上海交通大学“学术之星”评选

通讯评审材料

申请方向 动力工程及工程热物理

推荐单位 机械与动力工程学院

填表日期 2023 年 10 月 19 日

上海交通大学“学术之星”评选组委会 制表

目　录

1.主要学术科研成绩和贡献概述

申请人应详实、准确、客观地填写本人在本校攻读硕士或博士学位期间，在学术科研工作方面作出的成绩和贡献(**注：宋体、小四号字体，1.5倍行距，限两页**)。

本人以联合国2030可持续发展目标中“确保人人享有清洁、安全的水”的愿景为指导，应用工程热力学与材料学交叉学科知识，开展“吸附式大气集水”研究，探索解决干旱地区以及特殊场景下的淡水供应难题。在材料构筑方面，**首次构建了**适用于吸湿盐掺杂复合吸附材料的溶液保留机制，提出了指导复合水凝胶吸附材料吸附量、动力学与稳定性设计的**热力学准则**；在集水策略方面，**首次总结性提出并优化了**具备气候适应性的新型大气集水循环策略；在应用拓展方面，设计了材料-器件-系统的多层级热质传递耦合模型，保障了吸附材料在大气集水设备中的高效集成，最终在中国兰州、上海、新加坡的多气候湿度场景下**成功实现大气集水设备单日产水记录的突破**。在国际高水平期刊上累计发表学术论文13篇（独立一作6篇），包括Nature Communications、Advanced Materials、Joule、Energy & Environmental Science、Device。期间获国家留学基金委创新型人才国际合作项目资助在新加坡国立大学进行联授博士学位培养，参与“国家自然科学基金创新研究群体项目”、某委重点保密项目等科研项目。具体研究内容及同行评价如下：

(1) 材料构筑：提出指导吸附材料平衡吸附量、动力学及稳定性设计的热力学准则

针对原有吸湿盐掺杂复合材料无法精确调控吸附性能的问题，通过分析吸湿盐-水二元热力学系统中蒸汽压-浓度-温度关系和盐溶液-基质材料相互作用，提出了指导吸附材料平衡吸附量、动力学以及稳定性设计的热力学准则。

基于该准则构筑了聚电解质水凝胶高分子吸附材料体系，并对凝胶网络内部带电磺酸基团与盐离子的静电作用进行调控，实现了吸湿盐离子的络合与凝胶内部高渗透压的保持，获得了稳定盐溶液保留与快速水分迁移特性，**有效解决了原有吸附材料的缓慢动力学与循环稳定性下降等问题**。基于该准则还提出了聚四氟乙烯透湿、防水多孔膜的材料外部封装方法，进一步实现了吸附材料超高容量的盐溶液锁定，**完全解决了原有材料循环稳定性差以及溶液泄露导致的腐蚀、水污染问题**。在确保极高的稳定性的前提下，使用该准则开发的水凝胶与碳纤维材料，**显著提升了吸湿盐在吸附材料中的比例**，从而使材料在中低湿度条件下的吸附量达到了2.93 $g\ g^{-1}$，在国内外同类吸附材料中占据领先地位。

相关成果发表在Joule、Cell Reports Physical Science（Cell子刊，他引47次）等顶刊。所开发材料因其突出性能，被美国艺术与科学院院士、麻省理工学院Evelyn Wang课题组在Advanced Materials文章中**以图文形式作为典型材料进**

(2) 集水策略：首次总结性提出并优化适应多气候场景的新型大气集水循环策略

首次提出且优化了“夜间批量吸附、日间逐次解吸”的批处理大气集水循环模式以及“单块材料吸附-解吸快速切换”的多循环模式，通过策略设计弥合了吸附材料自身吸附势动态变化造成的动力学下降、昼夜温湿度波动、太阳能利用的随机间歇特性三个问题，**解决了传统昼夜切换循环模式造成的时间与能源的浪费，克服了从单一湿度到全湿度场景的可便携性器件的适应性难题**。

基于上述两种策略，在半干旱气候（兰州）、半湿润气候（上海）与湿润气候（新加坡）下进行了实地测试，实现了便携式装置产水量 **1 L kg^{-1} day^{-1} 的跨越**，并进一步翻倍提高至超过 2 L kg^{-1} day^{-1}。相比于文献报道的(半)干旱工况下的产水量数据，**在单位体积产水量上提高了 1.5 倍，单位质量产水量上提高了 6 倍**。

相关成果发表在 Nature Communications、Advanced Materials、Energy & Environmental Science 上。所提出的新型循环策略被麻省理工学院的学者在 Device 期刊文章中**作为过往大气集水领域的五种典型模式进行引用与分析**；被**国家杰青、科学探索奖获得者、南京大学朱嘉教授在 Advanced Materials 文章中以整段形式介绍**，并认为所提出的“批处理操作策略缓解了吸附缓慢与快速解吸间差距…这种模式可以在整个白天保持高的解吸速率…”。

(3)应用拓展：开展系统级热质传递模拟并拓展其在能源−水−食物关系中的应用

针对原有设备系统设计粗糙、效率低下等问题，开展了从材料-器件-系统的多层次热质传递模拟研究，精确捕捉材料与装置的温度、速度、浓度场特征。**首次证明了余热与光热耦合能量边界用于大气集水解吸循环的优势，解决了传统光热或电加热形式的升温速率缓慢、温度均匀性差的问题**，实现了能量边界与上述循环策略的匹配，保障了多场景下集水设备的热效率与高产水量。

将大气集水技术拓展到供水场景之外，利用其分布式、可持续能源驱动的特点，进行了“能源-水-食物”多功能耦合分析与开发。对于城市建筑微环境中的能源、水和食物循环与供应关系，展望并计算了大气集水与辐射制冷、建筑光伏一体化以及屋顶精准农业等技术的融合发展，以及其实现零能耗绿色建筑的潜力。具体到技术层面，使用大气集水技术实现了光伏散热强化，**使光伏板温度降低 2-6 °C**；利用吸附材料的多步热量储放效应，**将吸附储热密度进一步提高达到 9948 kJ kg^{-1}，比传统物理吸附剂储热密度提高 1-2 个数量级**，实现低品位热能和水的高效利用与储存；应用大气集水的除湿与产水功能，实现屋顶农场热环境控制与精准滴灌，获得了食物和水分布式供应。相关成果发表在 Energy，ACS Energy Letters 上。

2．代表性论文、专利、论著情况

<table>
<tr><td colspan="3">本栏目请填写申请人的代表性成果及他人对其成果的评价和引用情况，
（所列论文数不超过 3 篇，专著不超过 3 本，专利不超过 3 项）</td></tr>
<tr><td rowspan="6">论文</td><td colspan="2">论文 1：
Exceptional water production yield enabled by batch-processed portable water harvester in semi-arid climate. Nature Communications 13, 5406 (2022).</td></tr>
<tr><td>贡献度: ☑主要完成人 ☐次要完成人 ☐参与人</td><td>第一作者</td></tr>
<tr><td colspan="2">论文 2：
All-Day Multicyclic Atmospheric Water Harvesting Enabled by Polyelectrolyte Hydrogel with Hybrid Desorption Mode. Advanced Materials 35, 2302038 (2023).</td></tr>
<tr><td>贡献度: ☑主要完成人 ☐次要完成人 ☐参与人</td><td>第一作者</td></tr>
<tr><td colspan="2">论文 3：
Improving solar water harvesting via airflow restructuring using 3D vapor generator.
Device (Cell 姊妹刊，首卷发表) 1, 100065 (2023).</td></tr>
<tr><td>贡献度: ☑主要完成人 ☐次要完成人 ☐参与人</td><td>第一作者</td></tr>
<tr><td>他人引用及评价情况(不多于 5 条评价，限 400 字)</td><td colspan="2">1. 美国艺术与科学院院士、麻省理工学院(MIT)机械工程系主任 Evelyn Wang 教授课题组在国际知名期刊 Advanced Materials 上发文，其中<u>以数据分析与图片的形式引用</u>申请人在 Nature Communications 中所报道的材料，并将其作为吸附性能的参考比较对象；在 Cell 姊妹刊 Device 中，使用多幅表格和图片详细分析了申请人提出的器件和模式，将其<u>列为五种典型模式之一进行重点分析</u>。
2. 国家杰青、科学探索奖获得者、南京大学朱嘉教授在 Advanced Materials 发文以整段形式介绍申请人在 Nature Communications 中的策略与模式，并认为申请人提出的“批处理操作策略可以缓解吸附缓慢与快速解吸间差距…这种模式在整个白天<u>保持高的解吸速率</u>…”
3. 国际能源材料领域知名学者、美国德克萨斯大学奥斯汀</td></tr>
</table>

	分校(UT Austin) Guihua Yu 教授发表的 Angewandte Chemie 等文章中，以<u>图片与文字形式</u>评价申请人在 Cell 子刊 Cell Reports Physical Science (引用量：48 次，DOI 号：doi.org/10.1016/j.xcrp.2021.100664)上报道的盐溶液保留方法，认为该方法可以“进一步增盐负载量”并“防止泄露”。 4. 香港理工大学协理副校长、机械工程学系王钻开讲席教授在 Cell 子刊 Cell Reports Physical Science 文章中评价申请人所开发的方法“使用特殊的润湿材料来<u>防止液体泄漏的风险</u>”，可以保证了吸附材料稳定性，并使用类似结构开发了新型复合吸附剂。
论著	论著 1：
	负责完成　章节，共　万字　第□作者
	论著 2：
	负责完成　章节，共　万字　第□作者
	论著 3：
	负责完成　章节，共　万字　第□作者
论著受资助及获奖情况	
专利	专利 1：
	贡献度:□主要完成人 □次要完成人 □参与人　第□完成人
	专利 2：
	贡献度:□主要完成人 □次要完成人 □参与人　第□完成人
	专利 3：
	贡献度:□主要完成人 □次要完成人 □参与人　第□完成人
专利转化情况	

nature communications

Article

https://doi.org/10.1038/s41467-022-33062-w

Exceptional water production yield enabled by batch-processed portable water harvester in semi-arid climate

Received: 28 January 2022

Accepted: 31 August 2022

Published online: 15 September 2022

Check for updates

Sorption-based atmospheric water harvesting has the potential to realize water production anytime, anywhere, but reaching a hundred-gram high water yield in semi-arid climates is still challenging, although state-of-the-art sorbents have been used. Here, we report a portable and modularized water harvester with scalable, low-cost, and lightweight LiCl-based hygroscopic composite (Li-SHC) sorbents. Li-SHC achieves water uptake capacity of 1.18, 1.79, and 2.93 g g^{-1} at 15%, 30%, and 60% RH, respectively. Importantly, considering the large mismatch between water capture and release rates, a rationally designed batch processing mode is proposed to pursue maximum water yield in a single diurnal cycle. Together with the advanced thermal design, the water harvester shows an exceptional water yield of 311.69 g day^{-1} and 1.09 g $g_{sorbent}^{-1}$ day^{-1} in the semi-arid climate with the extremely low RH of ~15%, demonstrating the adaptability and possibility of achieving large-scale and reliable water production in real scenarios.

Freshwater scarcity has become a severe global challenge, since by 2025 almost 2 billion people will live in areas with absolute water scarcity[1,2]. A sustainable development goal raised by United Nations aims to solve water shortage with water availability and sustainability becoming of high concern[3]. Stable, portable, and high-yield clean water supply appears to be particularly vital, especially in emergencies or remote arid regions[4,5]. Atmospheric water, in the form of vapor and droplets, is a huge unexplored source of freshwater and its amount is equivalent to one-eighth of the total freshwater resources of rivers and lakes[6]. Harvesting overlooked but ubiquitous water resources in the atmosphere is considered as a potential approach to alleviate the water shortage[7]. Among all atmospheric water harvesting (AWH) technologies, sorption-based AWH (SAWH) shows high adaptivity and fewer limitations on environmental conditions, as sorbents have a strong affinity to capture water from air at a wide range of RH (~10–100% RH) and release it due to water vapor partial pressure difference[8,9].

The performance of SAWH systems highly depends on the water sorption capacity of sorbents. Recently, novel sorbents with high water uptake, low energy demand, fast kinetics, and cycling stability have been widely developed to improve the working performance of AWH systems[10], including metal-organic frameworks (MOFs)[11–16], hydrogels[17–22], and salt-based composite sorbents[23–28]. Salt-based composite sorbents are developed by inserting hygroscopic salt crystals into the porous matrix. The commonly used hygroscopic salts include lithium chloride (LiCl) and calcium chloride ($CaCl_2$), which show strong hygroscopicity and high equilibrium water uptake at low RH. Highly porous or capillary materials, such as fibrous substrates, polymer networks, and hollow containers, are frequently used as a matrix[10]. Unlike MOFs and hydrogels with relatively limited sorption humidity ranges, salt-based composite sorbents can realize excellent water uptake capacity at a wide range of RHs, thereby demonstrating a strong environmental adaptation. Besides, the synthesis of MOFs and hydrogels requires expensive raw materials, complex procedures, and strict reaction conditions, such as high temperature and pressure conditions of the hydrothermal reactions and the deoxidizing condition of free radical initiation synthesis, but salt-based composite sorbents can usually be easily synthesized by

[1]Institute of Refrigeration and Cryogenics, Shanghai Jiao Tong University, Shanghai 200240, China. [2]Engineering Research Center of Solar Power & Refrigeration, MOE China, Shanghai 200240, China. e-mail: sailote@sjtu.edu.cn; rzwang@sjtu.edu.cn

impregnating matrixes with salt solution at mild ambient conditions. Therefore, the cheap and industrially mass-produced raw materials and the simple production processes make the salt-based composite sorbents highly suitable for mass production and show great market potential.

It is of great concern that although many high-performance sorbents have been reported, the practical photothermal water harvesters are still very rudimentary or small-scale, with simple heat and mass transfer solutions, resulting in low efficiency and limited overall water yield[29,30]. Recently, many approaches, such as thermal insulation by silica aerogels[14], selective solar absorbers[31,32], dual-stage latent heat recovery[31], and multi-cyclic operation modes[12,23,33] have demonstrated the improvement of the overall energy efficiency and the water yield of solar-thermal water harvesters. For example, multiple water harvesting cycles over the whole day were implemented in a MOFs water harvester, achieving the water productivity of 0.7 L kg_{MOF}^{-1} day^{-1} in the actual desert climate. Besides, the water harvester with daily eight water capture-release cycles recently achieved ultrahigh outdoor water productivity of 1.05 L_{water} $kg_{sorbent}^{-1}$ day^{-1} only driven by natural sunlight. Furthermore, combining AWH systems with other applications, such as thermal management[34–38], energy generations or storage[39–44], and agriculture[19,35,45] can also be regarded as the methods to improve the overall production or efficiency of the AWH-related systems. With these approaches, the practical outdoor water productivity per kilogram of sorbent has improved from 0.07 to over 1 L kg^{-1} day^{-1}. However, challenges regarding high yield and stable water production remains. For passive photothermal water harvesters, the actual total daily water yield is limited to tens of grams, and they are overly sensitive to the fluctuation of solar energy, making it harder to meet the personal demand for daily drinking water. Contrary, active sorption-based water harvesters that rely on electric or thermal energy-driven sorption processes as input are getting more attention owing to their stable water productivity and significantly higher yield, whereas the weight and size of these harvesters are usually unacceptable, especially for portable SAWH applications[46,47]. This raises a question about the successful realization of portable, stable, and high-yield water harvesters that can meet the needs of emergency drinking water in multiple scenarios.

In this work, we introduce a portable and modularized water harvester with scalable, low-cost, and lightweight LiCl-based hygroscopic composite (Li-SHC) sorbents to realize a hundred-gram water production yield in a real semi-arid climate. Li-SHC shows excellent equilibrium water uptake and optimized sorption dynamics, achieving 1.18, 1.79, and 2.93 g g^{-1} at 15%, 30%, and 60% RH within night-time 12 h. More importantly, the gaps between material-level water uptake and real device-level water production are noticed. Considering the mismatch between relatively low water sorption and fast desorption rates, a batch-processed operation strategy was proposed in which multiple pieces of sorbents simultaneously capture water vapor to make full use of the nighttime high RH and release them alternately to maintain the high desorption rate during the entire daytime. The combination guarantees high water uptake of each piece of the sorbent as well as high water production yield in a single diurnal cycle. Together with the device-level advanced thermal designs, the portable water harvester with the volume of 5.6 L and the weight of 3.2 kg achieved water productivity of up to 311.69 g day^{-1} and 1.09 g $g_{sorbent}^{-1}$ day^{-1}, by applying eight desorption cycles in the real semi-arid environment (Lanzhou, China) with the extreme low RH of ~15%. Moreover, the harvester with lightweight sorbents can be easily deployed by a single person. With these features, the developed portable water harvester can realize high-yield freshwater production in real-world scenarios without the limitation of weather conditions and geographical locations. This study is expected to inspire further research focusing on the practical AWH applications to match actual human water consumption anytime and anywhere.

Results

Synthesis and characterization of Li-SHC

The sorbent Li-SHC was prepared by impregnating LiCl salt on active carbon felts which has been recognized as an excellent porous matrix choice for hygroscopic salts loading. The abundant micropores of carbon fibers provide ultra-high specific surface areas (Supplementary Fig. 1). Meanwhile, their physical entanglement and numerous channels enhance the hydrophilicity (Supplementary Fig. 2) and capillary force of the felt (Supplementary Fig. 3). The water uptake isotherm of the pure porous matrix (Supplementary Fig. 4) demonstrates the micropore filling at the low RH (<30%) and an increased water uptake at higher RH owing to the multilayer adsorption and capillary condensation in mesoporous[48], but the relatively low water adsorption capacity (<0.1 g g^{-1} below 30% RH) can hardly be suitable for water harvesting in arid climates. Therefore, hygroscopic nanoscale LiCl salts were uniformly loaded to the porous matrix by vacuum impregnation and mild heating methods to promote the water harvesting capacity in a wide working range of RHs. Meanwhile, the active carbon fiber felt serves as the matrix to support and disperse LiCl to alleviate the salt agglomeration and salt solution leakage. After LiCl loading, the dried sorbent becomes less flexible and shows a higher mechanical strength than the pure matrix, but the flexibility of the sorbent can be recovered after sorption (Supplementary Fig. 5).

The successful LiCl salt loading and its hydrated salt crystallization form (LiCl and LiCl·H_2O) at different temperatures (30, 60, 90, 110 °C) were confirmed by powder X-Ray diffraction (PXRD) of Li-SHC (Fig. 1a). The cut-section scanning electron microscope (SEM) image (Fig. 1b) and the energy-dispersive X-ray spectroscopy (EDX) mappings of Li-SHC (Fig. 1c) confirmed the LiCl crystals were successfully loaded on the surface of fibers and between the channels formed by the physical entanglement. When exposed to moist air, the water molecules can be absorbed by LiCl crystals on the surface of the fibers (Fig. 1d), then diffuse into the porous matrix, forming concentrated LiCl solution. The volume of LiCl solution is expanded during the absorption process, and the formed solution is stored inside the hydrophilic and highly porous matrix with strong capillary force. A water vapor breathable but waterproof porous polytetrafluoroethylene membrane was further applied to encapsulate sorbents to completely avoid the risk of solution leakage and the resulting corrosion and cyclic sorption performance degradation (Supplementary Figs. 6–9)[32,49,50].

The hygroscopic LiCl and its content are the critical parameters determining water vapor sorption performance for water uptake capacity and dynamics. Dynamic vapor sorption curves of Li-SHC (Fig. 1e) with five different salt contents (40, 70, 80, 90, and 95 wt%) were measured to study the effect of the porous matrix and LiCl loading content. The linear drive force (LDF) model was used to quantitively evaluate their dynamic sorption characteristics (Supplementary Information Section 2)[51]. The sorption rate coefficients k_{LDF} indicates a strong positive correlation between the salt content and the sorption rate (Supplementary Fig. 10). This variation of dynamic sorption characteristic owes to the mass transfer enhancement effect, provided by the matrix, as it leverages the effect of additional pores and channels for increased sorption interfacial area. However, with the increased salt content, LiCl crystals form not only on the fiber pores but also on the surface and between the gaps of fibers (SEM images see Supplementary Fig. 11), which inevitably reduces the vapor transport channels and the sorption dynamics. Note that although reducing the salt loading can increase the sorption dynamics, the absolute amount of water uptake decreases simultaneously. The desired salt content in practical water harvesting applications can be optimized by matching the duration of a sorption cycle with the required equilibrium duration, indicating no waste of both the sorbent material and the operating time[52]. Considering the 12-h nighttime sorption duration and performance degradation of scale-up sorbents in real climates, Li-SHC

https://doi.org/10.1038/s41467-022-33062-w

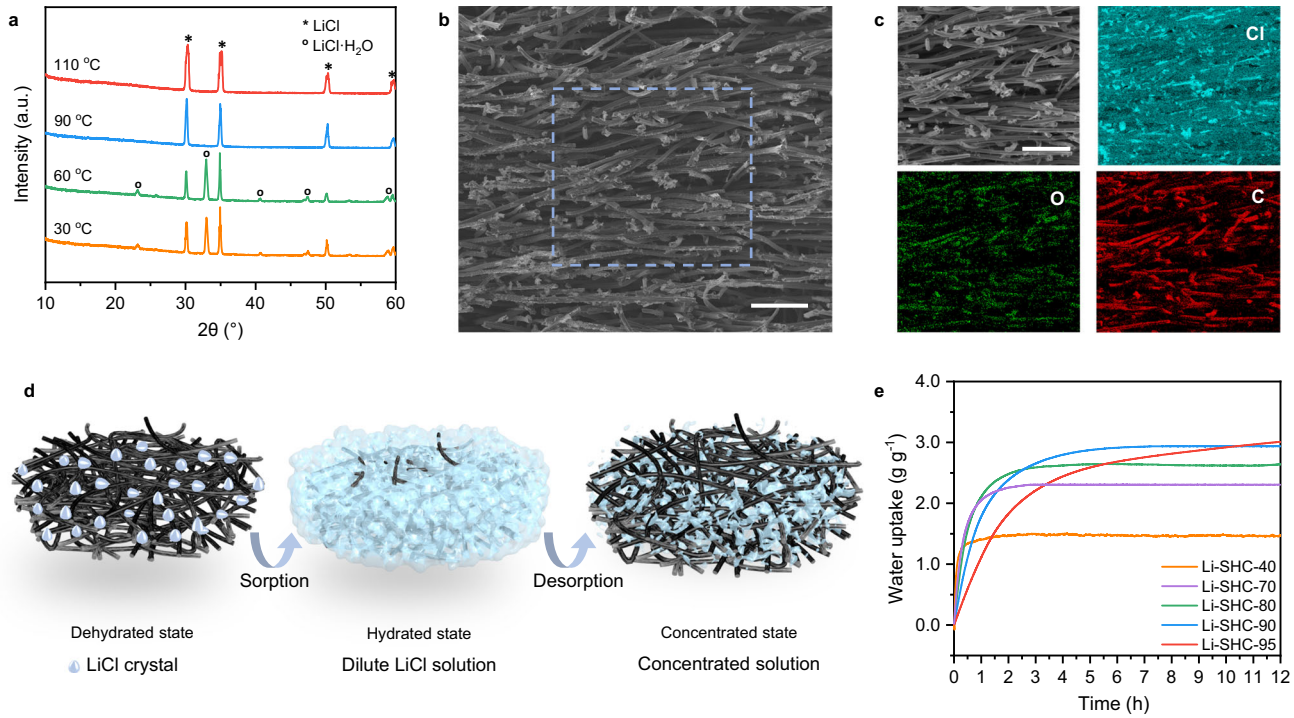

Fig. 1 | Characteristics and optimization of Li-SHC. a Variable temperature XRD patterns of porous matrix and sorbents. **b** SEM images of Li-SHC with the salt content of 90 wt% in the sectional view. Scale bar: 100 μm. **c** EDS element mapping of Li-SHC demonstrates the uniform nanoscale arrangements of LiCl crystals and small amounts of agglomeration. Scale bar: 100 μm **d** Schematic illustration of the sorption-desorption process. The water molecules are captured by LiCl crystals on the surface of the fibers, then diffuse into the porous matrix, forming concentrated LiCl solution. The solution is stored inside the hydrophilic and highly porous matrix with strong capillary force. **e** Dynamic sorption curves of Li-SHC with the salt content of 40%, 70%, 80%, 90%, and 95%.

with the salt content of ~90 wt% (referred to Li-SHC) was selected due to the best trade-off between sorption capacity and sorption dynamics.

The sorption isotherm of Li-SHC at 30 °C was shown in Fig. 2a. To reveal the sorption mechanism of Li-SHC, the phase diagram and the theoretical isotherm of pure LiCl were calculated (Supplementary Information Section 3) and presented in Supplementary Fig. 12 [53]. The isotherm of Li-SHC shows a highly similar isotherm of pure LiCl, which indicates that the equilibrium water uptake of Li-SHC is mainly determined by the sorption capacity of LiCl salt. In other words, the porous matrix has a negligible contribution to the equilibrium water uptake. The water uptake of Li-SHC shows the multi-step mechanism as demonstrated in Fig. 2a: 1. Chemisorption of anhydrous LiCl below the deliquescence RH (11% RH at 30 °C); 2. Deliquescence of hydrous LiCl ($LiCl{\cdot}H_2O$) and the saturated solution forms 3. Absorption of water vapor in saturated/concentrated LiCl solution[53]. Note that over 85% of total water uptake was attributed by the adsorption of water vapor in LiCl solution when sorption at RH > 60%, thus the third step highly contributes to the overall water uptake capacity.

Owing to the ultra-high LiCl content of Li-SHC, the water uptake reaches 1.18 g g^{-1}, 1.79 g g^{-1}, and 2.93 g g^{-1}, when the RH is increased to 15%, 30%, and, 60% RH, respectively. The results of dynamic sorption experiments under three typical climates, arid climate (30% RH), semi-arid climate (60% RH), and humid climate (90% RH) demonstrate the environmental adaptivity of Li-SHC (Fig. 2b). Surprisingly, Li-SHC takes up more than 846% water content under humid climates (90% RH) within 12 h, revealing the ultra-high water uptake capacity of Li-SHC. In arid climates (30% RH), Li-SHC also shows satisfactory water uptake performance in comparison to other reported AWH sorbents (Fig. 2c and Supplementary Fig. 13)[1,11,12,18–20,22,23,25,26,28]. Besides, the satisfied sorption dynamics can also be observed because Li-SHC can reach equilibrium within six hours at the RHs of 30% and 60%. Moreover, the sorption capacity of Li-SHC is insensitive to the ambient temperature because of the essential sorption mechanism of LiCl salt, thus it can be extended to extreme conditions regardless of air temperature (Supplementary Fig. 14). Sorption-desorption cycles performed over 186 h confirmed the stable equilibrium and dynamic sorption performance without degradation and LiCl leakage (Fig. 2d and Supplementary Fig. 15).

One of the most critical parameters for the evaluation of sorbent performance in real-world water harvesting is its sorption and desorption dynamics[54]. Based on a myriad of publications, it has long been ignored and less comprehensively evaluated, but with the development of the batch processing or continuous AWH, the importance of this parameter should be intensely evaluated and considered as well[55–57]. The reported sorption dynamics in most papers, including those presented in Fig. 2e, are usually conducted using milligram-scale samples inside an ideal constant humidity and temperature chamber with a fast air flow[58]. Although this thermogravimetric analysis is regarded as an appropriate scientific method for evaluating ideal sorption performance by controlling variables that might affect analysis, these results typically do not reflect the actual sorption state in practical climates and AWH devices because the performance of scale-up gram-scale sorbents is easily limited by higher vapor diffusion barriers and lower heat transfer rate, which is especially true for the monolithic sorbents with high packing thickness and density. Therefore, to evaluate the practical sorption performance in a real semi-arid climate more accurately, a massive sorbent (250 × 250 x 2 mm), whose weight is nearly 10000 times than those usually used in commercial sorption analyzer, was selected and tested in a typical semi-arid climate with the typical night-time humidity and temperature of 65% RH and 15 °C. The dynamic sorption curve under these nonideal conditions indicated, as expected, the slower water uptake dynamics (Fig. 2f). Note that this decrease in sorption performance is a common problem of sorbent materials used in devices, as even MOFs demonstrated a more serious performance reduction between milligram-

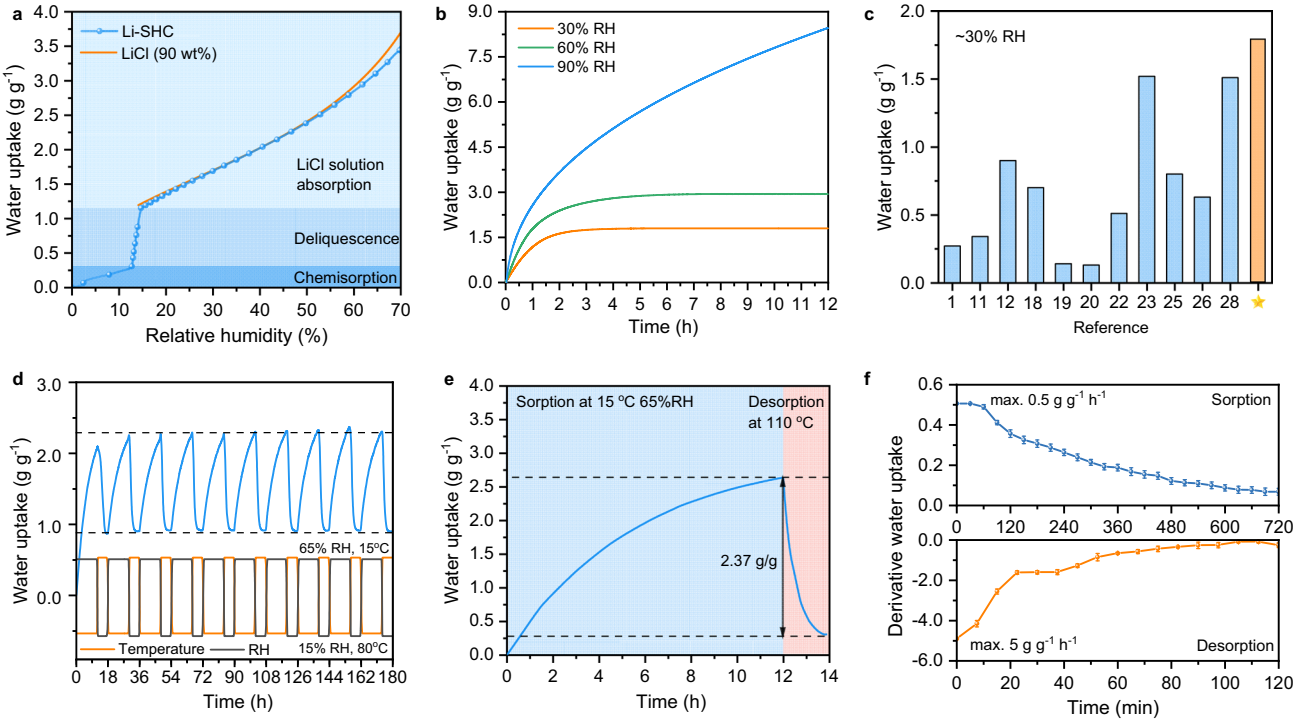

Fig. 2 | Sorption characteristic and comparison of Li-SHC. a Vapor sorption isotherm of Li-SHC and theoretical isotherm of LiCl with the initial specific mass of 90 wt%. **b** Dynamic sorption curves of Li-SHC at 30% RH, 60% RH, and 90% RH. **c** Comparison of vapor sorption capacity with the state-of-the-art sorbent materials at 30% RH. **d** Cycling performance of 2-mm-thick bulk Li-SHC. The sorption and desorption are performed at 65% RH, 15 °C, and 15% RH, 80 °C, respectively. **e** Dynamic sorption and desorption curves of 2-mm-thick bulk Li-SHC sample. The sorption curve was measured under a simulated semi-arid climate with the slight wind (15 °C, 65% RH). The desorption curve was measured using a hot plate at 110 °C. **f** Derivative water uptake changes of 2-mm-thick bulk Li-SHC sample demonstrating the mismatch between sorption and desorption time. Error bar: standard deviation (SD).

scale samples and bulk sorbents[33]. Furthermore, we measured the dynamic desorption performance of sorbents under a hot plate at 110 °C instead of placing them inside the constant climate chamber under ideal conditions. By comparing the derivative water uptake of sorption and desorption curves, we found a significant mismatch between water capture and release rates. The peak derivative sorption mass change is ~0.5 g g^{-1} h^{-1}, only 1/10 compared with the results of the desorption condition (~5 g g^{-1} h^{-1}). Therefore, two mismatches need to be particularly considered to pursue maximum water production yield if applying the sorbent to real devices: 1. the sorption performance of real bulk sorbents versus the milligram-level test samples; 2. the slow water sorption rate and the relative fast desorption rate. Fortunately, although a slower sorption dynamic limits the sorption performance of Li-SHC within 12 h, Li-SHC still shows a large amount of water release (2.37 g g^{-1}) in one water harvesting cycle under this actual situation, which benefits from the strong water affinity of LiCl salts, the high salt content of sorbents, and the better thermal conductivity of the carbon-based matrix. Also, to ensure quasi-continuous water collection during the daytime, a batch-processed operation mode is strongly needed to maintain a fast desorption rate during the entire daytime, which is expected to improve diurnal water collection rates.

Design and optimization of water harvester

Enabled by the high-performance, adaptable and stable sorbent Li-SHC, a portable and modularized water harvester was designed, manufactured, and assembled to demonstrate the water harvesting potential (Fig. 3a-b and Supplementary Figs. 16–18). The water harvester includes an electrical heating plate hosting layer(s) of Li-SHC sorbents with a surface area of 25 × 25 cm^2. The heating plate required a 12 V DC power supply, which can be easily realized by the photovoltaic (PV) or PV-battery power supply (Supplementary Fig. 19). The temperature of the heating plate was controlled by a well-designed feedback system, which can accurately adjust the heating power and consequently temperature within 2.5 °C by applying the feedback control method (Supplementary Fig. 20). During the desorption process, a condensation cover was connected and sealed with the heating plate by a buckle structure, which can be easily dismounted and reassembled. The hot moist air was generated by applying heat to the sorbents and transferred to the condensation cover due to the concentration and density differences between the desorption and condensation parts. It was then condensed into liquid water droplets and slid into water reservoirs at the edges of the condensation cover. During the night-time sorption process, sorbents were placed inside the device, capturing water vapor from the air. In the daytime, sorbents with high water content were used to generate the water vapor through desorption.

The optimum heating temperature was around 110 °C for sorbent regeneration, which ensured the long-term cyclic performance of a sorbent. Generally, to improve the vapor condensation performance, it is desirable to increase the temperature difference between the sorbent and condensation parts[59], which is determined by the heat and mass transfer inside the chamber (Fig. 3c). To do so, temperature and velocity distributions inside the harvester were numerically simulated by the COMSOL software (Supplementary Information Section 5). The simulation results indicate a large air velocity in the unblocked cavity region, resulting in a fully developed natural convection of heated moist air (Fig. 3d). This leads to a higher condensation temperature, thereby decreasing the temperature gradient between the condensation cover and the heating plate, resulting in further reduction of liquid water generation. To alleviate this problem, a highly reflective heat insulation panel, made of polystyrene foam coated with aluminum foil, was placed in the space above the sorbents (Supplementary Fig. 21). According to the further simulation results, the natural convection and the direct thermal radiation between the condensation surface and

https://doi.org/10.1038/s41467-022-33062-w

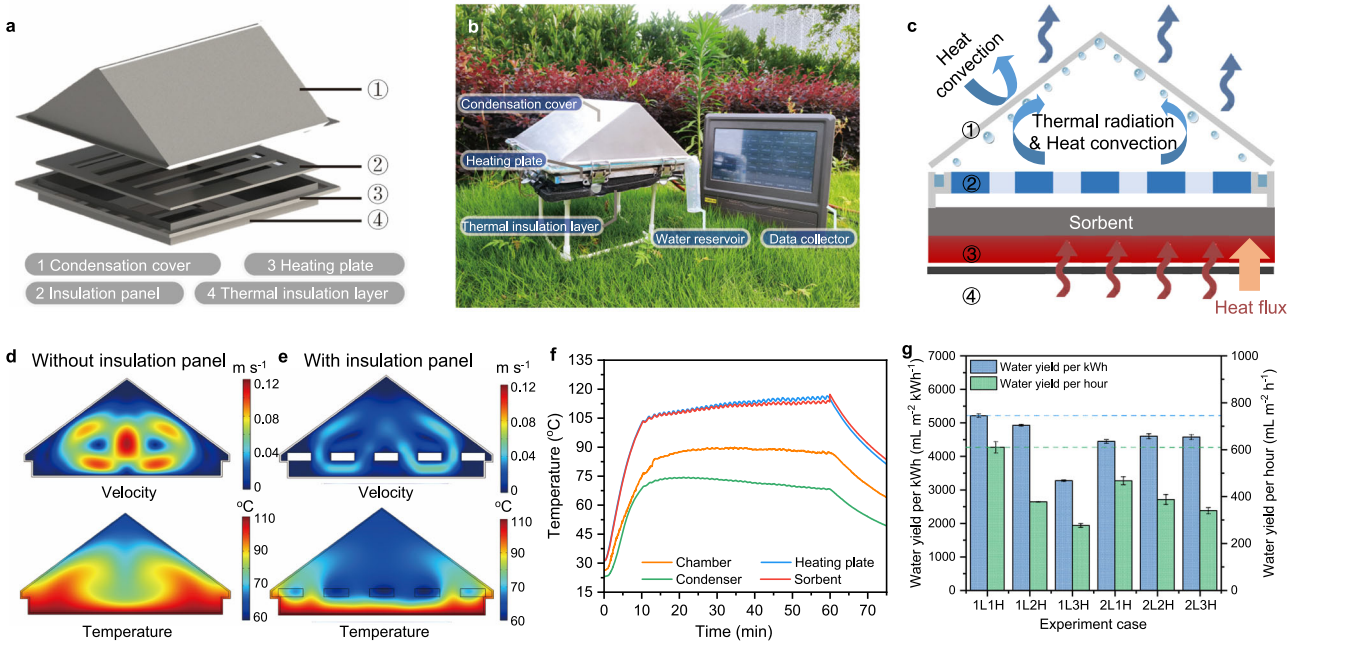

Fig. 3 | Design and optimization of sorption-based water harvester. a 3D render of the designed portable sorption-based water harvester. **b** Photo of the water harvester and the data collector. **c** Energy balance of the SAWH device during the water release-condensation process. **d** Velocity and temperature distribution inside the device without the insulation panel. **e** Velocity and temperature distribution inside the device with the insulation panel. **f** Temperature variation of the chamber, heating plate, condenser, and sorbent in the case of the 1-layer-sorbent and 1-heating-hour experiment. **g** Comparison of water yield per kilowatt-hour and per hour for six different experiment cases. L-layer(s), H-hour(s). Error bar: SD.

sorbents were remarkably reduced after installing this panel (Fig. 3e). The moist air movement is massively suppressed to the region below the insulation panel, which is exhibited by a highly increased temperature gradient. The steady-state temperature difference between the condensation surface and the heating plate reaches ~42 °C. To show the improvements after installing the panel more directly, the temperature variations of two selected characteristic points before and after installation were compared, showing a 25% drop in temperature (Supplementary Fig. 22).

Furthermore, we experimentally measured the temperature variations of the sorbents, chamber, heating plate, and condensation cover during the regeneration and collection experiment. As shown in Fig. 3f, the equilibrium-state surface temperature of the one-layer sorbent can reach up to 106.8 °C within 15 min under the heating temperature of 107.1 °C. Owing to the accuracy of the temperature control system, they are nearly stable during the following desorption process. Besides, the temperature difference between the sorbent and the heating plate was within 3 °C, proving the sufficient heat transfer performance of the sorbent. More importantly, as anticipated from simulation results, the temperature difference of 33–49 °C between the sorbent and condensation cover was achieved, which provided a strong driving force for the condensation process, ensuring a high liquid water collection rate.

To fully realize the daily water production potential of the water harvester, in addition to advanced heat and mass transfer study, we also investigated the optimization parameters and strategies. The heating hours (1–3 h) and the layer of sorbents (1 or 2) were selected as two optimization parameters to obtain maximum water productivity and minimize unit energy consumption. The parameter optimization experiments were conducted in the real semi-arid region (Lanzhou, China, 36.017° N, 103.784° E). Details information can be found in Supplementary Fig. 23–26. The results show that the total water yield increased from 609.6 mL m^{-2} to 828.8 mL m^{-2} with the increased heating time (Supplementary Fig. 27), but the water amount that produced in the single hour decreased by 55% in the case of one-layer sorbent. This is consistent with the dynamic desorption result of sorbents (Fig. 2f), in which 78% of water was released within the first 1 h, whereas only 11% of water was released over the following 1 h. It further demonstrates that regenerating multiple pieces of sorbents successively each hour to fully maintain the fastest desorption rate of each sorbent can obtain the highest possible amount of water in a limited time.

The energy consumption of water production is another assessment criterion. Energy input determines the maximum theoretical amount of water production, especially when solar PV electricity is used for heat supply. As shown in Fig. 3g, the maximum water yield per unit of energy consumption (5215.1 mL m^{-2} kWh^{-1}) also occurred in the case of the one-layer one-hour case. As for the one-layer three-hour case, the water yield per kWh dramatically declines to only 3274.4 mL m^{-2} kWh^{-1}. It has been proven that when the heating time increased from two to three hours, more input energy cannot be used for vapor generation because at this time the sorbent has already reached the desorption equilibrium. To sum up, the 1-layer 1-hour case is the optimal mode to pursue higher water production and lower energy consumption within a limited time.

Field test of batch-processed water harvester in semi-arid climate

The operation mode of the most reported SAWH devices is quite simple—single water capture-release cycle in a diurnal cycle, resulting in the inefficient water production, largely because of the apparent mismatch between the sorption and desorption dynamics. Such an operation strategy leads to inefficient utilization of solar energy and consequently lowers the corresponding water yield per 24 h due to the fast desorption rate with a depleted source of sorbed water (Supplementary Fig. 28a). Many research studies attempted to solve this mismatch by semi-continuous or continuous AWH cycles, but this means that the water capture cycles have to take place during the daytime at low RH environments (Supplementary Fig. 28b)[23,25,33]. However, the high RH brought in the nighttime due to diurnal air

https://doi.org/10.1038/s41467-022-33062-w

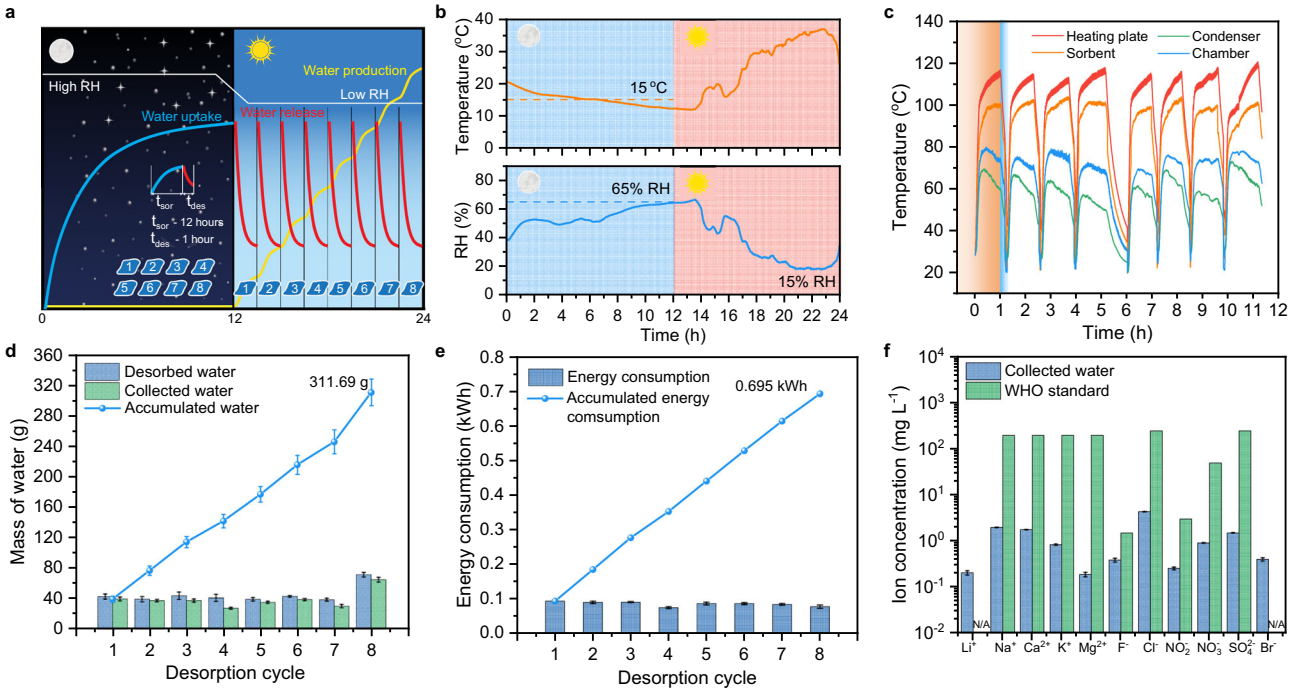

Fig. 4 | Water harvesting performance of the water harvester by applying the batch-processed alternating mode. a Schematic diagram of the proposed batch-processed alternating mode, showing the variation of water capture, release, and production in a single diurnal cycle. The eight pieces of sorbents are simultaneously exposed to the high RH ambient during the night, and consequent batch-operation desorption releases water vapor with freshwater production during the daytime. The white, blue, red, and yellow lines represent RH variation, water uptake, water release, and water production over the whole day, respectively. **b** Air temperature and RH variation within 24 h in the semi-arid region of Lanzhou, China. RH: relative humidity; **c** Temperature variations of the sorbent and device during eight desorption cycles including the heating stages and standby stages. **d** Mass of desorbed and collected water during each cycle, and its accumulated water. **e** Energy consumption during each desorption cycle. **f** Detected concentrations of the possible metal and ions in the collected water. All error bars represent SD.

temperature variation in the semi-arid climates, is more beneficial for the water sorption. To bridge this gap, a distinctive operation strategy, in which the multiple pieces of sorbents are simultaneously exposed to the ambient with high RH in the nighttime to absorb water vapor, then batch-processed alternately for water release during the daytime, is proposed to make full use of both the nighttime high RH environment and maintain high desorption rates throughout the day (Fig. 4a). In practical device operation, this operation strategy requires the portability, adaptability, and stability of both hygroscopic materials and water harvesters. The lightweight sorbent Li-SHC produced with low-cost and sustainable raw materials, facile and easily scaled-up fabrication procedures show excellent water sorption performance, adaptability, and stability, which allows fast deployment into practical applications (Supplementary Information Section 6). Additionally, the portable and cheap water harvester can be easily disassembled, reassembled, and carried by a person. These features make it possible to realize ultra-high freshwater production yield in a diurnal cycle in real arid scenarios.

Based on the presented strategy, we demonstrate the viability of the multicycle mode and pursue its potential of maximum water productivity in a single day under practical climatic conditions. Specifically, eight AWH cycles were obtained by the batch alternating operation strategy in one day (Fig. 4b and details information see Supplementary Section 7). The daytime RH in Lanzhou, China recorded extremely low values of ~15% RH, while it increased to ~65% RH during the nighttime as the air temperature dropped by 15 °C (Fig. 4b). The eight pieces of sorbents were exposed to the nighttime high RH ambient and absorbed water vapor, then they were moved to the water harvester to release water vapor one by one from 8 AM. Then, the condensation cover was assembled and then the water release process started. The sorbent temperature rose rapidly to the set temperature and was maintained for 60 min. The condensation temperature was between 71 to 50 °C and dropped with the decrease of the desorption rate. Each cycle consisted of a 60-min heating stage and a ~20-min standby stage (Fig. 4c). The total duration of the 8-cycle experiment was ~11.3 h.

The quantity of collected and desorbed water for each cycle is shown in Fig. 4d and Supplementary Table 7. Remarkably, the overall water productivity was 311.69 g, even in the extreme semi-arid climate with the lowest RH of ~15%, which make the daily water productivity of the portable sorption-based water harvester into the order of 100 grams. The energy consumption for each cycle is displayed in Fig. 4e and Supplementary Table 8, in which the average energy consumption is lower than that of the single-cycle shown above, because of the heat capacity of the device. This competitive water productivity (311.69 g day^{-1}) and associated low costs (0.19 $ L^{-1}, 448.5 mL kWh^{-1}) enable the large-scale AWH in real semi-arid regions, showcased by our portable device as one of the most promising approaches to overcome the challenges of water supply in emergencies and rural areas[60]. Furthermore, we measured the concentrations of the metals and ions in the collected water (Fig. 4f), and the results show that the quality of the water extracted from the air meets the requirements for drinking water quality set by the World Health Organization (WHO). Finally, the stability of the device was evaluated by conducting the 6-day water harvesting and batch-processed water production cycling experiments under various simulated climate conditions, further demonstrating the stability of the bulk sorbents and the strong environmental adaptability of the water harvester (Supplementary Fig. 29).

Except for the price of produced water, various tradeoffs between water productivity, cost, weight, and volume of the device need to be considered during the design of AWH systems. Additionally, there are

multifarious sorbents, structures, and energy sources involved in these devices. For our work, the water productivity per gram of sorbents per day is 1.09 g of obtained water per gram of sorbent per day ($g_{water}\ g_{sorbent}^{-1}\ day^{-1}$), which has taken into account the mass of the eight replaced sorbents. From the whole device level, the portable water harvester with the volume of 5.6 L and the weight of 3.2 kg achieved the water production yield of 311.69 g per day, showing the apparent superiority regarding the weight and space of the whole device (Supplementary Fig. 30). These advantages are highly attributed to the advanced thermal design of the device to avoid the use of complex auxiliary devices, and the proposed operation strategy to fully utilize the desorption time.

For a comprehensive assessment of the water production potential, we selected five typical climates across the globe, including arid, semi-arid, and humid climates, and obtained their daytime and nighttime average ambient temperature and RHs (Supplementary Information Section 10). Then, based on the collected performance data in field tests, the water production of each location was estimated and shown in Fig. 5a. The water production is significantly influenced by the ambient RH, as over 1000 mL day^{-1} water production could be achieved in a relatively humid climate (e.g., Birmingham, GRB) but the lower limit of water production (150 mL day^{-1}) was reached in the aridest month of the Sahara Desert (Kharga, EGY). Furthermore, the global daily water production potential of the water harvester is also estimated according to the Dubibib-Astakhov (D-A) equation[61], the global average annual RH, and the collected performance data of the proposed water harvester. The water production potential of the water harvester is conservatively estimated at over 350 mL day^{-1} in the majority of locations, only except for the Tibetan Plateau, North Africa, etc. (Fig. 5b).

Our developed water harvester with a facile operation strategy shows its impressive record-breaking metrics, demonstrating a near realizable high yield of portable water production anytime and anywhere. Featured with a low total capital investment of both the sorbent and device and low operation costs, the portable water harvester demonstrated its market potential, making it closer to marketization and industrialization.

Discussion

We demonstrated a realization of a high-performance and portable water harvester with scalable, low-cost, and lightweight sorbent Li-SHC, which was comprehensibly developed from the perspective of materials, as well as advanced structure design and operation strategy. With the optimized LiCl content, Li-SHC shows the water uptake capacity of 1.18, 1.79, and 2.93 g g^{-1} at 15%, 30%, and 60% RH, respectively. The bulk sorbent Li-SHC shows a high water release of 2.37 g g^{-1} in a single water capture-release cycle under a simulated practical semi-arid environment. By combining simulations and experimental approaches, the portable water harvester with the volume of 5.6 L and the weight of 3.2 kg was designed and optimized. Together with the proposed novel eight-cycle batch alternating desorption mode with maintaining the high water desorption rate during the daytime, the portable water harvester achieved an exceptional water production yield of 311.69 g day^{-1} and 1.09 $g_{water}\ g_{sorbent}^{-1}\ day^{-1}$ in an entire semi-arid region with an extremely low RH of ~15%, which puts the daily water productivity of portable sorption-based water harvester on the hundred-grams scale. Remarkably, this portable device shows apparent superiority regarding the weight and space of the whole device, demonstrating exceptional performance considering these metrics.

We anticipate that this study could make a closer step to practical AWH to meet the daily personal water demand and could serve as an inspiration for future research work related to batch-operated practical AWH systems. Currently, the desorption heat is provided by joule heating. The main advantage of the proposed desorption mechanism based on electrical heating is to obviate the intermittence and periodicity of solar thermal heating to desorb and collect the adsorbed water as much as possible during the whole day. Considering the high correspondence between arid regions and solar-rich regions, the possibility of using solar PV systems to boost low-carbon water harvesters was estimated (Supplementary Information Section 11). By matching the energy demand of the above 8 water harvesting cycles and the performance of commercial PV modules under different weathers, we calculated the demand for solar panel areas, showing that solar panels with an area of 1.11–2.08 m^2 can meet the requirements of the water collection cycle shown above. Therefore, the thin-film solar cells that can be carried by a person could be used for portable water harvesting, and the silicon solar cells could power the scaled-up water harvester in areas without an electrical grid. Furthermore, new research avenues related to direct solar utilization in the form of PV/T panels or individual solar absorbers in conjunction with thermal storage should be investigated in detail, which could improve the overall system energy efficiency. More importantly, storing solar energy in electricity (e.g., batteries) and thermal heat (e.g., phase change materials) could expand the water release process into the night, realizing all-day atmospheric water harvesting. Finally, further advancements in tailor-made sorbents, where new materials with exceptional physical and chemical properties are combined into composite sorbents could pave the road for next-generation sorbents. For instance, joule-heating electrical components could serve as a nano/micro porous matrix, also

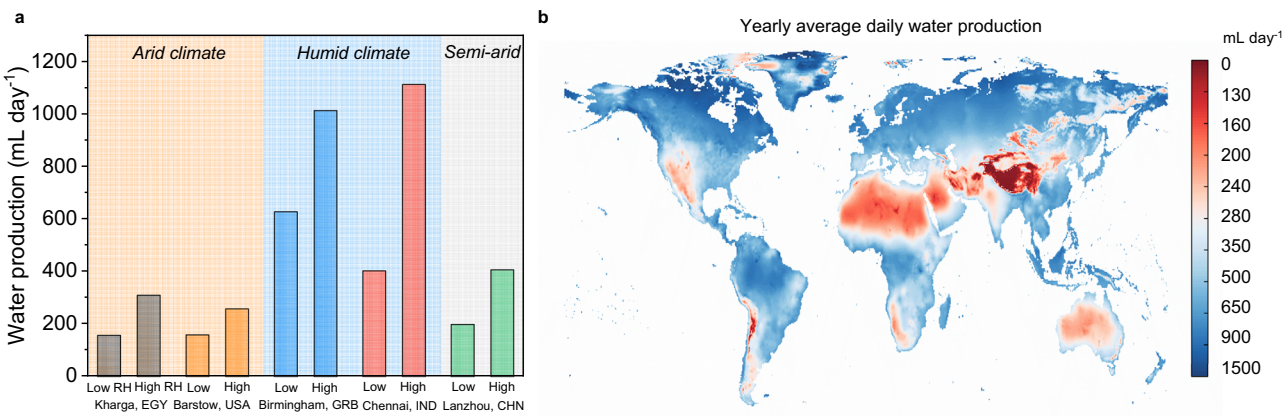

Fig. 5 | Estimated water production of the water harvester applying the sorbent and operation strategy. a Estimated daily water production in typical arid, humid, and semi-arid climates. The month with the lowest (highest) monthly average RH throughout the year is marked as a low (high) RH month. **b** Daily water production of the water harvester that is estimated by the yearly average RHs.

possessing high thermal conductivity, thus further reducing losses by introducing electrical heat utilization.

Methods

Synthesis and characterization of Li-SHC

Active carbon fiber felt was supplied by Kejing Carbon Materials. PTFE membranes were supplied by Zeyou Fluoroplastic. Lithium chloride (99%) was purchased from Sigma-Aldrich. Li-SHC were prepared by immersing the active carbon fiber felt pieces that were pre-dried at 120 °C for 8 h in pre-prepared LiCl solution with various concentration (0.05–0.45 g mL^{-1}). The wetted matrixes with the LiCl solution were then transferred into a vacuum drying chamber to eliminate the entrapped air in the matrixes. After 8 h, the wetted matrixes were taken out of the solution and then wrapped inside the porous PTFE membrane with a pore size of 3 μm. Finally, the sides of composite sorbents were encapsulated carefully to obtain the composite sorbents.

Nitrogen gas adsorption isotherms were recorded on volumetric gas adsorption analyzer at 77 K by 3Flex America Micromeritics. Attenuated total reflectance Fourier transform infrared (ATR-FTIR) spectra were recorded on the FTIR spectrometer (Nicolet 6700) using an attenuated total reflection (ATR) cell equipped with a Ge crystal. Powder x-ray diffraction (PXRD) patterns were recorded with a Bruker D8 ADVANCE diffractometer (Göbel-mirror monochromated Cu Kα1 radiation, λ = 1.54056 Å). The morphology and elemental distribution were examined by scanning electron microscopy (SEM) and energy-dispersive X-ray spectroscopy (Nova NanoSEM 230) equipped with energy disperse X-ray spectroscopy (EDS, X-MaxN 80, Oxford). The contact angles were measured by a surface contact angle meter (Data physics OCA20) at ambient temperature (~24 °C) using a 5 μL water droplet as the indicator. Inductively coupled plasma-optical emission spectroscopy (ICP-OES) (Avio 500) and Ion Chromatography (ICS-5000+/900) were used to assess the water quality.

Measurements of water vapor sorption performance

Water sorption isotherms were measured by a commercial gas sorption apparatus (3Flex, Micromeritics). The dynamic water sorption–desorption tests of microgram-scale sorbents were performed on a thermogravimetric analyzer (STA 449C, Netzsch), equipped with a moisture humidity generator (MHG 32, ProUmid). The samples were completely dried at 120 °C, then placed in the thermogravimetric analyzer and kept at 30 °C under different humidity (30%, 60%, and 90% RH) for 12 h for water sorption.

Dynamic water vapor sorption-desorption experiments of the 2-mm-thickness sorbents were conducted in a constant climate chamber (KMF-115, Binder) with the temperature and RH accuracy of ±0.1 °C and ±1.5% RH. All samples were dried at 120 °C for 4 h to be dehydrated before the sorption tests. Once the chamber reached the set temperature (15 °C) and humidity (65% RH), the dehydrated composites were moved into the chamber. After a 12-hour sorption process, the sorbents were taken out and placed on a hot plate with a temperature of 110 °C to simulate the actual situation inside the AWH device. The mass change was measured by an analytical balance (Mettler Toledo ME204, 0.1 mg).

The sorption-desorption cyclic experiments were conducted to evaluate the stability of Li-SHC. The dehydrated sample with an area of 3 ×3 cm^2 firstly absorbed water vapor at 15 °C and 65% RH inside the constant climate chamber (KMF-115, Binder) for 12 h. After that, the environment was changed to the desorption condition (80 °C, 15% RH) for 6 h. The sorption-desorption cycles were repeated ten times, which took over 10,000 min. The weight change of the sample was recorded by the analytical balance. The stability and adaptability of the water harvester were evaluated by the 6-day water collection experiments under three various simulated climatic conditions. Detailed information can be found in Supplementary Information.

Device fabrication and data acquisition

The water harvester was composed of an electrical heating plate (25 cm × 25 cm) attached to a sorbent container (29 cm × 29 cm × 2.4 cm) made of a 19 mm thick aluminum plate welded to the upper side of the side walls (25 cm × 1.9 cm). A roof-shaped condensation cover with an angle of 37° with the horizontal line connected with the sorbent container. A blind-style high reflectivity and heat insulation panel (254 mm × 254 mm) with four empty areas (25 mm × 190 mm), made of polystyrene foam coated with aluminum foil, was placed in the space above the sorbents. Detailed information on the water harvester, temperature control system, and heating system can be found in Supplementary Information.

As for the data acquisition system, an ultra-thin K-type thermocouple with a diameter of 0.1 mm (−20-200 °C, ±1 °C) was used to measure temperatures. The measure points were arranged on the surface of the heating plate, the inner surface of the condensation part, the central point of sorbents, and the vapor-flowing path. These signals were transferred to an Agilent 34970A. The current signal was transferred by the transmitter to the data acquisition system. All data were recorded and processed by PC.

Field test in the semi-arid climate

The field tests of the water harvester were conducted in a real semi-arid environment, which is located in Xiagouya Mountain, Lanzhou, China (36.017° N, 103.784° E) in September 2021. The indoor and outdoor temperature and RH were recorded by two temperature and RH sensors (COS-03, Renke) with an accuracy of 0.15 °C and 1.5% RH.

The parameter optimization procedure before the batch-process experiments were conducted within two days. The dry weights of sorbents were between 37.90–39.65 g. All sorbents were exposed to the air for 12 h from 20:00 to 08:00 the next day. After that, the weight of the sorbent was recorded by a balance (0.01 g), and the water uptake of the sorbents was calculated (1.83–2.19 g g^{-1}). Then, the sorbents were placed inside the water harvester for water desorption and collection. The ambient temperature and RH during the desorption were 30 °C, and 20% RH, respectively. The device adjustment, batch-process multicycle experiment, and repeated experiments were conducted on the following days. The sorption process was from 20:00 to 08:00 during the night, and then the sorbents were alternately sealed and placed inside the water harvester. Taking the time lag of vapor condensation and the frequency of material replacement into account, each desorption duration was ~1.35 h, and 8 cycles took around 11 h. The desorption time was from ~08:00 to ~19:30. Note that the fourth cycle was longer than the others. This rest time is in line with the special situation, such as an emergency water supply, that is operated by a single person, indicating that each AHW cycle could be decoupled and paused. The number of cycles can be determined by the daily water demand and the allowed operating time, and the maximum recommended number of cycles is eight.

Data availability

All the data needed to evaluate the conclusions in the paper are present in the paper and/or the Supplementary information. Source data are provided with this paper.

References

1. Kim, H. et al. Water harvesting from air with metal-organic frameworks powered by natural sunlight. *Science* **356**, 430–434 (2017).
2. Mekonnen, M. M. & Hoekstra, A. Y. Four billion people facing severe water scarcity. *Sci. Adv.* **2**, e1500323 (2016).
3. Wang, W. et al. Solar seawater distillation by flexible and fully passive multistage membrane distillation. *Nano Lett.* **21**, 5068–5074 (2021).
4. Lord, J. et al. Global potential for harvesting drinking water from air using solar energy. *Nature* **598**, 611–617 (2021).

5. Tu, Y., Wang, R., Zhang, Y. & Wang, J. Progress and expectation of atmospheric water harvesting. *Joule* **2**, 1452–1475 (2018).
6. Xu, W. & Yaghi, O. M. Metal–organic frameworks for water harvesting from air, anywhere, anytime. *ACS Cent. Sci.* **6**, 1348–1354 (2020).
7. Zhou, X., Lu, H., Zhao, F. & Yu, G. Atmospheric water harvesting: a review of material and structural designs. *ACS Mater. Lett.* **2**, 671–684 (2020).
8. Ejeian, M. & Wang, R. Z. Adsorption-based atmospheric water harvesting. *Joule* **5**, 1678–1703 (2021).
9. Zhang, Y. et al. Atmospheric water harvesting by large-scale radiative cooling cellulose-based fabric. *Nano Lett.* **22**, 2618–2626 (2022).
10. Yang, K. et al. A roadmap to sorption-based atmospheric water harvesting: from molecular sorption mechanism to sorbent design and system optimization. *Environ. Sci. Technol.* **55**, 6542–6560 (2021).
11. Fathieh, F. et al. Practical water production from desert air. *Sci. Adv.* **4**, eaat3198 (2018).
12. Rieth, A. J., Yang, S., Wang, E. N. & Dincă, M. Record atmospheric fresh water capture and heat transfer with a material operating at the water uptake reversibility limit. *ACS Cent. Sci.* **3**, 668–672 (2017).
13. Towsif Abtab, S. M. et al. Reticular chemistry in action: a hydrolytically stable MOF capturing twice its weight in adsorbed water. *Chem* **4**, 94–105 (2018).
14. Kim, H. et al. Adsorption-based atmospheric water harvesting device for arid climates. *Nat. Commun.* **9**, 1191 (2018).
15. Yang, T., Ge, L., Ge, T., Zhan, G. & Wang, R. Binder-free growth of aluminum-based metal–organic frameworks on aluminum substrate for enhanced water adsorption capacity. *Adv. Funct. Mater.* **32**, 2105267 (2022).
16. Feng, Y., Ge, T., Chen, B., Zhan, G. & Wang, R. A regulation strategy of sorbent stepwise position for boosting atmospheric water harvesting in arid area. *Cell Rep. Phys. Sci.* **2**, 100561 (2021).
17. Guo, Y. et al. Scalable super hygroscopic polymer films for sustainable moisture harvesting in arid environments. *Nat. Commun.* **13**, 2761 (2022).
18. Zhao, F. et al. Super moisture-absorbent gels for all-weather atmospheric water harvesting. *Adv. Mater.* **31**, 1806446 (2019).
19. Yang, J. et al. A moisture-hungry copper complex harvesting air moisture for potable water and autonomous urban agriculture. *Adv. Mater.* **32**, 2002936 (2020).
20. Yao, H. et al. Highly efficient clean water production from contaminated air with a wide humidity range. *Adv. Mater.* **32**, 1905875 (2020).
21. Nandakumar, D. K. et al. Solar energy triggered clean water harvesting from humid air existing above sea surface enabled by a hydrogel with ultrahigh hygroscopicity. *Adv. Mater.* **31**, 1806730 (2019).
22. Aleid, S. et al. Salting-in effect of zwitterionic polymer hydrogel facilitates atmospheric water harvesting. *ACS Mater. Lett.* **4**, 511–520 (2022).
23. Xu, J. et al. Ultrahigh solar-driven atmospheric water production enabled by scalable rapid-cycling water harvester with vertically aligned nanocomposite sorbent. *Energy Environ. Sci.* **14**, 5979–5994 (2021).
24. Xu, J. et al. Efficient solar-driven water harvesting from arid air with metal–organic frameworks modified by hygroscopic salt. *Angew. Chem. Int. Ed.* **59**, 5202–5210 (2020).
25. Li, R., Shi, Y., Wu, M., Hong, S. & Wang, P. Improving atmospheric water production yield: Enabling multiple water harvesting cycles with nano sorbent. *Nano Energy* **67**, 104255 (2020).
26. Lei, C. et al. Polyzwitterionic hydrogels for efficient atmospheric water harvesting. *Angew. Chem. Int. Ed.* **61**, e202200271 (2022).
27. Wang, J. Y., Wang, R. Z., Tu, Y. D. & Wang, L. W. Universal scalable sorption-based atmosphere water harvesting. *Energy* **165**, 387–395 (2018).
28. Entezari, A., Ejeian, M. & Wang, R. Super atmospheric water harvesting hydrogel with alginate chains modified with binary salts. *ACS Mater. Lett.* **2**, 471–477 (2020).
29. Gordeeva, L. G. et al. Metal-organic frameworks for energy conversion and water harvesting: A bridge between thermal engineering and material science. *Nano Energy* **84**, 105946 (2021).
30. Hanikel, N., Prévot, M. S. & Yaghi, O. M. MOF water harvesters. *Nat. Nanotechnol.* **15**, 348–355 (2020).
31. LaPotin, A. et al. Dual-stage atmospheric water harvesting device for scalable solar-driven water production. *Joule* **5**, 166–182 (2021).
32. Shan, H. et al. High-yield solar-driven atmospheric water harvesting with ultra-high salt content composites encapsulated in porous membrane. *Cell Rep. Phys. Sci.* **2**, 100664 (2021).
33. Hanikel, N. et al. Rapid cycling and exceptional yield in a metal-organic framework water harvester. *ACS Cent. Sci.* **5**, 1699–1706 (2019).
34. Li, R., Shi, Y., Wu, M., Hong, S. & Wang, P. Photovoltaic panel cooling by atmospheric water sorption–evaporation cycle. *Nat. Sustainability* **3**, 636–643 (2020).
35. Li, R. et al. An integrated solar-driven system produces electricity with fresh water and crops in arid regions. *Cell Rep. Phys. Sci.* **3**, 100781 (2022).
36. Pu, S. et al. Promoting energy efficiency via a self-adaptive evaporative cooling hydrogel. *Adv. Mater.* **32**, 1907307 (2020).
37. Wang, C. et al. A thermal management strategy for electronic devices based on moisture sorption-desorption processes. *Joule* **4**, 435–447 (2020).
38. Xu, J. et al. Near-zero-energy smart battery thermal management enabled by sorption energy harvesting from air. *ACS Cent. Sci.* **6**, 1542–1554 (2020).
39. Wang, X. et al. Hydrovoltaic technology: from mechanism to applications. *Chem. Soc. Rev.* **51**, 4902–4927 (2022).
40. Yang, L. et al. Energy harvesting from atmospheric humidity by a hydrogel-integrated ferroelectric-semiconductor system. *Joule* **4**, 176–188 (2020).
41. Xu, T. et al. An efficient polymer moist-electric generator. *Energy Environ. Sci.* **12**, 972–978 (2019).
42. Zhang, Y. et al. An asymmetric hygroscopic structure for moisture-driven hygro-ionic electricity generation and storage. *Adv. Mater.* **34**, 2201228 (2022).
43. Zhang, Y., Nandakumar, D. K. & Tan, S. C. Digestion of ambient humidity for energy generation. *Joule* **4**, 2532–2536 (2020).
44. Yan, T. et al. Ultrahigh-energy-density sorption thermal battery enabled by graphene aerogel-based composite sorbents for thermal energy harvesting from air. *ACS Energy Lett.* **6**, 1795–1802 (2021).
45. Zhou, X., Zhang, P., Zhao, F. & Yu, G. Super moisture absorbent gels for sustainable agriculture via atmospheric water irrigation. *ACS Mater. Lett.* **2**, 1419–1422 (2020).
46. Wang, W. et al. Viability of a practical multicyclic sorption-based water harvester with improved water yield. *Water Res.* **211**, 118029 (2022).
47. Wang, W. et al. Air-cooled adsorption-based device for harvesting water from island air. *Renew. Sustain. Energy Rev.* **141**, 110802 (2021).
48. Alcañiz-Monge, J., Linares-Solano, A. & Rand, B. Mechanism of adsorption of water in carbon micropores as revealed by a study of activated carbon fibers. *J. Phys. Chem. B* **106**, 3209–3216 (2002).
49. Wang, Y. et al. Heterogeneous wettability and radiative cooling for efficient deliquescent sorbents-based atmospheric water harvesting. *Cell Rep. Phys. Sci.* **3**, 100879 (2022).

50. Li, W. et al. A facile strategy to prepare robust self-healable superhydrophobic fabrics with self-cleaning, anti-icing, UV resistance, and antibacterial properties. *Chem. Eng. J.* **446**, 137195 (2022).
51. Sircar, S. & Hufton, J. R. Why does the linear driving force model for adsorption kinetics work? *Adsorption* **6**, 137–147 (2000).
52. Díaz-Marín, C. D. et al. Kinetics of sorption in hygroscopic hydrogels. *Nano Lett.* **22**, 1100–1107 (2022).
53. Conde, M. R. Properties of aqueous solutions of lithium and calcium chlorides: formulations for use in air conditioning equipment design. *Int. J. Therm. Sci.* **43**, 367–382 (2004).
54. Song, Y. et al. High-yield solar-driven atmospheric water harvesting of metal–organic-framework-derived nanoporous carbon with fast-diffusion water channels. *Nat. Nanotechnol.* **17**, 857–863 (2022).
55. Park, H. et al. Enhanced atmospheric water harvesting with sunlight-activated sorption ratcheting. *ACS Appl. Mater. Interfaces* **14**, 2237–2245 (2022).
56. Legrand, U., Girard-Lauriault, P.-L., Meunier, J.-L., Boudreault, R. & Tavares, J. R. Experimental and theoretical assessment of water sorbent kinetics. *Langmuir* **38**, 2651–2659 (2022).
57. Poredoš, P., Shan, H., Wang, C., Deng, F. & Wang, R. Sustainable water generation: Grand challenges in continuously atmospheric water harvesting. *Energy Environ. Sci.* **15**, 3223–3235 (2022).
58. Zhang, Y. & Tan, S. C. Best practices for solar water production technologies. *Nat. Sustain.* **5**, 554–556 (2022).
59. Poredoš, P. et al. Condensation of water vapor from humid air inside vertical channels formed by flat plates. *Iscience* **25**, 103565 (2022).
60. Qi, H. et al. An interfacial solar-driven atmospheric water generator based on a liquid sorbent with simultaneous adsorption–desorption. *Adv. Mater.* **31**, 1903378 (2019).
61. Stoeckli, H. F., Kraehenbuehl, F., Ballerini, L. & De Bernardini, S. Recent developments in the Dubinin equation. *Carbon* **27**, 125–128 (1989).

Acknowledgements

This research work was funded by the Foundation for Innovative Research Groups of the National Natural Science Foundation of China (No. 51521004). We thank Prof. Jinping Li and Mr. Rui Li at the Lanzhou University of Technology for their help.

Author contributions

H.S., C.L. designed the prototype and synthesized the sorbents. H.S., Z.Y., and Z.C. carried out the experiments and analyzed the experimental data. W.Y., J.W. conducted the simulation. H.S., Q.P., P.P., R.W. prepared the manuscript. All authors contributed to the final version. R.W. and Q.P. conceived the idea and led the project.

Competing interests

The authors declare no competing interests.

Additional information

Supplementary information The online version contains supplementary material available at https://doi.org/10.1038/s41467-022-33062-w.

Correspondence and requests for materials should be addressed to Quanwen Pan or Ruzhu Wang.

Peer review information *Nature Communications* thanks Yufei Zhang and the other, anonymous, reviewer(s) for their contribution to the peer review of this work. Peer reviewer reports are available.

ADVANCED MATERIALS
www.advmat.de

All-Day Multicyclic Atmospheric Water Harvesting Enabled by Polyelectrolyte Hydrogel with Hybrid Desorption Mode

Sorption-based atmospheric water harvesting (AWH) is a promising approach for mitigating worldwide water scarcity. However, reliable water supply driven by sustainable energy regardless of diurnal variation and weather remains a long-standing challenge. To address this issue, a polyelectrolyte hydrogel sorbent with an optimal hybrid-desorption multicyclic-operation strategy is proposed, achieving all-day AWH and a significant increase in daily water production. The polyelectrolyte hydrogel possesses a large interior osmotic pressure of 659 atm, which refreshes sorption sites by continuously migrating the sorbed water within its interior, and thus enhancing sorption kinetics. The charged polymeric chains coordinate with hygroscopic salt ions, anchoring the salts and preventing agglomeration and leakage, thereby enhancing cyclic stability. The hybrid desorption mode, which couples solar energy and simulated waste heat, introduces a uniform and adjustable sorbent temperature for achieving all-day ultrafast water release. With rapid sorption–desorption kinetics, an optimization model suggests that eight moisture capture–release cycles are capable of achieving high water yield of 2410 mL_{water} $kg_{sorbent}^{-1}$ day^{-1}, up to 3.5 times that of single-cyclic non-hybrid modes. The polyelectrolyte hydrogel sorbent and the coupling with sustainable energy driven desorption mode pave the way for the next-generation AWH systems, significantly bringing freshwater on a multi-kilogram scale closer.

1. Introduction

Two-thirds of the worldwide population is living in water-scare regions.[1] Freshwater scarcity has become an urgent global challenge threatening the sustainable development of humankind.[2] The atmospheric water resource is estimated to be 12 900 cubic kilometers, accounting for up to ≈10% of freshwater sources on Earth.[3] Sorption-based atmospheric water harvesting (AWH) has been regarded as a promising approach to alleviate the water shortage, achieving freshwater production in a wide range of relative humidity (RH), especially in the low RH (RH<60%) environment owing to the high water affinity of sorbents for capturing water molecules from the air.[4] Sorbents can spontaneously capture water in the air by sorption and release it due to the local RH differences. The sorption performance of sorbents determines the water harvesting limit of AWH systems; thus, the design and development of sorbents have attracted enormous attention and promoted the overall AWH performance in the aspects of water uptake capacity, kinetics, and stability.[5]

Among various sorbents, metal–organic frameworks (MOFs) are considered to offer great potential for efficient AWH because of their adjustable S-shape isotherm.[6] MOF-801 [$Zr_6O_4(OH)_4$(fumarate)$_6$] with the steep increase in water uptake at an extremely low RH range shows the superior potential in water harvesting in arid areas where RH is merely 20%.[3a] Cr-soc-MOF-1 offers an extremely high apparent surface area of 4549 m^2 g^{-1} and unique vapor sorption properties of 1.95 g g^{-1} at 70% RH, but the observed shift in the water desorption branch to a relatively lower pressure should be considered for low energy demand water release.[7] In addition, Al-based MOFs (MIL-96(Al) and MIL-100(Al)) can be in situ synthesized utilizing metal ions from the aluminum substrates, obtaining superior heat and mass transfer potentials that could be combined with industrial heat exchangers.[8] However, the limited adaptability of MOF to changes in environmental RH, along with stronger temperature dependence of the vapor sorption isotherm, the difficulty and expensive large-scale synthesis, as well as larger deterioration of heat and mass transfer after modularization have hindered the wider applications in practical scalable water harvesters.[9]

Department of Materials Science and Engineering
National University of Singapore
9 Engineering Drive 1, Singapore 117574, Singapore
E-mail: msetansc@nus.edu.sg

Institute of Refrigeration and Cryogenics
Shanghai Jiao Tong University
800 Dongchuan Road, Shanghai 200240, China
E-mail: rzwang@sjtu.edu.cn

Engineering Research Center of Solar Power & Refrigeration
MOE China
Shanghai 200240, China

China-UK Low Carbon College
Shanghai Jiao Tong University
3 Yinlian Road, Shanghai 201306, China

The ORCID identification number(s) for the author(s) of this article can be found under https://doi.org/10.1002/adma.202302038

DOI: 10.1002/adma.202302038

Hygroscopic salt-embedded composite materials (HSCM) that are synthesized by the facile embedding process of the hygroscopic salt (e.g., lithium chloride (LiCl)) into the matrix, have been widely investigated in AWH systems, particularly for scale-up applications.[10] Such materials show advantages in low-cost fabrication, facile and scalable preparation methods, and strong adaptability over wide air humidity ranges (≈10–100%). Porous matrices, made from materials such as hydrogels,[11] MOFs,[12] fibers,[4,13] and sponges,[14] are used to expand the reaction surface area between moisture and hygroscopic salts, which accelerates sorption kinetics and makes HSCM suitable for daily multiple AWH cycles. Importantly, these porous materials have been extensively studied in various fields and offer numerous design options for AWH materials,[15] which makes HSCM a highly promising material platform for efficient AWH.[16] Among various HSCM, hydrogel-based HSCM with soft and expandable polymeric networks are regarded as the next-generation sorbents owing to their unique swelling and water storage properties of polymeric gel matrices.[11,17] Although the thermally responsive hydrogel PPy-Cl-PNIPAM has shown exceptional water uptake under high humidity (6.7 g g^{-1} at 90% RH),[18] only after the incorporation of hygroscopic salts in the hydrogels, the water uptake ability in the low-RH environment has been demonstrated and improved.[19]

The hydrogel-based HSCM sorption process begins with the embedded hygroscopic salts first capturing the water vapor, which are then in situ to liquify the water molecules on the hydrogel surface. After that, the liquified water is transferred inside the polymeric networks by osmotic pressure differences and is stored owing to the unique swelling property. The surface moisture-capture sites are re-exposed for subsequent sorption. Thus, the migration of water driven by osmotic pressure and its following retention resulting from swelling are defining features that distinguish hydrogel-based sorbents from other sorbents. The swelling properties and the interior osmotic properties of hydrogel facilitate enhancing water storage and migration, thereby significantly affecting the sorption capacity and kinetics of the material.[18,20] However, the interior osmotic pressure of recently developed nonionic hydrogels is much lower than that of the hygroscopic salt solution generated during sorption,[21] resulting in the reduction or even loss of the swelling property of nonionic hydrogels, thereby affecting the water transport and storage performance.[16a,22] Besides, nonionic hydrogels with uncharged polymer chains have no interactions with embedded hygroscopic salts, thus salts exist as the free state that has fast mobility in the soft hydrogel–salt system[23] (**Scheme 1**a), which can cause the risk of salt leakage and salt agglomeration after several sorption–desorption cycles.[24]

Different from the nonionic hydrogels, polyelectrolyte hydrogels with cationic or anionic groups on the polymeric chains, such as the cationic hydrogel poly(2-acrylamido-2-methyl-1-propanesulfonic acid) (PAMPS), are promising hydrogel-based matrices[26] (Scheme 1b), because their charged polymer chains found inside the polyelectrolyte hydrogels show strong electrostatic interaction and demonstrate high osmotic pressure of hundreds of atm.[27] They show a large swelling ratio of several thousand in pure water and maintain the swelling ratio of tens to hundreds in a salt solution that is generated during the sorption process. The high interior osmotic pressure and generated gradient during sorption are expected to facilitate the rapid transport of sorbed water molecules into the interior of hydrogel and refresh the surface water sorption sites[28] (Scheme 1c). Meanwhile, the charged polymer chain could confine the oppositely charged hygroscopic ions and form coordinated salts, which is expected to limit the mobility of salts and controls the solution leakage.[29] Therefore, the unique polyelectrolyte hydrogel with high interior osmotic pressure could be a candidate to improve the water transport and storage performance, prevent solution leakage and finally obtain excellent water uptake performance for efficient AWH.

Beyond the sorbent materials, the overall AWH performance is considerably affected by the operation strategy and energy sources for driving the desorption. The diurnal single capture–release cycle causes a waste of time due to the mismatch of sorption and desorption rates while adopting an active multicyclic or batch-processed mode can maintain high water harvesting rates, successfully pushing the water production yield into over 1 L $kg_{sorbent}^{-1}$ day^{-1}.[5,30] However, the optimization of sorption and desorption duration for multicyclic and batch-processed water harvester still needs to be precisely adjusted.[4] Furthermore, atmospheric humidity is a widespread water resource, whereas available energy for driving water release is always influenced by the locations.[31] Low-grade thermal energy, for example, the waste heat discharged from car engines, factory exhausts, and air conditioners, can be recovered and stored to continuously drive water release and water production[32] (Scheme 1d). Particularly, the waste heat with a temperature below 100 °C shares the largest proportion in the residential heat exhaust and transportation[25] (Scheme 1e), which particularly meets the energy grade required for desorption. More importantly, waste heat can be seen as an energy supplement to solar energy to achieve a hybrid desorption mode. This kind of mode is expected to obtain a more uniform and controllable desorption temperature of the sorbent for more efficient water release. Also, such an approach could realize commendable all-day water production regardless of climate and diurnal variations.

Herein, we develop a cationic polyelectrolyte hydrogel sorbent embedded by the free LiCl and coordinated LiCl to achieve all-day water harvesting by employing the multicyclic water capture–release strategy and the hybrid desorption mode. The hygroscopic gel was fabricated by embedding the hygroscopic LiCl and photothermal carbon nanotubes (CNT) into the polyelectrolyte hydrogel (PAMPS) networks, achieving the surprisingly large interior osmotic pressure of ≈659 atm and the satisfactory swelling ratio of 58.1 g g^{-1} for water migration and retention. The negatively charged sulfonic groups in polymer chains form strong electrostatic interactions with salt species (SO^{3-}–Li^{+}), achieving the anchoring of salt ions and effectively preventing salt aggregation and leakage. The remaining uncoordinated free LiCl contributed to further improvement of the water capacity. The hydrogel sorbents show a water uptake capacity of 0.65, 1.00, and 1.87 g g^{-1} at the RH of 15%, 30%, and 60% RH, respectively, without the risk of solution leakage. Moreover, with fast sorption–desorption kinetics, 70% of the water was adsorbed and released within the initial 150 and 20 min, respectively. To fully utilize the AWH performance, we adopted a multicyclic water capture–release operation strategy and employed a hybrid desorption mode based on simulated waste heat and solar energy. The waste

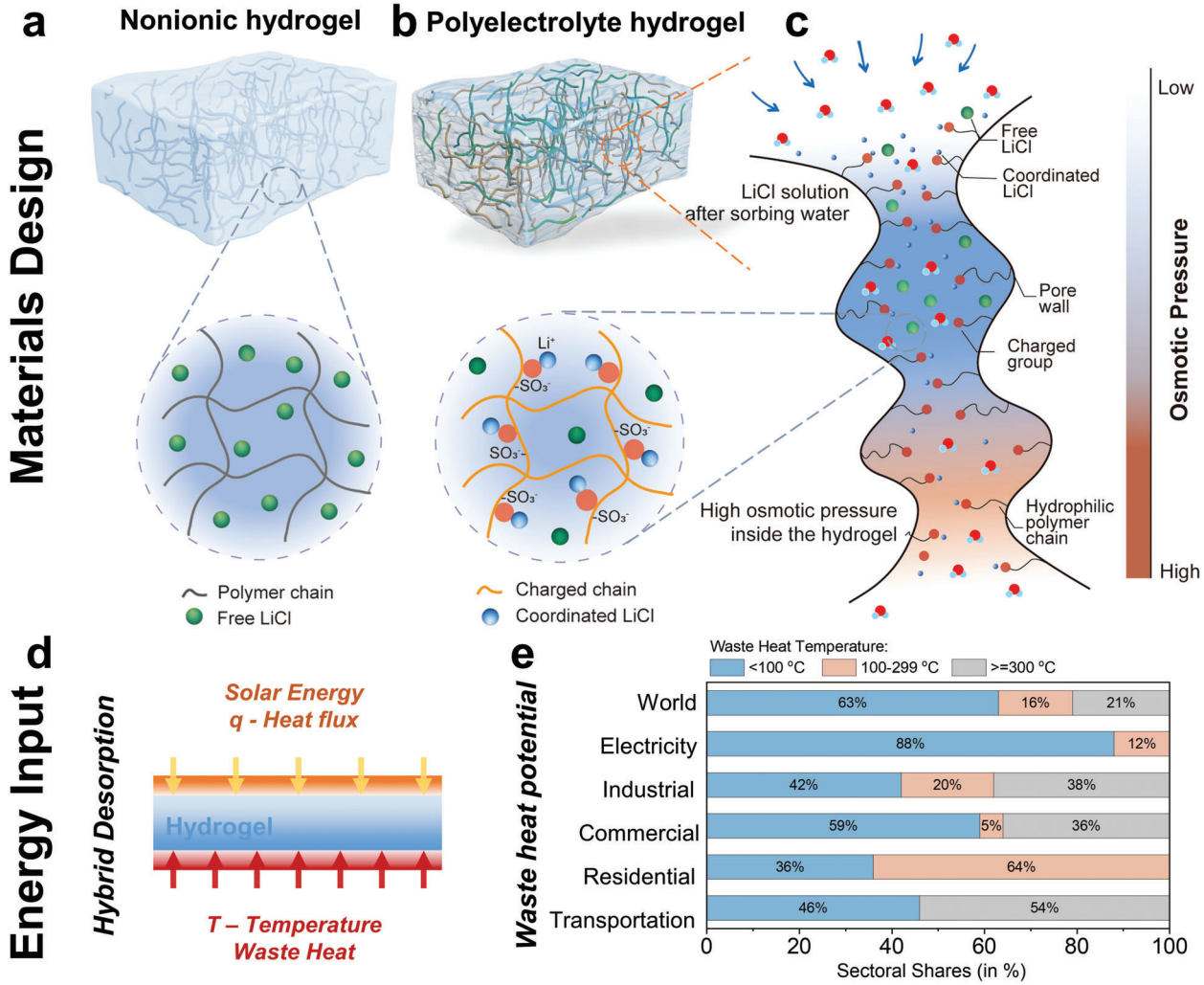

Scheme 1. Schematic of a hydrogel-based material platform for atmospheric water harvesting driven by sustainable waste heat and solar energy. a) Schematic of a nonionic hydrogel and free LiCl without interaction with uncharged polymeric chains. b) Schematic of a polyelectrolyte hydrogel with coordinated LiCl and oppositely charged hydrophilic polymeric chains. c) Schematic of efficient water sorption, transport, and storage inside the polyelectrolyte hydrogel. Water vapor is captured by the free and coordinated LiCl on the surface of the pore walls, and then the captured water molecules within the generated LiCl solution are pulled and permeated into the interior of hydrogel due to the strong osmotic pressure differences, promoting the transfer and retention of the sorbed water. d) Schematic of hybrid desorption mode coupling waste heat and solar energy for water release. e) Global waste heat potential across all sectors for driving desorption.[25]

heat is available all the time, consequently allowing desorption to extend to the nighttime and realizing all-day multicycle water production. The sorption–desorption durations over the day were optimized by the established numerical models and optimization algorithms. With these optimizations, the lab-tested water harvester achieved high-yield water production of up to 2410 mL_{water}^{-1} $kg_{sorbent}^{-1}$ day^{-1}, which is 3.5 and 2.5 times compared to the single-cyclic solar-driven photothermal mode and waste heat-driven mode, respectively.

2. Results and Discussion

2.1. Preparation and Characterization of PAMPS-CNT-LiCl

The hydrogel sorbent PAMPS-CNT-LiCl was fabricated by free-radical polymerization with the addition of CNT in the precursor solution and followed by immersing it in LiCl solution to embed the LiCl hygroscopic salt (**Figure 1**a). The optimal cross-linking degree was determined by varying the mass ratio of the cross-linker (MBAA) to monomer (AMPS). The resulting mechanical properties, swelling capacity, and successful cross-linking of the hydrogels were then evaluated. It shows that successful gelation occurs once the concentration of the cross-linker is higher than 0.5 wt% (Figure S1, Supporting Information). The as-prepared PAMPS hydrogels show a remarkable maximum water absorbency (e.g., the swelling ratio) of 1379 g g^{-1} at the lowest cross-linker ratio of 0.5 wt% owing to the large osmotic pressure generated by the electrostatic repulsion of the sulfonate groups in the polymeric chains based on the Flory–Rehner theory (Figure S2, Supporting Information).[33] However, the mechanical properties of the hydrogel became unacceptable at such a high degree of swelling. Thus, we further evaluated the mechanical properties

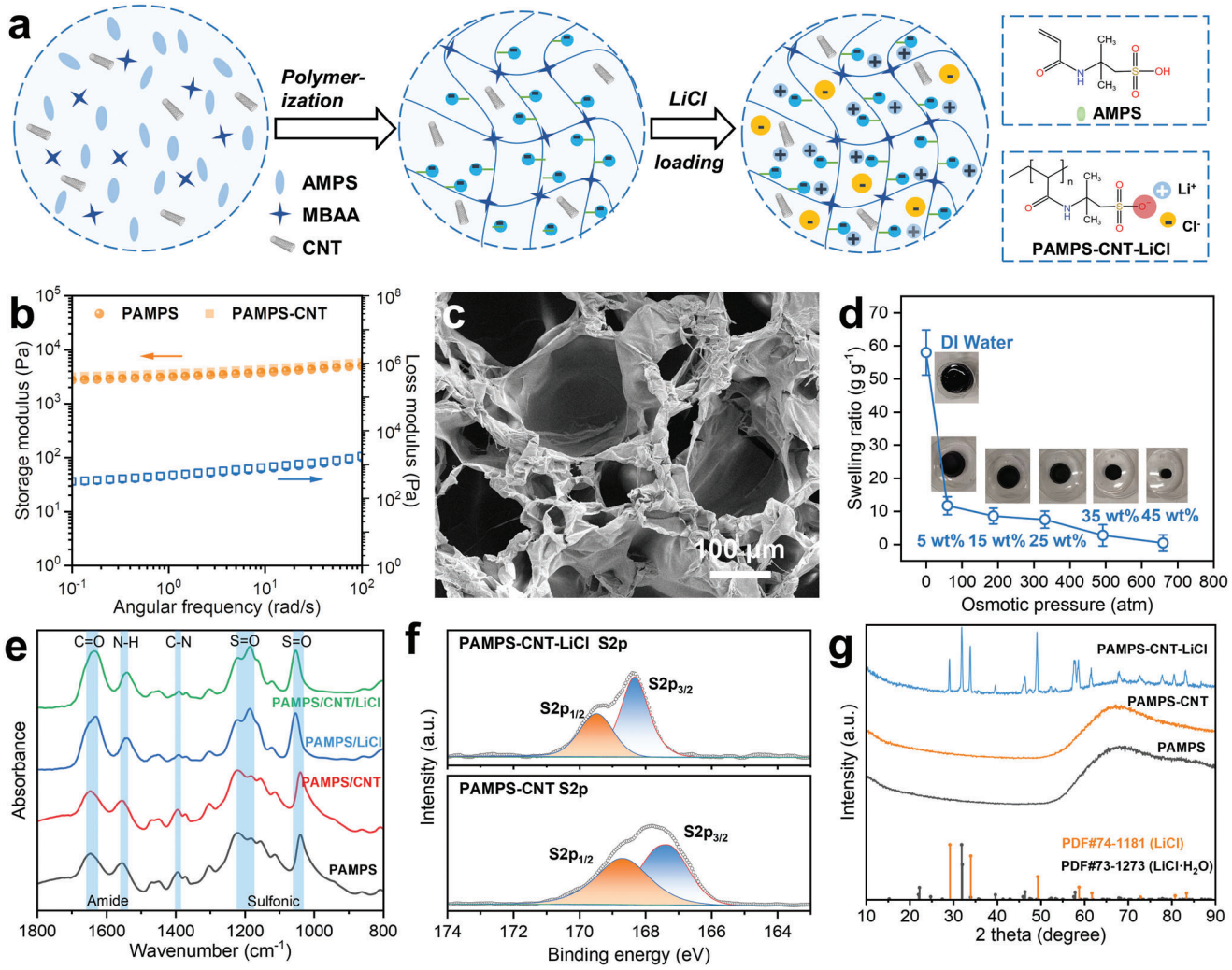

Figure 1. Preparation and characterization of the PAMPS-CNT-LiCl hydrogel sorbent, the free and coordinated LiCl. a) Schematic representation of the fabrication process of PAMPS-CNT-LiCl hydrogel. b) Dynamic mechanical analysis showing the storage modulus (G') and loss modulus (G'') for the PAMPS and PAMPS-CNT hydrogel, demonstrating successful crosslinking. c) SEM image of PAMPS hydrogel illustrating the macroporous structure with a pore size of 5–100 μm. d) Swelling ratios of the PAMPS-CNT hydrogel when immersed in LiCl solution with different concentrations, demonstrating the high osmotic pressure of the prepared hydrogels. e) FTIR spectra of hydrogels, showing the significantly shifted peak that represents the S=O stretching vibration. f) High-resolution S2p XPS spectra of PAMPS-CNT and PAMPS-CNT-LiCl hydrogel, indicating the peak location and intensity shifts of the sulfonic group. g) XRD patterns of hydrogels, showing the amorphous PAMPS phase and the sharp peaks contributed by LiCl and LiCl·H_2O crystals.

of PAMPS-CNT and finally identified the optimal cross-linker ratio of 10 wt% (Figure S3, Supporting Information). At the specified ratio, the hydrogel maintains its solid form and shows structural integrity even after swelling to 64 times its original volume when immersed in water. Moreover, it demonstrates sufficient strength and mechanical properties without exhibiting a liquid-like appearance or disintegrating.

The successful cross-linking and the viscoelastic mechanical properties of PAMPS and PAMPS-CNT were investigated by measuring the energy storage and dissipation characteristics of the as-prepared hydrogels. As shown in Figure 1b, the higher values of storage modulus (G') of both hydrogels compared with their loss modulus (G'') at the entire frequency range confirmed the successful formation of the cross-linked hydrogel networks.[34] The slightly higher G' and G'' values of PAMPS-CNT hydrogel than those of the pure PAMPS hydrogel confirm the extra physical cross-linking points between CNT and polymeric chains.[35] The as-prepared PAMPS and PAMPS-CNT after freeze-drying have a macroporous network structure with pore size spanning from several to hundreds of micrometers (Figure 1c; Figure S4, Supporting Information). The pores serve as the water transfer channels and are expected to expand or shrink during sorption and desorption for accelerating water transport. The smaller pore width and rough pore walls are obtained after doping the CNT into polymeric networks, indicating the successful integration of CNT (Figure S5, Supporting Information) and the enlarged surface area (Figure S6, Supporting Information), which is beneficial for the further attachment of the free LiCl. The smaller pore width observed in PAMPS-CNT hydrogels can be attributed to the higher cross-linking

degree resulting from additive physical cross-linking between CNT and PAMPS. This higher cross-linking degree, in turn, leads to a slightly reduced swelling ratio of PAMPS-CNT compared to pure PAMPS (Figure 1d). Additionally, energy-dispersive X-ray spectroscopy (EDS) elemental mapping confirmed the uniform construction of the polymeric networks and CNT embedding (Figure S7, Supporting Information). Especially, the uniformly distributed sulfonic groups could be linked onto the framework and evenly confined Li^+ in the pores.

The as-prepared PAMPS-CNT hydrogels were immersed in the LiCl solution with the mass fractions of 5–45 wt% to endow the hygroscopicity. As shown in Figure 1d; Figure S8 (Supporting Information), the swelling ratio of PAMPS-CNT hydrogels decreases from 58.1 g g^{-1} in DI water with an increase in the mass fraction of LiCl due to ion migration and equilibrium caused by osmotic pressure difference, as well as reduced electrostatic repulsion between charged polymeric chains due to the presence of counter ions (Li^+).[36] The PAMPS-CNT hydrogel exhibits strong internal osmotic pressure and loses its swelling capacity only at a LiCl concentration of 45 wt%, which is much higher than non-ionic hydrogels. Based on the van't Hoff theory and the thermodynamic equilibrium state between the hydrogel and the LiCl solution (see Experimental Section), the osmotic pressure of PAMPS-CNT-LiCl is calculated as ≈659 atm while the value of common nonionic hydrogel is below 30 atm.[28a,37] Therefore, the cationic polyelectrolyte hydrogel demonstrates an improvement of 1–2 orders of magnitude compared to the non-ionic hydrogel for efficient water transport and storage. In addition, the high interior osmotic pressure allows the hydrogel facilely to load the hygroscopic salt LiCl by an immersing-drying process without freeze-drying. The total LiCl content of PAMPS-CNT-LiCl was carefully evaluated by the thermogravimetric analyzer (TGA) (Figure S9, Supporting Information), and the hydrogel with a LiCl content of ≈53% was chosen, as no salt agglomeration was observed (Figure S10, Supporting Information).

LiCl dissociates into ions when it is introduced into the hydrogel network. Of all the alkali metal cations, the lithium-ion is the smallest with a radius of 0.59 Å and the highest charge density of 1.86×10^{11} C m^{-3}, showing high capacity to accept non-bonding electron pairs.[38] The sulfonate group has a high ionization capacity, and its oxygen atom shows the high electronegativity to donate electrons.[29b,39] Thus, the lithium-ion forms an electrostatic complex with the sulfonate group on the polyelectrolyte hydrogel PAMPS, which allows the polymer chains to evenly anchor and distribute the lithium ions.[20,40] The portion of LiCl that is bound by the sulfonate group via electrostatic interactions is referred to as coordinated LiCl. The binding energy of this complex depends on the distance between the Li^+ ion and the sulfonate group, as well as the orientation of the sulfonate group relative to the Li^+ ion.[36] The presence of sulfonate–Li^+ coordination complex within the hydrogels is confirmed by the Fourier-transform infrared (FTIR) spectra, which show the significantly shifted peak that represents the S=O stretching vibration[41] (Figure 1e). The high-resolution S 2p X-ray photoelectron spectroscopy (XPS) spectra showed a shift to higher binding energies and a change in intensity attributed to salt coordination, which also confirmed the interaction between PAMPS-CNT and coordinated salts.[42] (Figure 1f; Figure S11, Supporting Information). The rest of the salt without interaction with polymer chains could be considered as free salt. The successful loading of free LiCl is confirmed by the X-ray diffraction (XRD) patterns of PAMPS-CNT-LiCl (Figure 1g), showing the broad peak at ≈70° that corresponds to the amorphous PAMPS phase and the sharp peaks contributed by the hygroscopic LiCl and $LiCl{\cdot}H_2O$ crystals with the state of free salt. XRD patterns of PAMPS-CNT-LiCl during the sorption process were collected to understand the variation of the free LiCl crystals. As shown in Figure S12 (Supporting Information), the dry sorbent exhibits significant peaks that correspond to LiCl and $LiCl{\cdot}H_2O$. After 5 min sorption, the peaks of LiCl disappeared and only $LiCl{\cdot}H_2O$ remains with weak signals, indicating all anhydrous LiCl captured water and formed the $LiCl{\cdot}H_2O$. $LiCl{\cdot}H_2O$ continued absorbing water and gradually dissolved forming the salt solution. After 10 min, no sharp peaks were found, implying all salt was dissolved in the salt solution and started the solution absorption.

Furthermore, the mechanical properties and adhesion properties of the prepared sorbent need to be considered for potential practical applications. The cyclic compression tests showed that both PAMPS and PAMPS-CNT-LiCl could immediately recover their initial shape after being released and PAMPS hydrogel could be stretched to over four times its original length without breaking (Figure S13, Supporting Information). After additions of LiCl and CNT, PAMPS hydrogel showed reduced mechanical strength, but a long strain of ≈200% and maximum compression stress of ≈0.15 MPa remain, demonstrating the good extensibility, toughness, and self-recovery ability of both hydrogels. In addition, the PAMPS-CNT-LiCl hydrogel sorbent exhibits remarkable adhesion properties to both metallic and non-metallic surfaces, without requiring any additional physical or chemical treatments, making it a promising candidate for integration with a wide range of existing mature engineering technologies (Figure S14, Supporting Information).[31,41b]

2.2. Water Vapor Sorption–Desorption Performance of PAMPS-CNT-LiCl

The coordinated and free LiCl jointly contributed to the water uptake capacity, kinetics, and stability of the hydrogel sorbent. As shown in **Figure 2**a, PAMPS-CNT-LiCl shows the water uptake of 0.65, 1.00, 1.87, 5.45 g g^{-1} for 15%, 30%, 60%, and 90% RH at 25 °C, respectively. This demonstrates the excellent sorption capacity and strong environment adaptability of PAMPS-CNT-LiCl in a wide range of RHs. The equilibrium isotherm line slightly moves to the right when comparing the isotherm at 25 °C to the one at 60 °C due to the LiCl–water thermodynamic characteristics.[43] The sorption–desorption kinetics of PAMPS-CNT-LiCl were evaluated by a dynamic vapor sorption analyzer (DVS) with a dry gas flow rate of 120 mL min^{-1} (Figure S15, Supporting Information)). Four typical RHs from 15% to 90% were selected to comprehensively estimate the sorption behavior of the hydrogel. The results show that the water uptake at the low and middle RHs of 15% to 60% almost reaches equilibrium within the first 200 min (Figure 2b), which exhibits faster kinetics compared to non-ionic hydrogels (Figure S16, Supporting Information). The rapid sorption kinetics observed in the hydrogel can be explained by the significant osmotic pressure gradient that exists between the surface and interior regions. When the

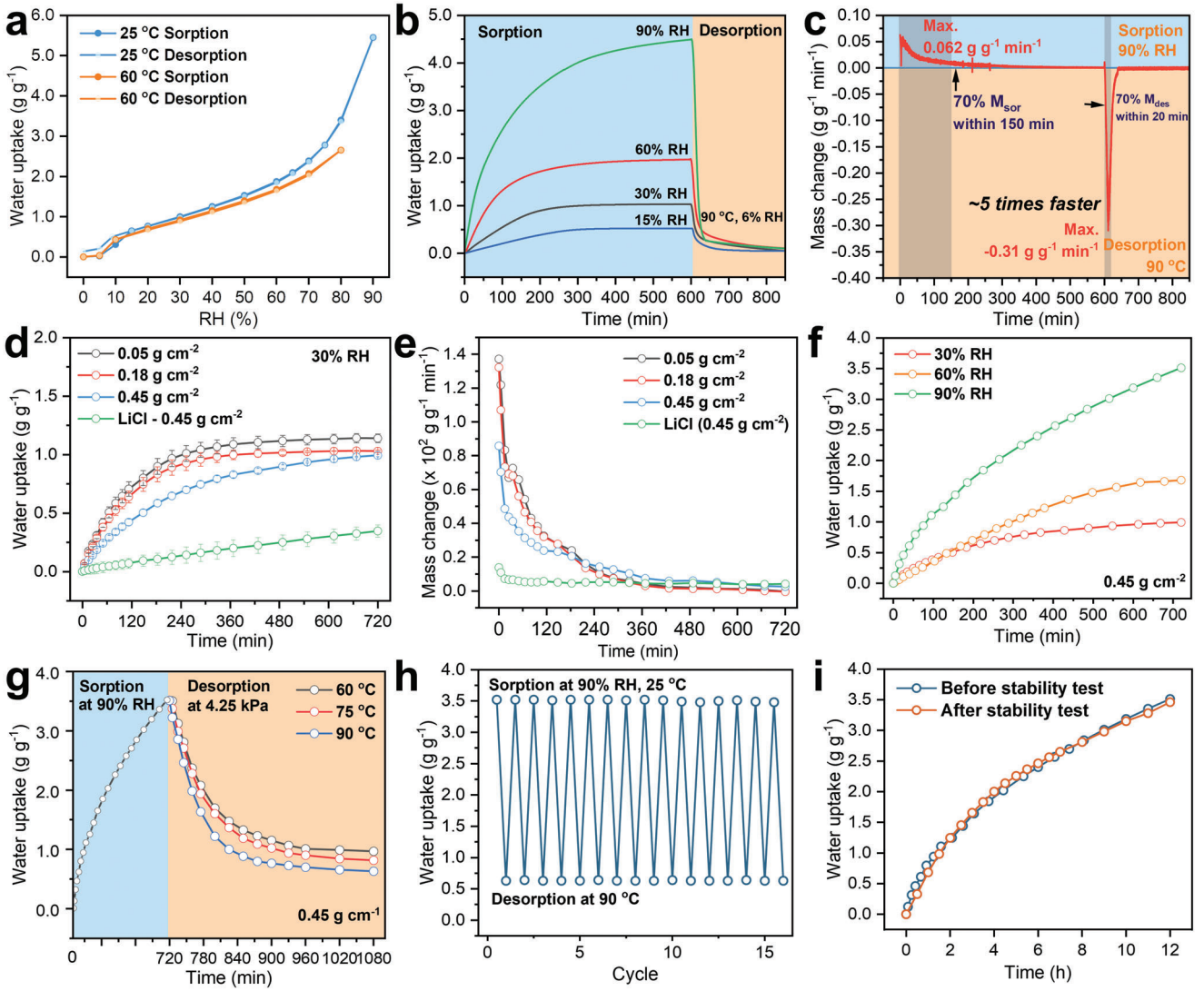

Figure 2. Water vapor sorption–desorption performance of PAMPS-CNT-LiCl. a) Water sorption isotherms at 25 and 60 °C. b) DVS curves displaying the dynamic water sorption process of PAMPS-CNT-LiCl under different working conditions of 15% RH, 30% RH, 60% RH, and 90% RH at 30 °C and the dynamic water desorption process under 6.0% RH at 90°C (4.2 kPa). c) Derivative water uptake changes of the milligram-scale sample at 30% RH, highlighting the discrepancy between sorption and desorption time. d) Dynamic sorption curves of bulk PAMPS-CNT-LiCl samples and LiCl with different specific weights tested in the humidity chamber at 25 °C, 30% RH, showing the effect of the sample size on sorption kinetics. e) Derivative water uptake changes of the bulk samples at 30% RH. f) Dynamic sorption curves of bulk PAMPS-CNT-LiCl sample with the specific weight of 0.45 g cm^{-1} tested at different RHs of 30%, 60% RH, and 90% RH at 30 °C. g) Dynamic desorption curves of bulk PAMPS-CNT-LiCl sample with the specific weight of 0.45 g cm^{-1} at 60, 75, 90 °C and 4.2 kPa, respectively. h) Fifteen water sorption–desorption cycling tests carried out at 25°C, 90% RH for sorption and 90 °C, 4.2 kPa for desorption, indicating satisfactory water sorption–desorption cycling stability. i) Dynamic sorption curves at 90% RH before and after the cycling tests demonstrating no deterioration of the sorption kinetic performance.

hydrogel sorbs water, the osmotic pressure of the surface layer decreases while the internal region maintains a high osmotic pressure, creating a large gradient that drives the sorption process. Additionally, the 3D porous structure of hydrogel contains sulfonic groups that anchor lithium ions to the walls. This anchoring effect means that during sorption, only the water molecules that are already sorbed undergo fast migration in the 3D porous channels, while the surface hygroscopic sites remain predominantly unsaturated and available for subsequent sorption. This further contributes to the rapid sorption kinetics of the hydrogel sorbent. For high RH condition, due to the strong water sorption capacity in humid environments (90% RH), the sorbent can reach 80% (4.49 g g^{-1}) of the equilibrium water uptake capacity (5.45 g g^{-1}) within 600 min. Although the fast sorption kinetics has obtained owing to the osmotic pumping effect, the sorption kinetic is still far lower than that of desorption. Over 90% (4.25 g g^{-1}) of the sorbed water at 90% RH can be released within the first 60 min, indicating that only ≈1/5 maximum sorption rate (0.062 g g^{-1} min^{-1}) compared to the maximum desorption rate (0.31 g g^{-1} min^{-1}) was observed as shown in Figure 2c.[4] In addition to the imbalance between sorption and desorption, the rates of these processes are also significantly different in the

early and late stages. Seventy percent of the water is adsorbed and released within the first 150 and 20 min, respectively, leaving only a small amount (30%) of water for sorption and release during the remaining time. These mismatches among sorption and desorption rates appear to be widespread in previously reported sorbents,[44] motivating us to balance it from the aspect of operation strategies (e.g., batch-processed[4] or multicyclic AWH[30a,45]) to pursue daily high-yield water production.

The other easily overlooked aspect is related to the decrease of kinetics between milligram-level samples with ideal gas flow conditions and gram-scale ones in practical environments[46] (Figure S17, Supporting Information). To evaluate the practical sorption characteristics and optimize the multicyclic mode more accurately, we measured the samples with three various specific weights at the humidity chamber with the RHs of 30, 60, and 90% (Figure S18, Supporting Information). Figure 2d shows that the slower kinetics were obtained with the increasing specific weights (i.e., thickness) of PAMPS-CNT-LiCl hydrogels, and this reduction trend is significantly accelerated as the further increase of the thickness because the resistance of both the vapor and liquid transport decreases significantly with the thickness. Also, note that the LiCl particles with a specific weight of 0.45 g cm^{-2} can hardly reach sorption equilibrium within 12 h. As shown in Figure 2e, the mass change of PAMPS-CNT-LiCl shows significantly higher values than that of pure LiCl particles, because of the continuous refreshing by pulling the captured water molecules into the interior of the hydrogel. Additionally, the almost same sorption characteristics of PAMPS-CNT-LiCl and PAMPS-CNT were observed (Figure S19, Supporting Information), showing that CNT has an almost negligible effect on the sorption behavior. In addition to the RH of 30%, Figures S20 and S21 (Supporting Information) present the sorption curves of the bulk PAMPS-CNT-LiCl samples with varying thicknesses under controlled RHs of 60% and 90%, respectively.

We selected the PAMPS-CNT-LiCl sample with the specific weight of 0.45 g cm^{-1} for further study to be closer to the practical system-level AWH situations. The dynamic sorption curves of the bulk sample are shown in Figure 2f, showing the 12 h water uptake of 0.99, 1.68, 3.51 g g^{-1} for 30%, 60%, and 90% RH at 25 °C, respectively. The dynamic desorption curves at the vapor pressure of 4.25 kPa indicate the efficient water release of 70% of the sorbed water within 4 h and thus reaching the water uptake of 0.97 g g^{-1} at the mild heating condition with 60 °C (Figure 2g). The results prove that the excellent sorption–desorption performance can still meet the requirements of the actual AWH situation with a wide range of RHs and driven by natural sunlight and/or low-grade waste heat, although the performance degradation occurs when using the bulk samples.

The water sorption–desorption stability of bulk PAMPS-CNT-LiCl is measured by 15 continuous sorption–desorption cycling tests in the humidity chamber at an extremely high RH of 90%. Figure 2h confirmed the satisfactory working stability at equilibrium water uptake even at such high RH. The stability of the kinetics can also be maintained after the cycling tests (Figure 2i). The salt solution leakage phenomenon was not observed (Figure S22, Supporting Information), and no salt agglomeration on the surface of the hydrogel after desorption was found (Figure S23, Supporting Information). This is because the coordinated salt is uniformly anchored by the charged polymer chains, which prevents the migration and aggregation of salt ions.[20,36] The remaining salt ions strongly coordinate with the water molecules and binding with chloride ions after water sorption, significantly limiting their migration within the hydrogel.[47] As a result, the hydrogel sorbent shows the potential for long-term utilization for water harvesting and production in practical application.

2.3. Coupled Energy-Driven Hybrid Desorption Performance

Low-grade waste heat is abundant worldwide from various sources. This waste heat can serve as alternative or supplementary energy source with solar energy to drive the desorption process for freshwater production, providing an eco-friendly and carbon-free solution. Using both solar energy and waste heat enables the desorption process to operate day and night, regardless of natural sunlight intensity fluctuations. Meanwhile, coupled solar energy and waste heat, both as the desorption-driven energy sources, provide the possibility to extend the desorption process into the nighttime and can also be used regardless of the fluctuation of natural sunlight intensity. Moreover, we analyzed the thermodynamic and heat and mass transfer characteristics of the hydrogel sorbent and found that coupling bottom waste heat with fixed temperature and top solar interfacial heating with a constant heat flux (**Figure 3**a) can increase the internal temperature of the hydrogels and eliminate the temperature difference, which significantly enhances the desorption rate.

We selected the desorption degree and the desorption rate to study the difference amount the interfacial solar energy (SE) driven desorption, the bottom waste heat-driven desorption, and the hybrid mode, because these parameters are reflective of the quality (temperature) and quantity of the energy source. The desorption degree is defined as the proportion of water that can be released from the total sorbed water when the desorption reaches equilibrium. The simulated waste heat (SWH) source with constant temperatures of 50, 60, 75, and 90 °C is arranged in the bottom of the sorbent, which was accomplished in the lab using an electrically driven Joule heater with PID feedback, without the need for costly piping, heat exchangers, or water storage. Additionally, the interfacial photothermal conversion occurred at the top of the sorbent simultaneously with the availability of solar energy input.

The desorption rate and degree driven by solely interfacial solar heating (refer as SE-driven) are studied by exposing hydrogels that sorbed at 90% RH to different solar radiation intensities. The hydrogel sorbent exhibits a water release of 2.18, 2.39, 2.44, and 2.60 g g^{-1} under solar intensities of 0.6–1.2 kW m^{-2} within the initial 4 h period (Figure 3b). Over 60% and 80% of captured water are released within 4 h and within 10 h at the lowest solar intensity of 0.6 kW m^{-2}, respectively, demonstrating the heating effect (Figure S24, Supporting Information) induced by the wide solar absorption band provided by CNTs in the sorbent (Figure S25, Supporting Information). Besides, the desorption process was approaching equilibrium within 10 h, with the first 4 h characterized by a rapid release of water followed by a very slow release rate for the remaining six h. This is consistent with the modeling results of previous studies, as the gradual decrease in water content within the hydrogel leads to a reduction in the water concentration gradient.[48]

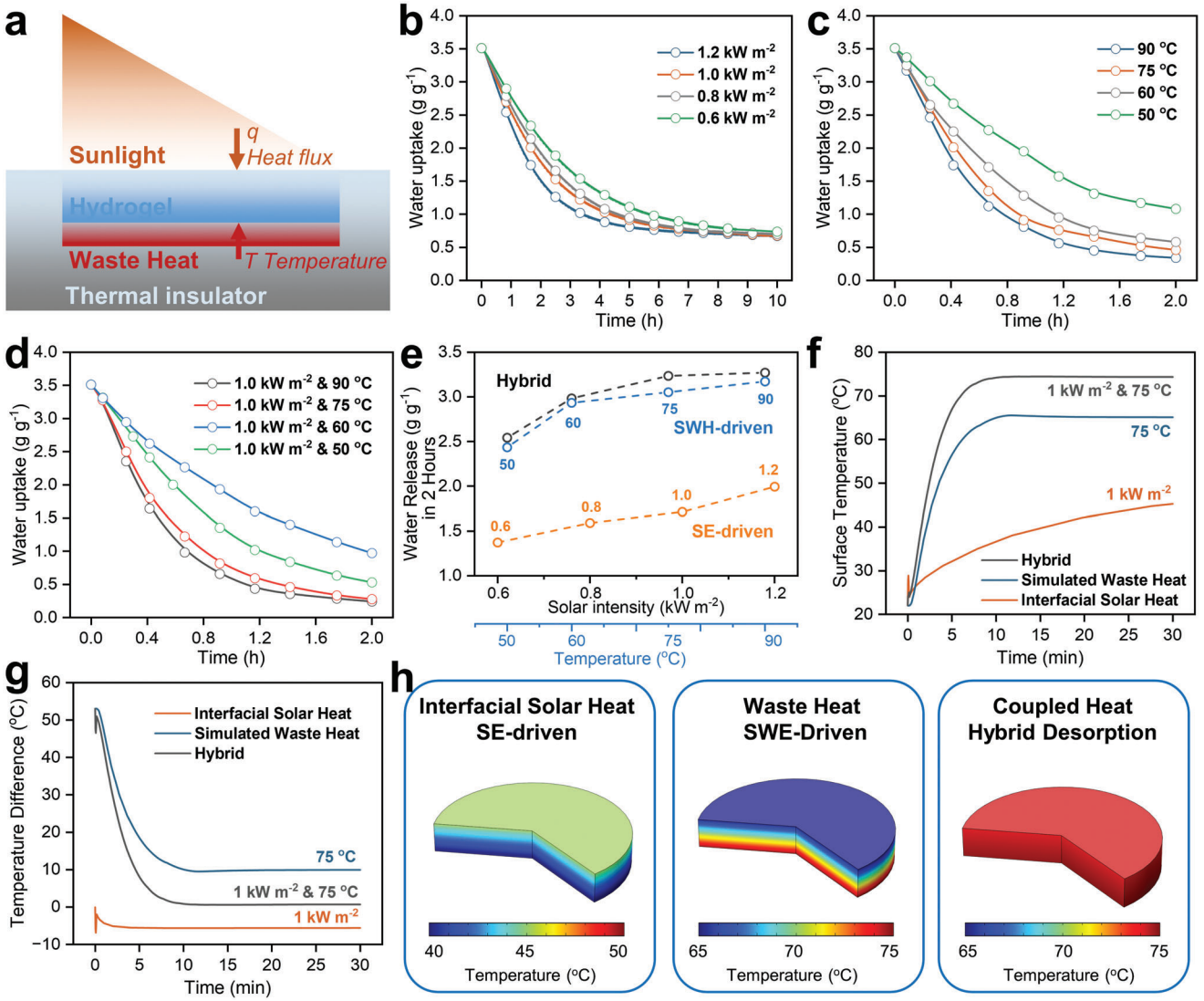

Figure 3. Water vapor desorption performance of PAMPS-CNT-LiCl under coupled energy sources. a) A schematic of the setup for desorption performance evaluation, indicating the locations of the simulated waste heat (SWH) represented by an electrically driven Joule heater and the solar energy (SE) input. b) SE-driven dynamic desorption curves under simulated solar intensities of 0.6, 0.8, 1.0, and 1.2 kW m^{-2}. c) SWH-driven dynamic desorption curves under source temperatures of 50, 60, 75, and 90 °C. d) Hybrid desorption curves under the simulated solar intensity of 1.0 kW m^{-2} and SWH temperatures of 50, 60, 75, and 90 °C. e) The amount of water released during the initial 2 h desorption period was measured for SE-driven, SWH-driven, and hybrid desorption modes. f) Simulation results showing the surface temperature variations of the PAMPS-CNT-LiCl hydrogel in SE-driven, SWH-driven, and hybrid desorption modes. g) Simulation results of the temperature difference variations of the PAMPS-CNT-LiCl hydrogel in SE-driven, SWH-driven, and hybrid desorption modes. h) Temperature profiles of the PAMPS-CNT-LiCl hydrogel in SE-driven, SWH-driven, and hybrid desorption modes after 30 min.

The utilization of waste heat at different temperatures from the bottom as a driving force for desorption (refer as SWH-driven) is found to be significantly more effective than the top interfacial solar heating-driven desorption. The hydrogel sorbent exhibits a remarkable and rapid release of water, with released amounts of 2.43, 2.93, 3.05, and 3.17 g g^{-1} at temperatures of 50, 60, 75, and 90 °C (Figure 3c), respectively, during a short period of 2 h. In contrast, even under the highest solar intensity of 1.2 kW m^{-2}, the water release rate is merely 1.99 g g^{-1} during the same period (Figure 3b), which is inferior to the performance achieved with the application of 50 °C waste heat. In addition to the difference in desorption rates, SWH-driven desorption exhibits a higher degree of desorption, which can be attributed to the difference in the equilibrium temperature of the sorbent, which affects the maximum desorption limit of LiCl.[43]

In the hybrid desorption mode, where solar energy and waste heat are combined, the hydrogel sorbent exhibits a water release of 2.54, 2.98, 3.23, and 3.27 g g^{-1} within 2 h under a heat source temperature of 50, 60, 75, and 90 °C, respectively, with a simultaneous 1 kW m^{-2} simulated solar intensity (Figure 3d). The dynamic desorption curve in the hybrid mode is similar in shape to that of SWH-driven desorption, with a slightly higher water

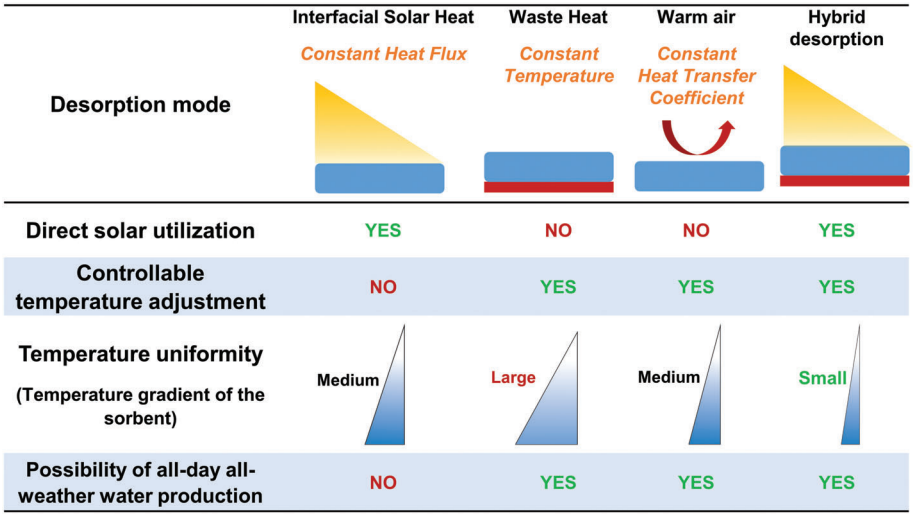

Scheme 2. Feature comparison of the typical desorption modes for SAWH.

release amount, indicating that the waste heat temperature plays a dominant role in desorption kinetics and degree in the hybrid mode (Figure 3e). The amount of water released during the initial 2 h desorption period increases with increasing temperature but becomes less prominent above 75 °C, suggesting that 75 °C is close to the threshold for desorption rate. This could be due to the effects of the tendency of free LiCl to crystallize and release hydrated water completely.[43] Therefore, a SWH temperature of 75 °C was selected for further AWH demonstration.

To investigate the mechanism behind the significant differences in desorption rates and degrees achieved by the three desorption modes mentioned above, we simulate the internal temperature evolution of the hydrogel sorbent during desorption under different energy input configurations via COMSOL software (Note S1 and Figures S26–S28, Supporting Information). The surface temperature variations of the hydrogel sorbent during desorption are shown in Figure 3f. The results show that the SE-driven desorption leads to a very slow increase in surface temperature of the hydrogel, with a low temperature rise of only 45 °C after 30 min, far from reaching equilibrium. In contrast, for the SWE-driven desorption mode, the surface temperature of the hydrogel has already reached the equilibrium temperature of 65 °C in just 13 min. Further exploration of the temperature gradient of the hydrogel along the height direction reveals a bottom-to-surface temperature difference of −5.6 °C for the SE-driven mode and 9.9 °C in 30 min for the SWE-driven mode (Figure 3g,h).

This can be explained, from the perspective of heat and mass transfer, as the solar interface heating provides thermal energy to the hydrogel surface through non-contact radiation, with a fixed and limited heat flux, limited by the solar intensity and photothermal conversion efficiency.[48] In contrast, the bottom waste heat provides a constant temperature boundary to the lower part of the hydrogel, which can be several times the solar heating power and is not limited by photothermal conversion efficiency. Therefore, the constant temperature heating condition at the bottom, as compared to the constant solar flux condition, leads to a rapid temperature equilibrium inside the hydrogel, with a higher concentration gradient of vapor inside, finally leading to a faster water release ability for the SE-driven mode.

For the hybrid heating mode, the hydrogel sorbent is simultaneously heated from the top and bottom sides by coupled energy sources. Under the hybrid desorption mode, the upper surface temperature of the hydrogel reaches a higher temperature of 75 °C in a shorter time (≈10 min) compared to the SWE-driven mode (65 °C, 13 min), which reaches the same to the temperature of the waste heat source (Figure 3f). This demonstrates the heat transfer characteristics are mainly controlled by the constant temperature boundary condition provided by the SWH source.[48] Besides, by using the hybrid desorption mode, a much uniform internal temperature distribution is archived and the temperature difference is less than 1 °C, Figure 3h). Both, the higher average temperature and more uniform temperature distribution in the hydrogel facilitate the water and vapor transports inside the hydrogel, resulting in faster desorption rates and degrees than the previous two modes.[49]

As summarized in **Scheme 2**, our proposed hybrid desorption mode offers several advantages. First, it enables the direct utilization of solar energy and waste heat, thereby achieving water production driven by sustainable energy. Second, the desorption temperature is adjustable according to the energy grade of abundant waste heat with a constant temperature. Third, a much more uniform internal temperature of the sorbent can be achieved, resulting in ultrafast water release. Fourth, all-day, and all-weather water production can be achieved due to the availability of waste heat throughout the day and year. In summary, the hybrid desorption mode provides a possibility for all-day, all-weather, multicyclic, high-yield atmospheric water harvesting through advanced hybrid heat utilization for the desorption process at both the top and bottom surfaces of the sorbent.

2.4. Concept and Optimization of Multicyclic Sorption–Desorption Mode

The monocyclic AWH operation matches the diurnal variation of solar energy, which has been widely introduced to the majority of conceptual solar-driven AWH devices (Figure S29, Supporting Information). However, the mismatch between sorption and

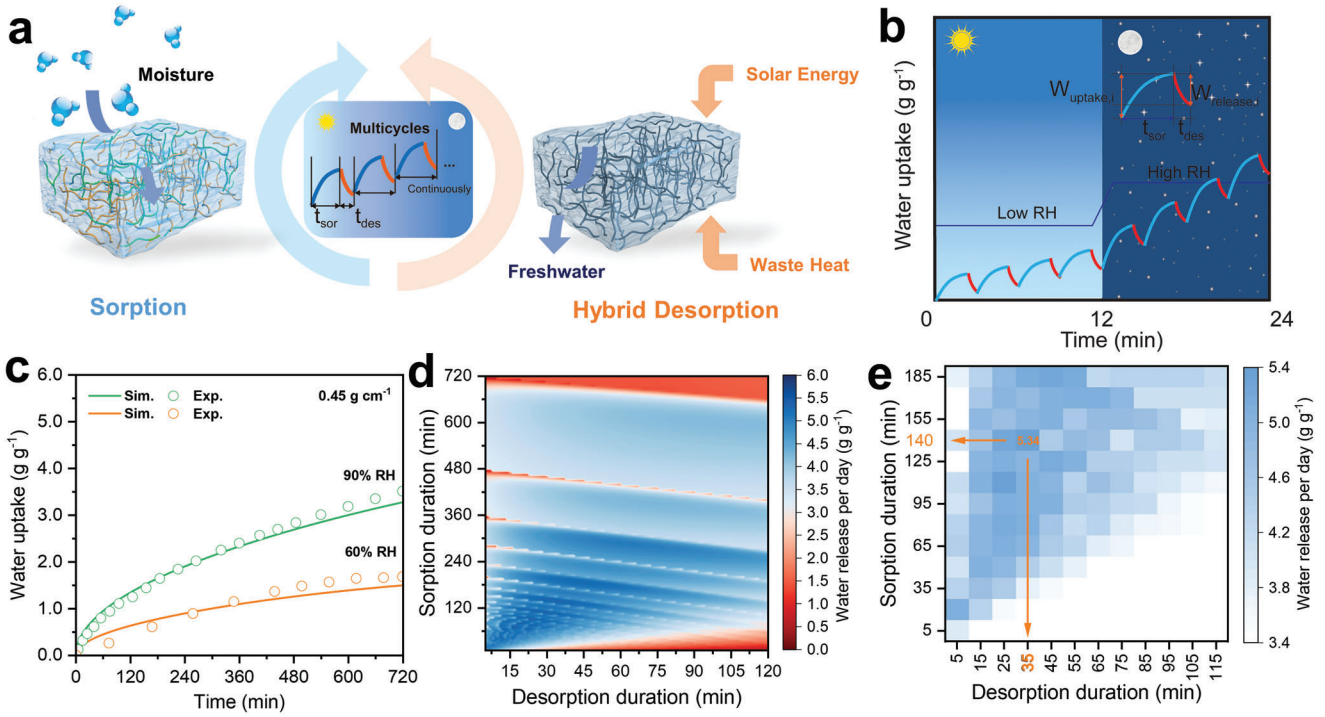

Figure 4. Concept and optimization of multicyclic sorption–desorption mode. a) Schematic of all-day multicyclic AWH mode driven by coupled solar energy and waste heat. b) Schematic of water uptake patterns and sorption–desorption durations in multicyclic AWH modes. c) Simulated and experimental water uptake variations at 60% RH and 90% RH, showing the accuracy of the FD model. d) Graphical mapping denoting a water release per day according to the sorption (20–180 min) and desorption duration (10–60 min), obtained by the optimization program. e) Partially enlarged view of the graphical mapping denotes a water release per day.

desorption rates leads to inefficient utilization of solar energy and daytime time. In addition to the previously proposed batch processing mode,[4] the multicyclic sorption–desorption AWH mode also shows its advantages, as only one piece of sorbent is needed and it can switch between sorption and desorption several times throughout the day. By fully using the potential of the highest sorption and desorption rates at the early stage of sorption and desorption, higher daily water production can be achieved. Additionally, this multicyclic AWH mode can be extended to the nighttime to achieve all-day semicontinuous water production if using solar energy storage systems[50] or waste heat[32] as the supplement energy input (**Figure 4**a).

Although the synthesized hydrogel sorbent has proven the fast water uptake and release performance for the daily multicyclic AWH, the optimization of the sorption and desorption durations (t_{sor} and t_{des}) per cycle remains required,[51] because the frequent switch of sorption and desorption processes would result in the continual energy flow in and out of the sorbent and the consequent ineffective heating and cooling (Figure 4b). Together with the lag of the vapor transport and the condensation, the frequent switches would lead to the waste of energy and mass and increase the complexity of the operation. Hence, we modeled the dynamic sorption–desorption process and established an optimization model to obtain the optimal operation strategy.

Specifically, we simulated the dynamic sorption behavior of the sorbent based on the Fickian diffusion (FD) model[52] (Note S2, Supporting Information). The FD model shows a satisfactory agreement between the theoretical and experimental data derived from both milligram-scale samples (Figure S30, Supporting Information) and bulk samples with a specific weight of 0.45 g cm^{-1} (Figure 4c). The sorption diffusion coefficient of the milligram-scale sample shows higher values than that of the bulk sample. As for desorption, we adopt the dynamic desorption curve under the SWH temperature of 75 °C for nighttime, and under the SWH coupled solar intensity of 1 kW m^{-2} for daytime for the simulation. Based on the dynamic sorption–desorption model, a MATLAB optimization program is built to find out the optimal sorption duration t_{sor}, the desorption duration t_{des}, the number of cycles per day N, and the corresponding water release amount $W_{release}$ (Note S3, Supporting Information). To simplify the calculation, the constant humidity conditions during the daytime or nighttime are selected and the transition of RH is done at the 12th hour instantaneously. We calculated the daily water release under different sorption durations t_{sor} and desorption durations t_{des} (Figure 4d), which shows that the prolonged sorption or desorption duration and fewer cycles can lead to the reduction of overall water release (Figure S31, Supporting Information). To clearly represent the range of the optimal sorption and desorption durations, we amplified the part of the mapping that contains the daily maximum water release ($5 < t_{sor} < 185$ and $5 < t_{des} < 115$, unit: min), as shown in Figure 4e. The results show that the maximum water release occurs at the sorption duration of 140 min, the desorption duration of 35 min, and eight cycles per day. This combination yields a maximum water release of 5.34 g g^{-1} day^{-1}.

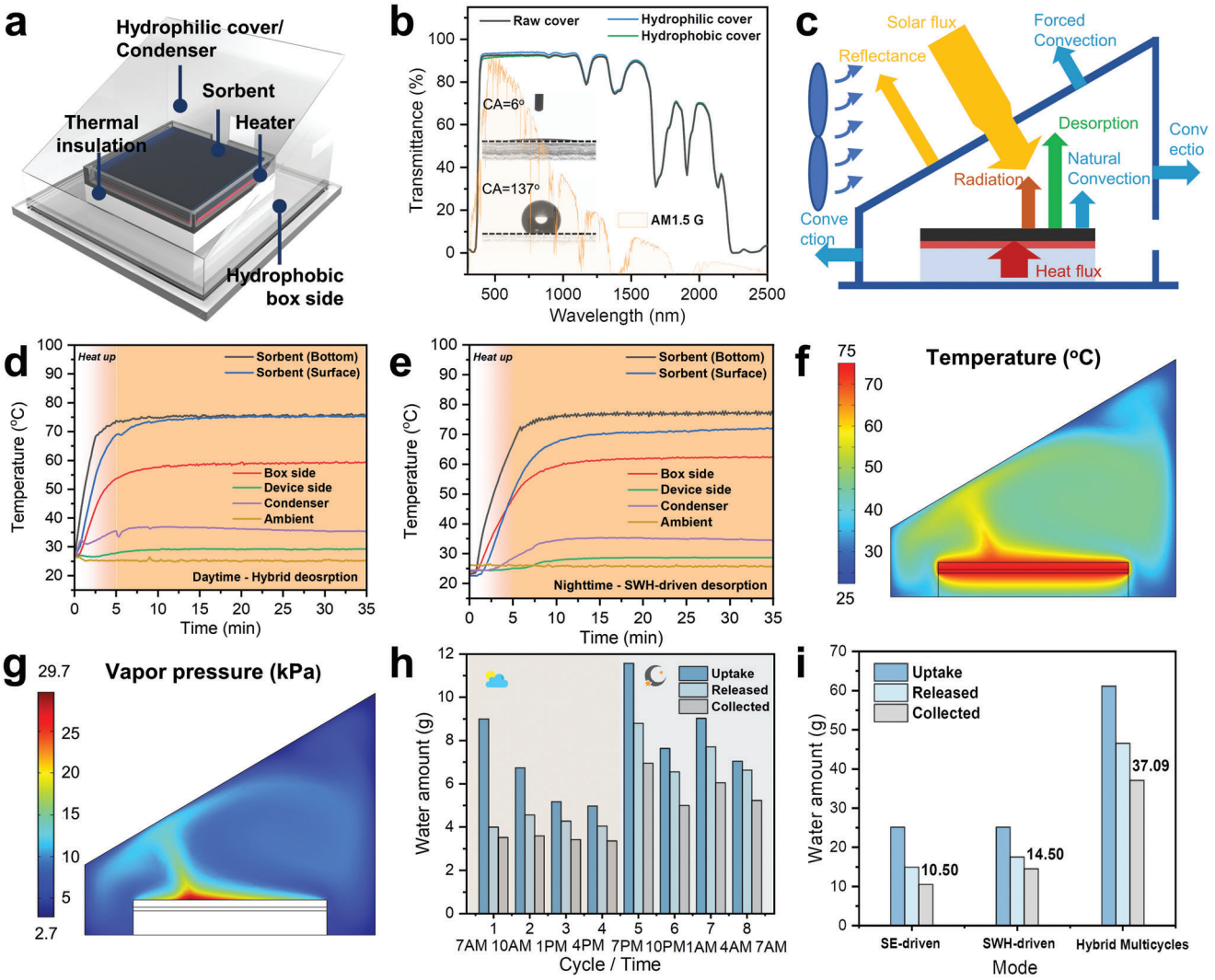

Figure 5. Demonstration of all-day multicyclic atmospheric water harvesting. a) Schematic diagram of the proof-of-concept atmospheric water harvester. b) UV–vis–NIR spectra of the raw, hydrophilically coated, and hydrophobically coated acrylic covers. The insets show the water contact angles of the hydrophilic cover (upper) and the hydrophobic cover (lower). c) Energy flow diagram of the atmospheric water harvester. d) Temperature variations of the components of the water harvester operating during the daytime with hybrid desorption mode. e) Temperature variations of the components of the water harvester that works in the nighttime with SWH-driven desorption. f) Temperature gradient of the water harvester in daytime hybrid desorption mode shows the heat localization of the sorbent. g) Vapor pressure gradient of the water harvester in daytime hybrid desorption mode, showing the significant vapor pressure difference between the sorbent and the condensation cover. h) Water uptake, released water, and collected water during each AWH cycle over the entire day. i) Comparison of daily water production between the proposed all-day multicyclic hybrid desorption AWH mode and the monocyclic AWH mode driven by either SE or SWH.

2.5. Demonstration of All-Day Multicyclic Atmospheric Water Harvesting

We designed a proof-of-concept water harvester to illustrate the multicyclic AWH and the hybrid desorption mode for all-day water production (**Figure 5**a; Figure S32, Supporting Information). The condensation roof cover and side walls made of transparent acrylic material are installed for water collection. To increase the water collection rate, the side walls were treated with a commercial hydrophobic coating to accelerate the flow of water droplets (Figure 5b), meanwhile, the top cover was treated with a superhydrophilic coating to prevent the reflection and dispersion of sunlight due to the accumulated water droplets after condensation. The transmittance of solar sunlight through acrylic material is less influenced by neither hydrophilic nor hydrophilic coatings (Figure 5b; Figure S33, Supporting Information). An air fan was employed to create an external forced convection condition to accelerate the water vapor condensation, appearing as an apparent temperature decrease of 22.4 °C compared to the natural air flow (Figure S34, Supporting Information). The hydrogel sorbent PAMPS-CNT-LiCl was placed on a heater for waste heat supply at a constant temperature, and its bottom was treated with thermal insulation foam. As suggested by the multicycle optimization model, the hydrogel was first exposed to the simulated daytime RH environment for four cycles with 140 min sorption, 35 min hybrid desorption, followed by a 5 min time interval for water

collection and device assembly (Figure 5b; Figure S35, Supporting Information). Then, the environmental conditions were shifted to the nighttime high-RH condition for the following four cycles, during which the desorption was driven by the SWH only. The morphology and performance of the hydrogel sorbent remain stable after multiple experiments (Figure S36, Supporting Information). Besides, the switching and sealing processes were performed manually in the lab for conceptual demonstration but could be easily achieved by a mechanical component powered by solar panels. Detail experiment procedures can be found in Experimental Section.

The energy flow of the atmospheric water harvester was analyzed to determine its heat transfer efficiency (Figure 5c). We investigated the temperature variation during the different desorption modes. Closely similar to the open-environment desorption (Figure 3a), the hydrogel sorbent was heated more rapidly with lesser temperature difference for the hybrid desorption during the daytime (Figure 5d) compared to the SWH-driven desorption pattern during the nighttime (Figure 5e). The temperature at the bottom of the sorbent was maintained at 75 °C ± 1.5 °C, which could sufficiently drive the rapid desorption (Figure 2g), while the maximum condensation temperature was 36.9 °C, which occurred at ≈10 min due to the high desorption rate in the early water release stage (Figure 2c). The COMSOL simulation results show the internal temperature distribution of the water harvester in the nighttime hybrid desorption mode (Figure 5f; Note S4, Supporting Information), indicating the heat localization near the sorbent. A huge temperature difference between the sorbent and the condensation cover was generated, affecting further the vapor pressure difference. This has also been confirmed by the vapor pressure distribution (Figure 5g). The surface of the sorbent had a vapor pressure of 29.7 kPa, corresponding to the saturated vapor pressure at the temperature of 69 °C, while the vapor pressure on the condensation cover was only 5.4 kPa (35 °C, 100% RH). The corresponding RH distribution inside the water harvester calculated by the vapor pressure is shown in Figure S37 (Supporting Information). This vapor pressure difference can drive the efficient flow and condensation of water vapor, ensuring overall water production in an efficient manner.

Figure 5h shows the experimental results of the captured, released, and collected water during the eight sorption–desorption cycles. The water uptake at the initial cycle of the daytime or nighttime environment (1st and 4th cycle) reaches its maximum value compared with the following sorption at the daytime or nighttime stages, respectively. This is because the water release is not sufficient in each cycle, and the next water uptake is established on the residual water content, therefore, the following sorption rate decreases, which can be visually observed from the sorption kinetic curve (Figure S38, Supporting Information). The average desorption efficiency (i.e., the ratio of water release to water uptake) and condensation efficiency (i.e., the ratio of condensed water to water release) are 72.3% and 80.4%, respectively, indicating the effectiveness of water release and condensation of the AWH device. Finally, the overall water production enabled by the optimized multicyclic operation strategy and hybrid desorption mode is 37.09 g day^{-1} (Figure S39, Supporting Information), corresponding to the average water collection of 2410 mL_{water} $kg_{sorbent}^{-1}$ day^{-1} and 5795 mL_{water} $m_{sorbent}^{-2}$ day^{-1} in a diurnal cycle, showing the high-yield water production of 180 g_{water} $m_{sorbent}^{-2}$ h^{-1} in the daytime and 302 g_{water} $m_{sorbent}^{-2}$ h^{-1} in the nighttime. From the perspective of the entire water harvester, our system, combined with the operation strategy, can produce 1101 g of water per kilogram of device per day (1101 g kg_{device}^{-1} day^{-1}) and 46 g of water per liter of device per day (46 g L_{device}^{-1} L^{-1}). Finally, the proposed all-day multicyclic operation strategy and hybrid desorption mode show water production boost of 353% and 255% compared to the monocyclic operation driven by solar energy (10.50 g day^{-1}) or waste heat (14.50 g day^{-1}), respectively (Figure 5i; Note S5, Supporting Information).

3. Conclusion

We achieved all-day atmospheric water harvesting and improved the daily water production yield from the aspects of material and strategy designs. The cationic polyelectrolyte hydrogel sorbent PAMPS-CNT-LiCl facilitates the large interior pressure and the satisfactory swelling ratio for fast water sorption kinetics and water storage. Owing to the unique chemical composition, it also enables the LiCl ions to coordinate with charged polymeric chains for stable salt retention. The sorbent PAMPS-CNT-LiCl achieves water uptake of 0.65, 1.00, and 1.87 g g^{-1} at the RH of 15%, 30%, and 60% RH, respectively, without the risk of solution leakage. More importantly, the hybrid desorption mode that couples solar energy and simulated waste heat for driving water release enables a distinctive temperature pattern with a much uniform sorbent temperature for achieving the ultrafast water release. Moreover, the waste heat utilization allows water release to be extended into the night, thus realizing all-day fast multicyclic water harvesting. Furthermore, an optimization model related to dynamic sorption–desorption characteristics is built to obtain the optimized sorption–desorption durations and the number of daily cycles. Finally, a lab-tested water harvester achieved high-yield water production of up to 2410 mL_{water}^{-1} $kg_{sorbent}^{-1}$ day^{-1}, which is 3.5 and 2.5 times compared to the single-cyclic solar-driven photothermal mode and waste heat-driven mode, respectively.

4. Experimental Section

Chemicals and Synthesis of PAMPS-CNT-LiCl: 2-Acrylamido-2-methyl-1-propanesulfonic acid (AMPS, 99%), *N*,*N*′-methylenebis(acrylamide) (MBAA, 99%), ammonium persulfate (APS, 98%) were purchased from Sigma–Aldrich. Deionized (DI) water (18.2 MΩ, from the Milli-Q system) was used throughout the experiments. Carbon nanotubes (CNT, 5–15 nm × 10–30 µm) were purchased from XFNANO. All materials were used without further purification.

AMPS powder (1285.7 mg) and 1 mg mL^{-1} CNT solution (3 g) were mixed under stirring conditions and purged with nitrogen for 10 min. Then, the cross-linker MBAA in varying percentages (0.5, 1, 3, 5, 10, 25, and 50 wt%) was added and dissolved. Next, the initiator APS (molar ratio to monomers = 50:1) was added to the solution separately and followed by the 3 min sonication. Then, the polymerization should be carried out for about 12 h at 60 °C. The obtained hydrogel was immersed in DI water for 24 h to remove unreacted chemicals to obtain the pure PAMPS-CNT hydrogel. To obtain PAMPS-CNT-LiCl hydrogel sorbent, PAMPS-CNT hydrogels were immersed into LiCl solutions with different concentrations (5, 15, 25, 35, and 45 wt%) to embed LiCl into the polymeric networks. After becoming fully swelled, PAMPS-CNT-LiCl hydrogel sorbents with different mass ratios of LiCl to PAMPS-CNT were obtained by drying them at 80 °C. The PAMPS hydrogel and PAMPS-LiCl hydrogel sorbents were obtained by replacing the CNT solution with DI water. The CNT solution was

obtained by refluxing the as-purchased CNT (5 g) in a mixture of 70% nitric acid (50 mL) and 97% sulfuric acid (150 mL) for 5 h at 70 °C, followed by washing and sonication to disperse in DI water.

Characterization of PAMPS-CNT-LiCl: The storage modulus and the loss modulus of hydrogels were measured by an automatic rheometer (MCR302, Anton Paar). The microstructures and element distribution of hydrogels were characterized collectively by SEM (Zeiss Supra 40VP). The chemical composition and the salt state of the hydrogel sorbents were confirmed by Fourier-transform infrared spectroscopy (FTIR) and X-ray photoelectron spectroscopy (XPS), which were respectively conducted by Agilent Cary 660 spectrometer and Kratos Axis Ultra DLD spectrometer. Thermogravimetric analysis (TGA) was carried out on a thermal instrument (TGA Q500) by increasing the temperature from ambient temperature to 600 °C at a rate of 10 °C min^{-1}. A UV–vis–NIR spectrometer (Agilent Cary 7000) equipped with an integrating sphere was employed for light absorption curve measurements. X-ray diffraction (XRD) patterns were collected by an X-ray Diffractometer (Bruker D8 Advance) with a scanning rate of 10° min^{-1}. The mechanical properties of hydrogels were tested by a dynamic mechanical analyzer (Instron 4505 tensile machine). The contact angle measurements were performed on a VCA optima surface analysis system (AST Products Inc., Billerica, MA, USA) using the sessile drop method with a 3 µL deionized water droplet. Nitrogen gas adsorption isotherms were recorded on volumetric gas adsorption analyzer at 77 K by 3Flex America Micromeritics.

Osmotic Pressure Measurements of Hydrogel Sorbent: Instead of directly calculating the osmotic pressure of PAMPS-CNT hydrogel, it was obtained by immersing it in LiCl solution with different concentrations (i.e., different osmotic pressures). When the hydrogel could not swell in the LiCl solution with a certain osmotic pressure, i.e., the LiCl solution reached the thermodynamic equilibrium with the hydrogel, the osmotic pressure of external LiCl solution was considered as the osmotic pressure of hydrogel. The osmotic pressure P_{osm} of strong inorganic electrolytes with a certain molar concentration C can be calculated with the assumption of complete hydrolysis according to van't Hoff's theory:

$$P_{osm} = iCRT \quad (1)$$

where i is the dimensionless van't Hoff index, $i = 2$ for LiCl solution; R is the ideal gas constant (8.314 J K^{-1} mol^{-1}); and T is the temperature (298.15 K). The experimental results showed that the hydrogel cannot swell in the LiCl solution with a concentration of 45 wt% and the calculated osmotic pressure of 659 atm. Therefore, the osmotic pressure of PAMPS-CNT was considered as 659 atm.

Water Sorption Tests of Milligram-Scale Sorbent: Water sorption isotherms and sorption kinetics of the milligram-scale sorbent at different temperatures and RHs were measured using a sorption analyzer (Aquadyne DVS). Before the isotherm measurement, PAMPS-CNT-LiCl was completely dried at 80 °C, then transferred in the analyzer and kept at temperature (25 and 60 °C) with RH variations. The sorption–desorption kinetics were measured by transferring the dried sample to the analyzer with a constant temperature of 25 °C and the RHs of 15%, 30%, 60%, and 90% for 600 min, then the temperature and RH were changed to 90 °C and 4%, respectively, for desorption. The flow rate of the dry air was 120 mL min^{-1}.

Water Sorption Tests of Bulk Sorbent: Sorption kinetics of the bulk sorbent sample at different temperatures and RHs were measured using a constant climate chamber (KMF-115E, Binder, Figure S15, Supporting Information) with the temperature and RH accuracy of ±0.1 °C and ±1.5% RH. All samples were dried at 80 °C for 4 h to be dehydrated before the sorption tests. Once the chamber reached the set temperature (25 °CC) and humidity (30%, 60%, and 90% RH), the dry samples with the specific weights of 0.05, 0.18, and 0.45 g cm^{-2} were transferred into the chamber for 12 h. Then, the temperatures and RHs were changed to 65, 70, and 90 °C with a vapor pressure of 4.25 kPa. The mass change was measured by an analytical balance (Sartorius CP224S) connected to the PC.

Water Desorption Tests of Bulk Sorbent: The SE-driven water desorption experiments were carried out under a xenon-lamp equipped with an AM1.5G filter (PLS-SXE300e/300UV) to simulate the solar intensities of 0.6, 0.8, 1.0, and 1.2 kW m^{-2}. The SWH-driven water desorption experiments were carried out by placing the sample on a heater (JiuKou, China) with a temperature feedback system to provide a constant temperature of 50, 60, 75, and 90 °C. The temperatures of the sample and the heater were measured by the ultrathin thermocouples (Kapson, K-type, −200 to 200 °C ± 0.1 °C). For hybrid desorption, the xenon-lamp and the heater were both in operation for heating the sorbent and desorption. The mass change was measured by an analytical balance (Sartorius CP224S) connected to PC. Before the tests, the samples sorbed the water vapor at 25 °C and 90% RH for 12 h with a water content of ≈3.51 g g^{-1}.

Fabrication and Tests of the Atmospheric Water Harvester: The atmospheric water harvester was composed of a water collection framework and a container, which were all made of acrylic sheets. The water collection framework was composed of an inclined condensation cover, four side walls, and a base plate. The base plate and the covers were quickly assembled and disassembled through the tenon-and-mortise structure. The angle between the condensation cover and the horizontal plane was 30° to accelerate the water flow. The condensation cover was coated with a commercial hydrophilic painting to achieve film water condensation, and the side walls were coated with a commercial hydrophobic painting to form water droplets and accelerate the vertical water flow. The container was made of heat with PID feedback system and a thermal insulation foam with a surface area of 8 × 8 cm^2, and the sorbent was placed on the heater and adhered to by adhesive tape. The weight of PAMPS-CNT-LiCl samples for water collection measurement was ≈14–16 g. The water harvesting experiments were carried out under laboratory conditions with an average RH of 65% and an average temperature of 22 °C under artificial lighting generated by a solar simulator with an irradiation intensity of 0.95–1.05 kW m^{-2}, and the heater was powered by a DC power source. The external air flow was ≈1–2 m s^{-1} for enhanced heat dissipation from the device. The dry hydrogel sorbent was put on the container and placed inside the climate chamber for the first sorption duration of 140 min. Then, the container with the sorbent was transferred to the water collection framework for the first desorption duration of 35 min. After desorption and condensation, the cover for vapor condensation was opened to allow the external moisture to flow in for the next water harvesting cycle. To prevent the solar heating effect that disrupts the sorption process, aluminum foil was manually placed 5 cm over the hydrogel sorbent. This process took 5 min to complete. After four daytime low-RH cycles, the humidity of the chamber used for sorption was changed to high RH condition to simulate the nighttime. The K-type thermocouples were connected to the thermostat, the surface and the bottom of the sorbent, the side wall of the water harvester, the condensation cover, and the side wall of the container to monitor and control the temperature. The temperature signals were collected by a portable data acquisition instrument. The amount of the collected water was obtained by weighing the liquid water that was gathered by the pipette using a balance. The masses of sorbed and desorbed water were obtained by measuring the mass change of sorbent before and after the water release for each cycle.

Supporting Information

Supporting Information is available from the Wiley Online Library or from the author.

Acknowledgements

The authors acknowledge the financial support from the Foundation for Innovative Research Groups of the National Natural Science Foundation of China (No. 51521004), the National Natural Science Foundation of China (No. 52006143), and the Fundamental Research Funds for the Central Universities. The authors also acknowledge the financial support from the Ministry of Education Academic Research Fund Tier 2 (A-0005415-01-00). P.P. thanks the Research Fund for International Young Scientists of the National Natural Science Foundation of China (No. 52150410421). H.S. thanks the support from China Scholarship Council (CSC) (No. 202106230250).

Conflict of Interest

The authors declare no conflict of interest.

Author Contributions

R.W. and S.C.T. supervised the project. H.S. convinced, designed, and carried out the experiment. H.S. and Z.Y. established the model for water sorption kinetics. H.S. and P.P. designed the optimization algorithms and established the optimization procedures. Z.Y. carried out the simulation for the water harvester. H.Q., H.S., and Y.Z. engineered the atmospheric water harvester. H.S., P.P., and M.Z. wrote the manuscript. All the authors discussed the results and contributed to the manuscript.

Data Availability Statement

The data that support the findings of this study are available from the corresponding author upon reasonable request.

Keywords

atmospheric water harvesting, hygroscopic materials, polyelectrolyte hydrogels, thermodynamics, waste heat

Received: March 3, 2023
Revised: April 17, 2023
Published online: July 17, 2023

[1] M. M. Mekonnen, A. Y. Hoekstra, *Sci. Adv.* **2016**, *2*, e1500323.
[2] Y. Tu, R. Wang, Y. Zhang, J. Wang, *Joule* **2018**, *2*, 1452.
[3] a) H. Kim, S. Yang, S. R. Rao, S. Narayanan, E. A. Kapustin, H. Furukawa, A. S. Umans, O. M. Yaghi, E. N. Wang, *Science* **2017**, *356*, 430; b) J. Lord, A. Thomas, N. Treat, M. Forkin, R. Bain, P. Dulac, C. H. Behroozi, T. Mamutov, J. Fongheiser, N. Kobilansky, S. Washburn, C. Truesdell, C. Lee, P. H. Schmaelzle, *Nature* **2021**, *598*, 611.
[4] a) H. Shan, C. Li, Z. Chen, W. Ying, P. Poredoš, Z. Ye, Q. Pan, J. Wang, R. Wang, *Nat. Commun.* **2022**, *13*, 5406; b) D. K. Nandakumar, S. K. Ravi, Y. Zhang, N. Guo, C. Zhang, S. C. Tan, *Energy Environ. Sci.* **2018**, *11*, 2179; c) L. Yang, D. K. Nandakumar, W. Lu, M. Gao, X. L. C. Wee, K. Zeng, M. Bosman, S. C. Tan, *Adv. Mater.* **2020**, *32*, 2000971.
[5] a) D. K. Nandakumar, Y. Zhang, S. K. Ravi, N. Guo, C. Zhang, S. C. Tan, *Adv. Mater.* **2019**, *31*, 1806730; b) J. Yang, X. Zhang, H. Qu, Z. G. Yu, Y. Zhang, T. J. Eey, Y. -W. Zhang, S. C. Tan, *Adv. Mater.* **2020**, *32*, 2002936; c) J. Xu, T. Li, T. Yan, S. Wu, M. Wu, J. Chao, X. Huo, P. Wang, R. Wang, *Energy Environ. Sci.* **2021**, *14*, 5979.
[6] a) F. Fathieh, M. J. Kalmutzki, E. A. Kapustin, P. J. Waller, J. Yang, O. M. Yaghi, *Sci. Adv.* **2018**, *4*, eaat3198; b) Y. Feng, T. Ge, B. Chen, G. Zhan, R. Wang, *Cell Rep. Phys. Sci.* **2021**, *2*, 100561.
[7] S. M. Towsif Abtab, D. Alezi, P. M. Bhatt, A. Shkurenko, Y. Belmabkhout, H. Aggarwal, Ł. J. Weseliński, N. Alsadun, U. Samin, M. N. Hedhili, M. Eddaoudi, *Chem* **2018**, *4*, 94.
[8] T. Yang, L. Ge, T. Ge, G. Zhan, R. Wang, *Adv. Funct. Mater.* **2022**, *32*, 2105267.
[9] A. C. Li, L. Zhang, Y. Zhong, X. Li, B. E. Fil, P. F. Fulvio, K. S. Walton, E. N. Wang, *Appl. Phys. Lett.* **2022**, *121*, 164102.
[10] H. Shan, Q. Pan, C. Xiang, P. Poredoš, Q. Ma, Z. Ye, G. Hou, R. Wang, *Cell Rep. Phys. Sci.* **2021**, *2*, 100664.
[11] R. Li, Y. Shi, M. Alsaedi, M. Wu, L. Shi, P. Wang, *Environ. Sci. Technol.* **2018**, *52*, 11367.
[12] J. Xu, T. Li, J. Chao, S. Wu, T. Yan, W. Li, B. Cao, R. Wang, *Angew. Chem., Int. Ed.* **2020**, *59*, 5202.
[13] Y. Zhang, L. Wu, X. Wang, J. Yu, B. Ding, *Nat. Commun.* **2020**, *11*, 3302.
[14] F. Deng, C. Xiang, C. Wang, R. Wang, *J. Mater. Chem. A* **2022**, *10*, 6576.
[15] a) Z. Deng, L. Miao, P.-F. Liu, J. Zhou, P. Wang, Y. Gu, X. Wang, H. Cai, L. Sun, S. Tanemura, *Nano Energy* **2019**, *55*, 368; b) X. Mu, J. Zhou, P. Wang, H. Chen, T. Yang, S. Chen, L. Miao, T. Mori, *Energy Environ. Sci.* **2022**, *15*, 3388.
[16] a) W. Shi, W. Guan, C. Lei, G. Yu, *Angew. Chem., Int. Ed.* **2022**, *61*, e202211267; b) H. Lu, W. Shi, Y. Guo, W. Guan, C. Lei, G. Yu, *Adv. Mater.* **2022**, *34*, 2110079; c) Z. Sun, X. Wen, L. Wang, J. Yu, X. Qin, *Energy Environ. Sci.* **2022**, *15*, 4584; d) J. Yang, X. Zhang, J. J. Koh, R. Deng, S. Kumarasamy, Y. X. Xu, H. Qu, S. Zhang, S. C. Tan, *Small* **2022**, *18*, 2107636.
[17] Y. Guo, J. Bae, Z. Fang, P. Li, F. Zhao, G. Yu, *Chem. Rev.* **2020**, *120*, 7642.
[18] F. Zhao, X. Zhou, Y. Liu, Y. Shi, Y. Dai, G. Yu, *Adv. Mater.* **2019**, *31*, 1806446.
[19] Y. Guo, W. Guan, C. Lei, H. Lu, W. Shi, G. Yu, *Nat. Commun.* **2022**, *13*, 2761.
[20] C. Lei, Y. Guo, W. Guan, H. Lu, W. Shi, G. Yu, *Angew. Chem., Int. Ed.* **2022**, *61*, e202200271.
[21] a) X. Liu, Z. Tong, O. Hu, *Macromolecules* **1995**, *28*, 3813; b) Y. Zhao, H. Su, L. Fang, T. Tan, *Polymer* **2005**, *46*, 5368; c) A. E. English, T. Tanaka, E. R. Edelman, *J. Chem. Phys.* **1997**, *107*, 1645.
[22] S. Pu, J. Fu, Y. Liao, L. Ge, Y. Zhou, S. Zhang, S. Zhao, X. Liu, X. Hu, K. Liu, J. Chen, *Adv. Mater.* **2020**, *32*, 1907307.
[23] M. Dai, F. Zhao, J. Fan, Q. Li, Y. Yang, Z. Fan, S. Ling, H. Yu, S. Liu, J. Li, W. Chen, G. Yu, *Adv. Mater.* **2022**, *34*, 2200865.
[24] a) S. Pu, J. Fu, Y. Liao, L. Ge, Y. Zhou, S. Zhang, S. Zhao, X. Liu, X. Hu, K. Liu, *Adv. Mater.* **2020**, *32*, 1907307; b) Y. Wang, S. Gao, H. Zhong, B. Zhang, M. Cui, M. Jiang, S. Wang, Z. Wang, *Cell Rep. Phys. Sci.* **2022**.
[25] C. Forman, I. K. Muritala, R. Pardemann, B. Meyer, *Renewable Sustainable Energy Rev.* **2016**, *57*, 1568.
[26] X. Li, D. Lou, H. Wang, X. Sun, J. Li, Y.-N. Liu, *Adv. Funct. Mater.* **2020**, *30*, 2007291.
[27] Y. Osada, *Advances in Polymer Science*, vol *82*. Springer, Berlin/Heidelberg, Germany **1987**.
[28] a) J. Zeng, Q. Wang, Y. Shi, P. Liu, R. Chen, *Adv. Energy Mater.* **2019**, *9*, 1900552; b) H. Wang, J. Wei, G. P. Simon, *Environ. Sci. Technol.* **2014**, *48*, 4214.
[29] a) L. Ni, J. Meng, G. M. Geise, Y. Zhang, J. Zhou, *J. Membr. Sci.* **2015**, *491*, 73; b) H. C. Yu, S. Y. Zheng, L. Fang, Z. Ying, M. Du, J. Wang, K. F. Ren, Z. L. Wu, Q. Zheng, *Adv. Mater.* **2020**, *32*, 2005171; c) N. Ueno, T. Wakabayashi, H. Sato, Y. Morisawa, *J. Phys. Chem. A* **2019**, *123*, 10746.
[30] a) N. Hanikel, M. S. Prevot, F. Fathieh, E. A. Kapustin, H. Lyu, H. Wang, N. J. Diercks, T. G. Glover, O. M. Yaghi, *ACS Cent. Sci.* **2019**, *5*, 1699; b) R. Li, Y. Shi, M. Wu, S. Hong, P. Wang, *Nano Energy* **2020**, *67*, 104255.
[31] P. Poredoš, H. Shan, R. Wang, *Joule* **2022**, *6*, 1390.
[32] Z. Y. Xu, J. T. Gao, B. Hu, R. Z. Wang, *Energy* **2022**, *238*, 121804.
[33] P. J. Flory, *Principles of Polymer Chemistry*, Cornell University Press, Ithaca, NY, USA **1953**.
[34] E. Su, M. Yurtsever, O. Okay, *Macromolecules* **2019**, *52*, 3257.
[35] M. Mihajlovic, M. Mihajlovic, P. Y. W. Dankers, R. Masereeuw, R. P. Sijbesma, *Macromol. Biosci.* **2019**, *19*, 1800173.
[36] Z. Wu, W. Shi, H. Ding, B. Zhong, W. Huang, Y. Zhou, X. Gui, X. Xie, J. Wu, *J. Mater. Chem. C* **2021**, *9*, 13668.
[37] W. Zhao, H. Gong, Y. Song, B. Li, N. Xu, X. Min, G. Liu, B. Zhu, L. Zhou, X.-X. Zhang, J. Zhu, *Adv. Funct. Mater.* **2021**, *31*, 2100025.
[38] M. B. Singh, V. H. Dalvi, V. G. Gaikar, *RSC Adv.* **2015**, *5*, 15328.

[39] C.-J. Lee, H. Wu, Y. Hu, M. Young, H. Wang, D. Lynch, F. Xu, H. Cong, G. Cheng, *ACS Appl. Mater. Interfaces* **2018**, *10*, 5845.
[40] X. Shen, L. Peng, R. Li, H. Li, X. Wang, B. Huang, D. Wu, P. Zhang, J. Zhao, *ChemElectroChem* **2019**, *6*, 4483.
[41] a) A. M. Atta, H. S. Ismail, A. M. Elsaaed, *J. Appl. Polym. Sci.* **2012**, *123*, 2500; b) X. Li, L. Cao, L.-p. Chen, *Biochem. Eng. J.* **2022**, *187*, 108606.
[42] a) J. Ma, Y. Zhang, Y. Tang, Y. Wei, Y. Liu, C. Liu, *Water Sci Technol* **2018**, *78*, 982; b) B. A. Getachew, S.-R. Kim, J.-H. Kim, *Environ. Sci. Technol.* **2017**, *51*, 905.
[43] M. R. Conde, *Int. J. Therm. Sci.* **2004**, *43*, 367.
[44] P. Poredoš, H. Shan, C. Wang, F. Deng, R. Wang, *Energy Environ. Sci.* **2022**, *15*, 3223.
[45] W. Wang, Q. Pan, Z. Xing, X. Liu, Y. Dai, R. Wang, T. Ge, *Water Res.* **2022**, *211*, 118029.
[46] a) Y. Zhang, S. C. Tan, *Nat. Sustainability* **2022**, *5*, 554; b) Z. Chen, Z. Shao, Y. Tang, F. Deng, S. Du, R. Wang, *ACS Mater. Au* **2022**.
[47] a) S. Bouazizi, S. Nasr, *J. Mol. Liq.* **2014**, *197*, 77; b) I. Pethes, *J. Mol. Liq.* **2018**, *264*, 179.
[48] C. D. Díaz-Marín, L. Zhang, B. E. Fil, Z. Lu, M. Alshrah, J. C. Grossman, E. N. Wang, *Int. J. Heat Mass Transfer* **2022**, *195*, 123103.
[49] C. D. Díaz-Marín, L. Zhang, Z. Lu, M. Alshrah, J. C. Grossman, E. N. Wang, *Nano Lett.* **2022**, *22*, 1100.
[50] T. Yan, T. Li, J. Xu, J. Chao, R. Wang, Y. I. Aristov, L. G. Gordeeva, P. Dutta, S. S. Murthy, *ACS Energy Lett.* **2021**, *6*, 1795.
[51] H. Park, I. Haechler, G. Schnoering, M. D. Ponte, T. M. Schutzius, D. Poulikakos, *ACS Appl. Mater. Interfaces* **2022**, *14*, 2237.
[52] U. Legrand, P.-L. Girard-Lauriault, J.-L. Meunier, R. Boudreault, J. R. Tavares, *Langmuir* **2022**, *38*, 2651.

Device

Article

Improving solar water harvesting via airflow restructuring using 3D vapor generator

Graphical abstract

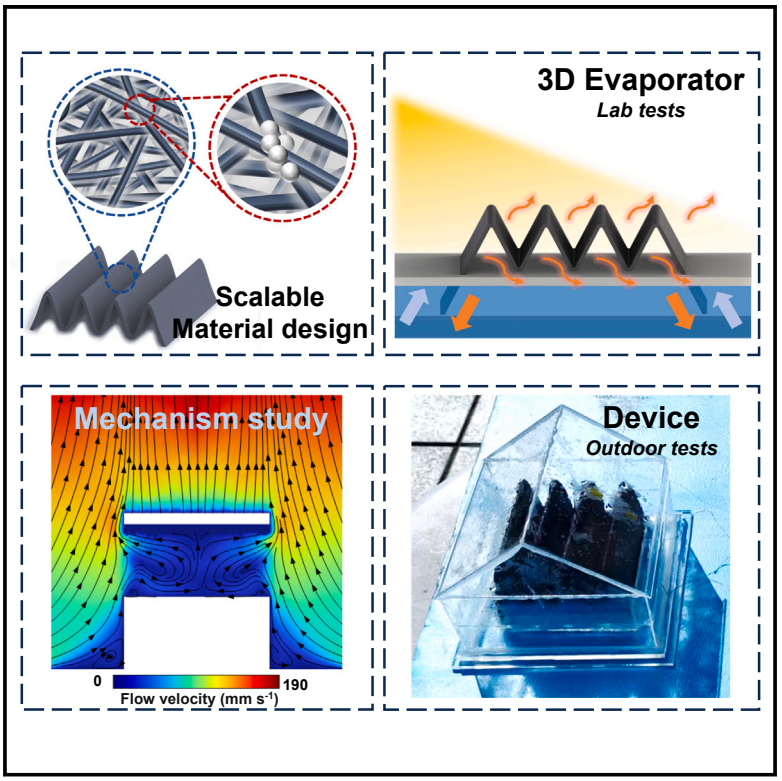

Highlights

- Developed low-cost 3D solar vapor generators to achieve high-performance evaporation
- Investigated mechanisms for the improved evaporation performance of the 3D structure
- Accounted for the impact of sun trajectory on solar energy capture
- A comprehensive analysis of the heat and mass transfer process in the 3D structure

Authors

Correspondence

In brief

A scalable 3D evaporation structure can enhance the performance of solar evaporators and contribute to the future design of atmospheric water harvesters. Through the analysis of thermodynamic parameters of the airflow around the evaporator, we observed that the enhancement does not solely rely on the augmentation of dark evaporation but that it also benefits from the 3D dual-sided evaporation configuration, leading to enhanced vapor diffusion and a more uniform temperature distribution.

Develop
Prototype with demonstrated applications in relevant environment

Shan et al., 2023, Device *1*, 100065
October 20, 2023 https://doi.org/10.1016/j.device.2023.

CellPress

Please cite this article in press as: et al., Improving solar water harvesting via airflow restructuring using 3D vapor generator, Device (2023), https://doi.org/10.1016/j.device.2023.100065

Device

CellPress

Article

Improving solar water harvesting via airflow restructuring using 3D vapor generator

[1]Institute of Refrigeration and Cryogenics, Shanghai Jiao Tong University, 800 Dongchuan Road, Shanghai 200240, China
[2]Engineering Research Center of Solar Power & Refrigeration, MOE China, Shanghai 200240, China
[3]Lead contact
*Correspondence:
https://doi.org/10.1016/j.device.2023.100065

THE BIGGER PICTURE The water crisis profoundly impacts the well-being and sustainable development of the global population. Exploring unconventional water resources has emerged as a viable solution to alleviate freshwater scarcity, where solar evaporation provides a zero-energy and environmentally friendly approach. While this technology has demonstrated promising results, there remains a performance and scalability gap between in-lab testing and their use in real-world conditions. We designed a 3D structured evaporator and present a comprehensive analysis of the heat and mass transfer mechanisms. The evaporation enhancement is attributed to the restructured evaporator airflow and improved outdoor solar energy capture. This comprehension leads to the advancement of future solar vapor generators and/or atmospheric water harvesters without increasing material costs. We hope our analysis contributes to the maturation and pragmatic implementation of this water purification technology.

SUMMARY

Solar interfacial evaporation offers a promising solution to the global water crisis. 3D vapor generators (3DVGs) have shown advancements in evaporation rates and efficiency, yet the mechanisms behind this enhancement remain enigmatic. To elucidate these mechanisms, we develop a scalable origami-inspired 3DVG with double-sided peak-valley structures that exhibits a 43.2% improvement over conventional plane evaporators. Our comprehensive heat and mass transfer studies reveal that the enhancement is not solely caused by the well-established dark evaporation increase but also by airflow restructuring, which reduces vapor diffusion resistance and facilitates thermal energy redistribution. Moreover, in practical scenarios considering the sun position, the 3DVG exhibits a remarkable 31.9% enhancement in outdoor solar energy harvesting. In multiple 5-day-long outdoor experiments under varying conditions, our device produced water ranging from 1.088 to 8.863 kg m^{-2} day^{-1}. These discoveries shed light on the fundamental mechanisms governing 3D evaporation enhancement and hold promising implications for practical solar desalination devices.

INTRODUCTION

The lack of access to freshwater is an ongoing problem for many communities, and the crisis is likely to worsen with climate change, posing challenges for the sustainable development of humankind.[1,2] The United Nations has recognized this issue and addressed it through sustainable development goal 6, which aims to foster the exploration of viable solutions for alleviating freshwater shortages.[3] Unconventional water resources, including seawater,[4–6] wastewater,[7] and atmospheric water,[8–12] can be readily converted into freshwater, although the sustainability of this approach relies on the environmental footprint and energy demand of the conversion techniques. Among the various techniques available, interfacial solar evaporation offers a passive and decentralized method to extract pollutants and salts from untreated water resources, thus enabling high-efficiency desalination and wastewater treatment.[13,14]

The continuous development of evaporator materials and designs has led to notable improvements in the solar evaporation rate, surpassing 10 kg m^{-2} h^{-1}, and energy efficiencies of over 90%.[15,16] Numerous materials have played a role in improving water evaporation efficiency by enhancing photothermal conversion,[17–20] managing water supply,[21–23] and reducing latent heat.[24–27] The utilization of materials with specific topographies and morphologies, such as hierarchical structures,[17,28] micro-3D structures,[29–31] sharply dimpled surfaces,[32] and stimulus hollow fibers,[33] further amplifies the evaporation rate. In conjunction with materials and micro-structure design, advanced heat and

Please cite this article in press as: et al., Improving solar water harvesting via airflow restructuring using 3D vapor generator, Device (2023), https://doi.org/10.1016/j.device.2023.100065

mass transfer strategies also play key roles in managing water and energy flow within solar evaporation systems. These strategies encompass latent heat recovery[34–36] and salinity regulation,[37–40] which have collectively yielded breakthrough outcomes in terms of overall performance. Moreover, to address the challenge of salt accumulation during seawater evaporation, advanced methodologies such as enhanced diffusion,[23,41] contactless evaporation,[42,43] and convection flow[37,44] have been introduced.

The macroscopic 3D architecture offers a versatile platform for incorporating diverse materials and micro-structural designs. Beyond its adaptability, this approach provides a way to further optimize solar energy capture and utilization of ambient energy of existing designs.[45–47] It provides a way for creating improved interfaces conducive to water-gas evaporation, resulting in elevated rates and efficiency. The extended 3D evaporation surfaces can also facilitate faster vapor escape from vapor generators.[31,48] However, the fundamental mechanism behind this evaporation enhancement remains not well understood, particularly concerning the inability of the dark evaporation growth model to fully explain this augmentation.

Although laboratory studies have achieved high evaporation efficiency close to the thermodynamic limit,[49] real-world outdoor evaporation performances for these reported devices under complex natural sunlight conditions often fall short of the limit. Given that solar energy serves as the primary energy input for passive evaporation systems, factors such as solar flux, sunlight duration, and dynamic illumination angles impact the solar intensity and the overall input energy amount received by solar vapor generators (SVG), thereby determining daily water production yield.[45,50,51] Consequently, optimizing the inclination angle of the SVG is essential for maximizing solar energy harvest, akin to optimizing photovoltaic panels.[52] The integration of multiple inclined surfaces in 3D macroscopic SVGs shows promise in capturing complex incident sunlight and enhancing solar energy harvesting.

In this study, we developed an origami-inspired 3D SVG (3DVG) using active carbon fiber felts with broad-spectrum sunlight absorption. The 3DVG features a double-sided 3D evaporation structure that promotes vapor escape through peak and valley structures and enhances solar harvesting from multiple illumination angles. The 3DVG achieved an impressive evaporation rate of 1.69 kg m^{-2} h^{-1} with a maximum energy efficiency of 96.1%. Experimental and simulation validation demonstrated that the maximum evaporation rate of the 3DVG was 43.2% higher than that of conventional flat evaporators. Thermodynamic simulations around the evaporator provided insights into the enhancement mechanisms of the 3DVG, revealing that the double-sided 3D evaporation structure enhances vapor diffusion, eliminates vapor stagnation, and reduces heat loss, leading to improvements in evaporation rate and energy efficiency. Under outdoor conditions, the 3DVG exhibited superior performance, with a maximum increase of 31.9% in energy harvesting compared to flat evaporators when taking into account the solar altitude angle and solar zenith angle. A continuous 5-day outdoor water production experiment confirmed the dual enhancement effects of the 3DVG, resulting in a water production yield of 1.088–8.863 kg m^{-2} day^{-1} with a 52%–84% improvement. These findings elucidate the mechanisms underlying 3D evaporation enhancement and are expected to facilitate the practical implementation of solar evaporation systems.

RESULTS AND DISCUSSION

Design and characteristics of 3DVG

Macroscopic-scale 3DVG enhances evaporation performance by providing effective water-air interfaces for phase transition and extended surfaces for vapor escaping. The 3D evaporation structure with multiple solar-energy-receiving surfaces also reduces the dependence of the evaporation performance on the solar illumination direction, enabling improved solar energy harvesting and efficient evaporation in various seasons and locations. Taking inspiration from origami, we fabricated a 3DVG with multiple peaks and valleys using active carbon fiber felt (ACFF) through a fixing, immersing, and drying process (Figure 1A). Silica sol, acting as a fiber binder, was used to create the self-supporting 3D structure.[53]

The scanning electron microscopy (SEM) and energy-dispersive spectroscopy (EDS) images of the initially prepared materials showed the formation of silicon dioxide from the drying of silica sol (Figure 1B). Notably, silicon dioxide particles are adhered to the fiber surface at both micrometer and nanometer dimensions (Figure 1C).[54] This adhesion is facilitated by the presence of abundant micropores on the ACFF surface (Figure S1). Some of the silicon dioxide crystals are several tens of micrometers in size and, when situated between the fibers, may have further enhanced the mechanical properties of the materials. This morphology remained unchanged after evaporation in pure water, saline water, and real seawater (Figure S2). The silicon layer securely attached to the fibers, and the micrometer-sized silicon dioxide crystals also persist in the fiber entanglement gaps (Figure S3). Distinctively, upon evaporation in seawater, the visible adhesion of various types of salts (NaCl, $MgCl_2$, $MgSO_4$, $CaSO_4$, etc.) was observed (Figure S4). Fortunately, these salt deposits did not obstruct water transport channels; instead, they adhered to the fiber surface. The mechanical strength is also confirmed through load tests (Figure 1D). These results provide evidence for the long-term durability and stability of the materials.

The intertwined structure of the ACFF forms micron-scale gap structures that enhance water-pumping and vapor-escaping capabilities. Water droplets are fully absorbed within 500 ms (Figure S5). The rising height and rate of the 3DVG and raw ACFF were characterized using an infrared camera (Figure S6), demonstrating that both materials allow water to climb over 10 cm within 100 s (Figure 1E). The prepared 3DVG exhibits a higher climbing rate and height than raw ACFF, indicating stronger hydrophilicity and capillarity from the introduction of silica gel particles with hydrophilic silanol (Si-OH) groups.[55] This increases the water supply capacity for evaporation. Additionally, the hydrophilic nature of the fibers facilitates the formation of multiple small-area water films at fiber intersections, further increasing the evaporation rate.

Apart from water supply, solar absorption is another crucial parameter of the 3D vapor generator. The material used in the 3DVG exhibits an optical absorption rate of 96.8% for the full solar spectrum, attributed to the inherent black carbon materials and light trapping by the intertwined and coiled fibers (Figure 1F). After wetting by pure water, saline water, and seawater, the wetted materials exhibit a reduction in reflectance across the entire spectrum (Figure S7). This phenomenon can be attributed to the decrease in interfacial light scattering occurring at the

Please cite this article in press as: et al., Improving solar water harvesting via airflow restructuring using 3D vapor generator, Device (2023), https://doi.org/10.1016/j.device.2023.100065

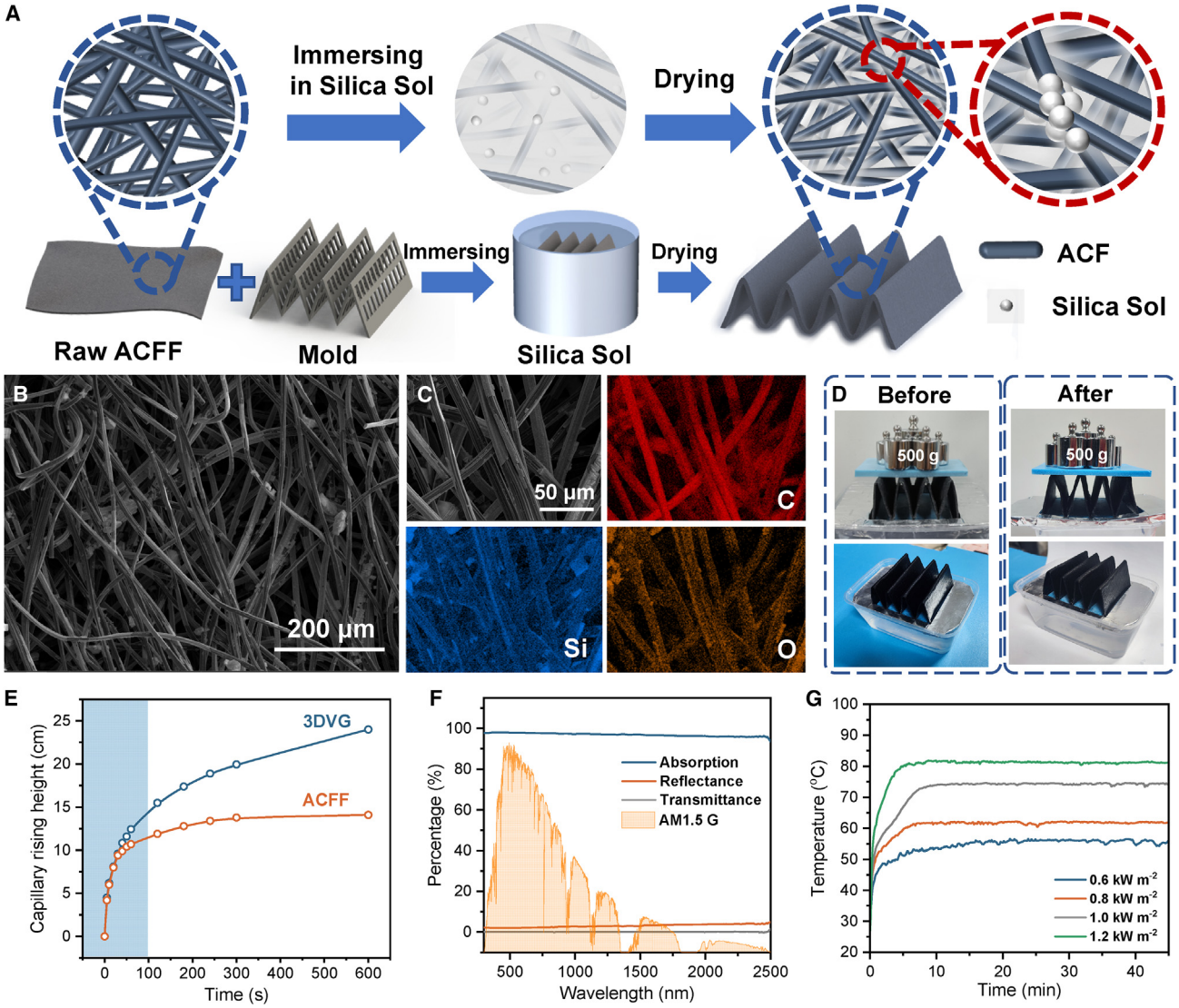

Figure 1. Preparation and characteristics of the 3DVG and the PVG

(A) Diagram of the preparation of the 3DVG. The raw ACFF is immersed in the silica sol and then dried on a mold with a 4-fold peak and valley structure to form the 3DVG.

(B) SEM image of the as-prepared material of the 3DVG.

(C) EDS images and the enlarged SEM image of the as-prepared 3DVG materials, confirming the distribution of silica nanoparticles.

(D) Photos of the as-prepared 3DVG and the 3DVG after evaporation that withstands a weight of 500 g without breaking, demonstrating its mechanical stability.

(E) Dynamic capillary rising height of the ACFF and 3DVG, illustrating that the capillary rising height and rate of the 3DVG are higher than the ACFF due to the integration of the hydrophilic silica nanoparticles.

(F) Absorption, transmittance, and reflectance spectra of the wet 3DVG. The normalized spectral solar irradiance density of the air mass 1.5 global (AM 1.5G) solar spectrum is shown by the orange line.

(G) Variations of the average temperature of the dry 3DVG under simulated solar sunlight, showing a rapid and large temperature increase owing to the strong solar absorption capacity.

liquid-to-material interface, as opposed to the air-to-material interface observed in the dry state.[56] Conversely, the redried materials demonstrate an increase in reflectance due to salt crystallization; however, this effect is relatively small and remains within ±3%. With superior solar absorption, the dry 3DVG reaches equilibrium temperatures of 55.9°C–78.1°C under solar irradiation of 0.6–1.2 kW m^{-2} within 15 min (Figure 1G), demonstrating good photothermal conversion capacity.

Evaporation enhancement and its mechanism

The laboratory solar evaporation performances of the 3DVG and the plate vapor generator (PVG) were tested under simulated sunlight with an intensity of 1 kW m^{-2} (Figure 2A). Water is supplied to the 3DVG via two supporting feet, while the middle part of the 3DVG is suspended to achieve a double-sided 3D evaporation configuration (Figure S8). The mass changes of the 3DVG and the PVG during evaporation were recorded (Figure 2B), and

Please cite this article in press as: et al., Improving solar water harvesting via airflow restructuring using 3D vapor generator, Device (2023), https://doi.org/10.1016/j.device.2023.100065

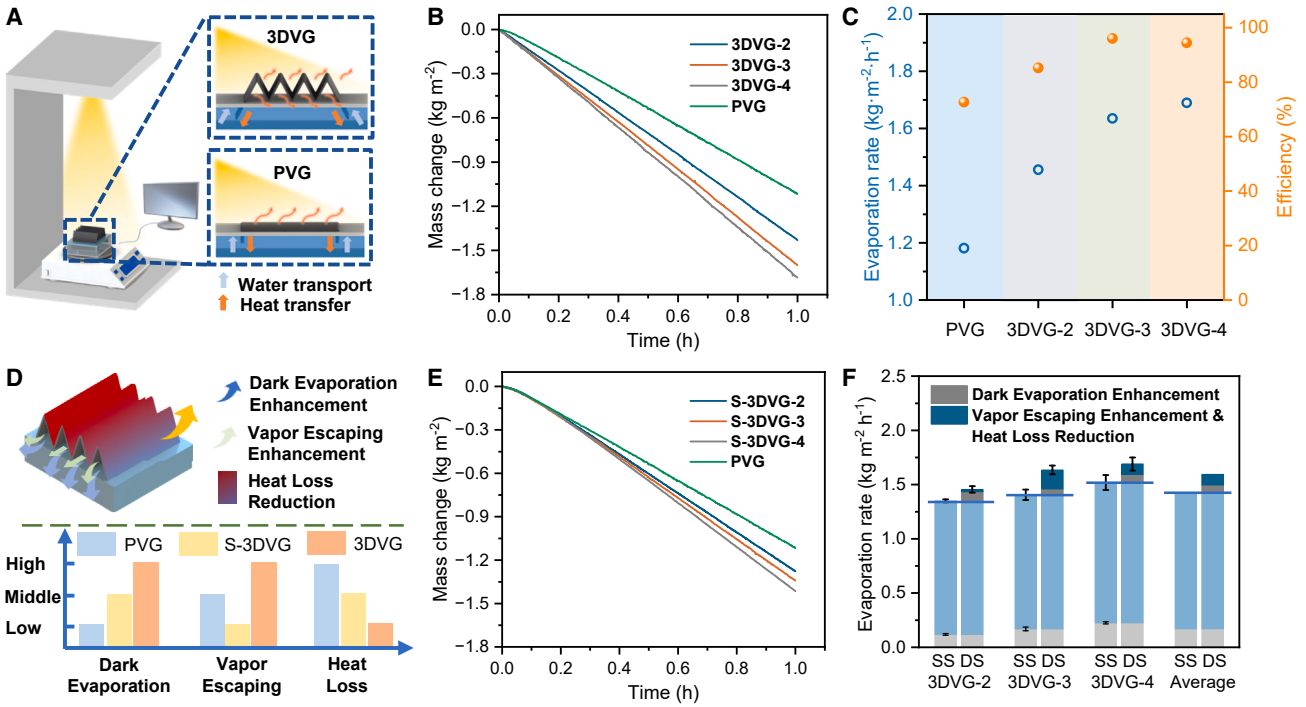

Figure 2. Solar vapor generation of 3DVG and PVG under one sun

(A) Schematic diagram of the setup for the water evaporation performance test and the corresponding vapor generators.

(B) Mass change curves for the 3DVG with different heights under one sun in comparison to the PVG as the control test.

(C) Evaporation rates and efficiency of 3DVG-2, 3DVG-3, 3DVG-4, and the PVG, showing a 43.2% enhancement for 3DVG-4 in the water evaporation rate.

(D) Three contributing factors and their relative proportions for the enhanced evaporation performance of 3DVG in comparison to the PVG.

(E) Mass change curves for the single-sided 3DVG (S-3DVG) with different heights to further analyze the increase of evaporation rate caused by the change in the airflow pattern and the temperature distribution.

(F) Analysis of the evaporation performance enhancement and their contributions to the overall evaporation rate. All error bars: standard deviation (SD).

the slopes of the curves represent the evaporation rates. As shown in Figure 2C, the PVG exhibited an evaporation rate of 1.18 kg m^{-2} h^{-1} under one sun, while the 3DVGs with varying heights (labeled as 3DVG-x, where x represents the height of the 3DVG in centimeters) achieved enhanced water evaporation performance. 3DVG-4 achieved a maximum evaporation rate of 1.69 kg m^{-2} h^{-1}, while 3DVG-3 achieved a maximum energy efficiency of 96.1% (Figure 2C), which are 43.2% and 32.2% higher than that of the PVG, respectively. Note that although 3DVG-4 exhibits a higher evaporation rate compared with 3DVG-3, its efficiency does not surpass that of 3DVG-3. This outcome can be attributed to the trade-off between the evaporation surface areas and the airflow escape. Specifically, more evaporation resulting from the increased evaporation surface areas necessitates efficient vapor discharge. Nevertheless, the heightened elevation of the SVG leads to a narrower outlet for vapor expulsion, causing a slowdown maximum airflow velocity of 3DVG-4 (188.1 mm s^{-1}) on the lower channels (Figure S9) and, consequently, lower efficiency.

The augmentation of evaporation performance can be attributed to three fundamental factors, as revealed through comprehensive analysis of heat and mass transfer: (1) intensified dark evaporation stemming from the expanded evaporation surface, (2) the enhanced but previously overlooked vapor-escaping pathways and modified airflow patterns of the double-sided evaporation structure,[29,31] and (3) mitigated heat dissipation to the bulk water and the ambient (Figure 2D).[57,58] Precisely, the developed 3DVG, characterized by intricate peaks and valleys and a double-sided design, substantially amplifies the evaporation area, ~4.14 times greater than that of the conventional PVG, thereby resulting in notable advancements in dark evaporation rates (effect 1). Furthermore, the 3DVG affords a more expansive vapor diffusion space per unit evaporation area, effectively diminishing vapor diffusion resistance (effect 2). This reduction in resistance engenders a reorganized vapor diffusion pattern around the evaporator, facilitating expeditious vapor diffusion, which is detailly revealed in the following section. The modifications in temperature distribution within the SVG, along with the water supply (positioned at both ends while leaving the middle suspended without contacting the water), collectively contribute to reducing heat dissipation (effect 3). This, in turn, enhances the overall energy efficiency. Overall, the synergistic interplay of these three factors yields substantial improvements in evaporation performance and energy efficiency.

To isolate and quantify the contributions of the three effects mentioned, we introduced a single-sided 3D vapor generator (S-3DVG) with a foam layer to prevent vapor generation on the bottom surface (Figure S10). The S-3DVG exhibited lower

Please cite this article in press as: et al., Improving solar water harvesting via airflow restructuring using 3D vapor generator, Device (2023), https://doi.org/10.1016/j.device.2023.100065

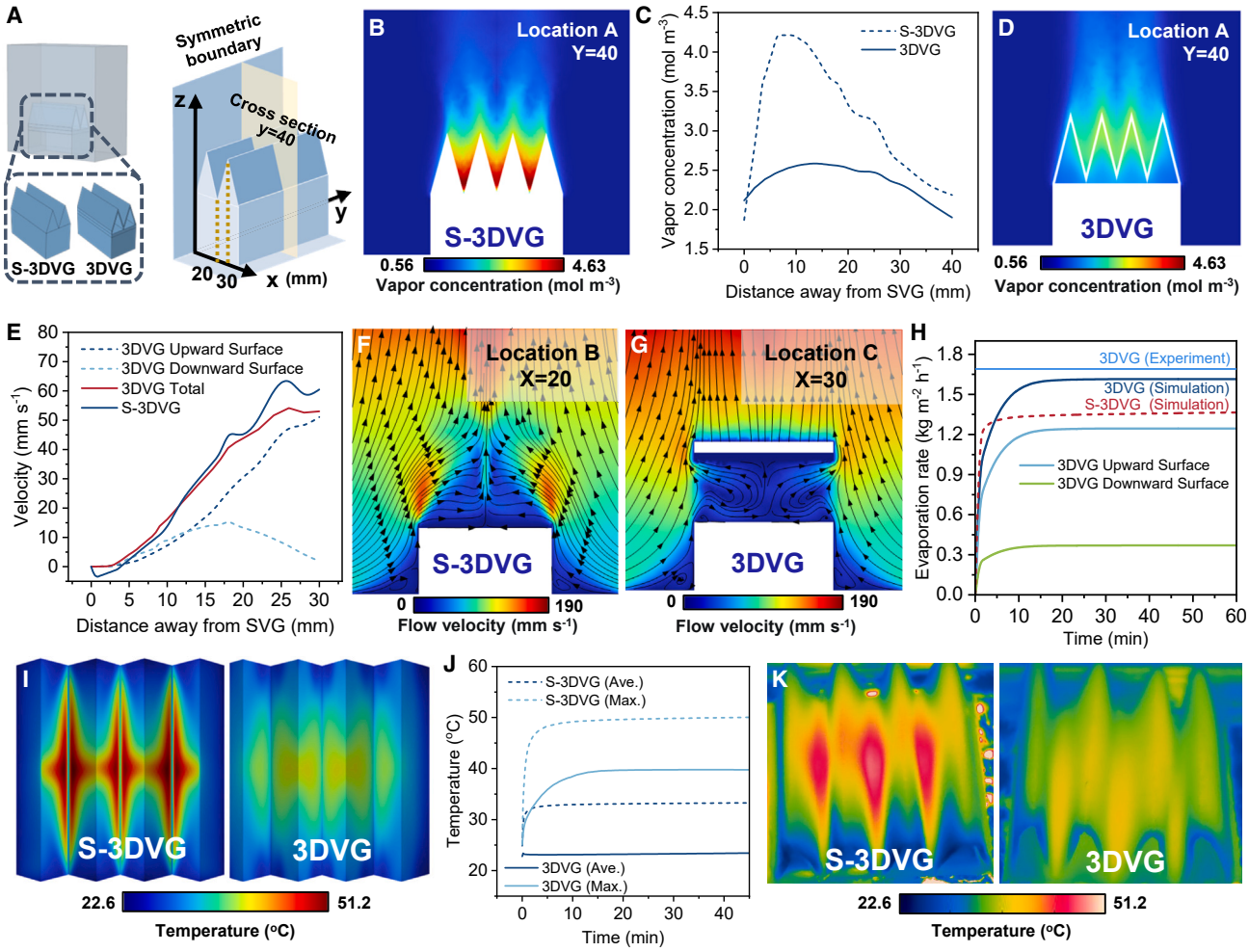

Figure 3. Exploring the underlying mechanisms of evaporation enhancement of the double-sided 3DVG

(A) Diagram of the simulation geometry model depicting the locations of labeled cross-sections.

(B) Cross-section mapping of vapor concentration near the S-3DVG at location A (y = 40 mm).

(C) Changes in vapor concentration at different positions from the 3DVG and S-3DVG evaporators.

(D) Cross-section mapping of vapor concentration near the 3DVG at location A (y = 40 mm).

(E) Changes in velocity at different positions from the 3DVG and S-3DVG evaporators. For the 3DVG, upward velocity is calculated from the valley to the top, and downward velocity is calculated from the top to the valley of the 3DVG.

(F) Cross-section mapping of airflow velocity near the S-3DVG at location B (x = 20 mm).

(G) Cross-section mapping of airflow velocity near the 3DVG at location C (x = 30 mm).

(H) Simulated evaporation rates from the upward and downward surfaces of 3DVG and S-3DVG, and the simulated and experimental overall evaporation rates of 3DVG and S-3DVG.

(I) Temperature distributions of S-3DVG and 3DVG obtained from the simulation results when evaporation reaches equilibrium.

(J) Simulated average and maximum temperature variations of S-3DVG and 3DVG.

(K) IR images of S-3DVG and 3DVG.

evaporation rates of 1.35, 1.41, and 1.52 kg m^{-2} h^{-1} for evaporator heights of 2, 3, and 4 cm, respectively, in comparison to the double-sided 3DVG (Figure 2E). By comparing the dark evaporation rates between 3DVG and S-3DVG, it was observed that the enhanced dark evaporation from the bottom surface accounted for 0.054–0.084 kg m^{-2} h^{-1} (effect 1), contributing to an average of 42% of the overall increase (Figure 2F; Table S1). After excluding the enhancement in dark evaporation from the bottom surface, a remaining increase of 58% in the evaporation rate was still evident, which could be attributed to the subsequent two effects. These effects involve changes in vapor diffusion and airflow patterns around the SVG (effect 2) as well as temperature variations of the SVG (effect 3).

To gain further insights into the remaining two potential effects contributing to enhanced evaporation, we conducted simulations using the software COMSOL Multiphysics to obtain and analyze vapor concentration, airflow velocity, and temperature distributions near SVGs during evaporation (see Note S1). We extracted the characteristic cross-sectional positions at y = 40, x = 20, and x = 30, denoting them as locations A, B, and C,

Please cite this article in press as: et al., Improving solar water harvesting via airflow restructuring using 3D vapor generator, Device (2023), https://doi.org/10.1016/j.device.2023.100065

respectively (Figure 3A). The vapor concentration between the valleys and peaks on the surface of the S-3DVG shows distinct characteristics because of the varying vapor diffusions at the different positions (Figure 3B). The valley region of the S-3DVG exhibits a vapor concentration 1.6 times higher than that at the peak region, with a maximum difference of 3.44 mol m^{-3} and an average concentration of 2.12 mol m^{-3} (Figure S11). This discrepancy arises from the occurrence of evaporation in a relatively narrow valley space, where the evaporation area significantly exceeds the vapor-escaping space, leading to the formation of a vapor "stagnation zone." Conversely, the double-sided 3DVG does not experience such a stagnation zone, primarily because its dual-sided evaporation structure provides additional downward airflow space. As a result, the vapor concentration surrounding the double-sided 3DVG exhibits a uniform distribution, with a concentration difference of only 0.48 mol m^{-3} and a lower average vapor concentration of 1.84 mol m^{-3} (Figure S12), demonstrating smooth vapor exclusion that prevents vapor accumulation around the evaporator and facilitates continuous evaporation. We captured the variation in vapor concentration as a function of position from the valley bottom to the evaporator top, revealing that the double-sided 3DVG exhibits a more gradual vapor change, whereas the single-sided variant reaches its maximum value and experiences vapor accumulation at 10 mm away from the evaporator surface (Figure 3C). The vapor concentration surrounding the 3DVG exhibits a uniform distribution, thereby providing confirmation of the vapor distribution effect and the enhancement of airflow (effect 2; Figure 3D).

We analyzed the airflow quantity and vector characteristics of the SVGs, which revealed that the airflow velocity in the valley of the single-sided S-3DVG decreased to 2.3 mm s^{-1} and exhibited an inward direction toward the evaporator, as shown by the representation of negative velocity values at a height less than 5 mm (Figure 3E). The velocity distribution contour map provides a more intuitive confirmation of the insufficient vapor escaping and subsequent reduction in evaporation (Figure 3F). At the peak of the S-3DVG, we observed that the vapor accelerated upward, reaching a maximum airflow rate of 75 mm s^{-1}. This phenomenon is facilitated by natural convection generated by the temperature difference between the moist air and the S-3DVG.

The double-sided 3DVG exhibits two separate airflow streams, with velocities reaching up to 51 mm s^{-1} from the upward surface and 15 mm s^{-1} from the downward surface, respectively. In addition to the velocity values, the vapor diffusion pattern also changes. The upstream air flows into the bottom channel of the 3DVG and converges in the middle of the bottom channel, resulting in an accelerated airflow for fast vapor escaping (Figure 3G). This change in airflow magnitude and direction prevents the occurrence of flow stagnation and promotes evaporation. Additionally, it has been observed that the increased height of the 3DVG contributes to enhanced vapor distribution and flow, which helps improve the evaporation rate. The overall evaporation rate considering upward and downward surfaces of the double-sided 3DVG demonstrates a considerable improvement compared to the S-3DVG configuration (Figure 3H). The bottom surface plays a crucial role in promoting evaporation, resulting in an increase ranging from 16.7% to 22.9% compared with the single-sided S-3DVG (Figure S13).

This particular airflow configuration also affects the temperature distribution pattern. The S-3DVG shows a distinct high-temperature region within the stagnation zone (Figures 3I and S14). Within this zone, the temperature increases to 50.2°C, with a temperature difference of 16.8°C compared with the average temperature (Figure 3J). On the other hand, the 3DVG exhibits a uniform and lower temperature distribution, with an average temperature of 39.8°C (for infrared [IR] images, see Figures 3K and S15). The lower temperature observed in the 3DVG indicates a reduction in radiative and convective heat losses (effect 3), thus indicating higher energy efficiency. In contrast, the PVG, lacking these distinctive characteristics, exhibits a higher temperature of around 12°C when compared with the 3DVG (see Figure S16), resulting in a lower evaporation efficiency of 72.7%. These findings collectively provide evidence that the enhanced evaporation observed in the 3DVG design can be attributed to factors such as dark evaporation from the bottom surface, improved vapor diffusion around the SVG, and overall minimization of heat losses within the SVG.

Therefore, the decoupled experimental results have demonstrated that the 3D structure not only enhances the overall evaporation rate and efficiency by increasing dark evaporation but that it also provides additional pathways for vapor escape and flow, which helps avoid vapor stagnation on the evaporator surface. This prevents a localized increase in relative humidity, thereby reducing vapor transport resistance in the air. Additionally, it results in the redistribution of heat within the evaporator, leading to reduced heat loss. These combined effects contribute to higher evaporation rates and efficiency.

Evaporation performance in practical scenarios

One important difference between laboratory and real-world conditions is the sun's trajectory[47] (i.e., the variability in solar altitude angle θ, solar azimuth angle α) and solar irradiation intensity throughout the day and across different seasons[59](Figure 4A). These factors must be considered to ensure the long-term practical performance and durability of SVGs. For conventional plate evaporators, the utilization of incident solar energy is limited, as the projection area to sunlight changes as the sun moves across the sky. This issue is similar to that faced by stationary solar panels, where the installation angle needs to be optimized based on geographical location. Figure 4B illustrates this concept, where the effective solar radiation received by a plate evaporator with a solar altitude angle of θ is $q_{sun} \cos \theta$. In contrast, the 3DVG with an inclination angle $(90^\circ - \beta)$ can receive more solar radiation, $q_{sun} \sin(\theta + \beta)$. This effect becomes particularly obvious when the solar altitude angle θ is close to 90°, such as during sunrise or sunset. To evaluate the influence of the solar altitude angle θ on overall energy-harvesting performance, we developed a dynamic solar irradiation harvest model, assuming a consistent daily solar path from southeast (α = 45°) to northwest (α = 135°) (see Note S2).

The accumulated solar radiation over the course of a day is depicted in Figure 4C, showing that the 3DVG accumulates 25.9% (42.2 kJ) more energy than the PVG over the entire day, which is utilized for evaporation purposes. The detailed analysis of each surface of the 3DVG reveals that the 3DVG can receive more than twice the solar energy (23.4 kJ) than the PVG (11 kJ) during the early morning period (6–8 a.m.) due to the #1 and #3 surfaces

Please cite this article in press as: et al., Improving solar water harvesting via airflow restructuring using 3D vapor generator, Device (2023), https://doi.org/10.1016/j.device.2023.100065

CellPress

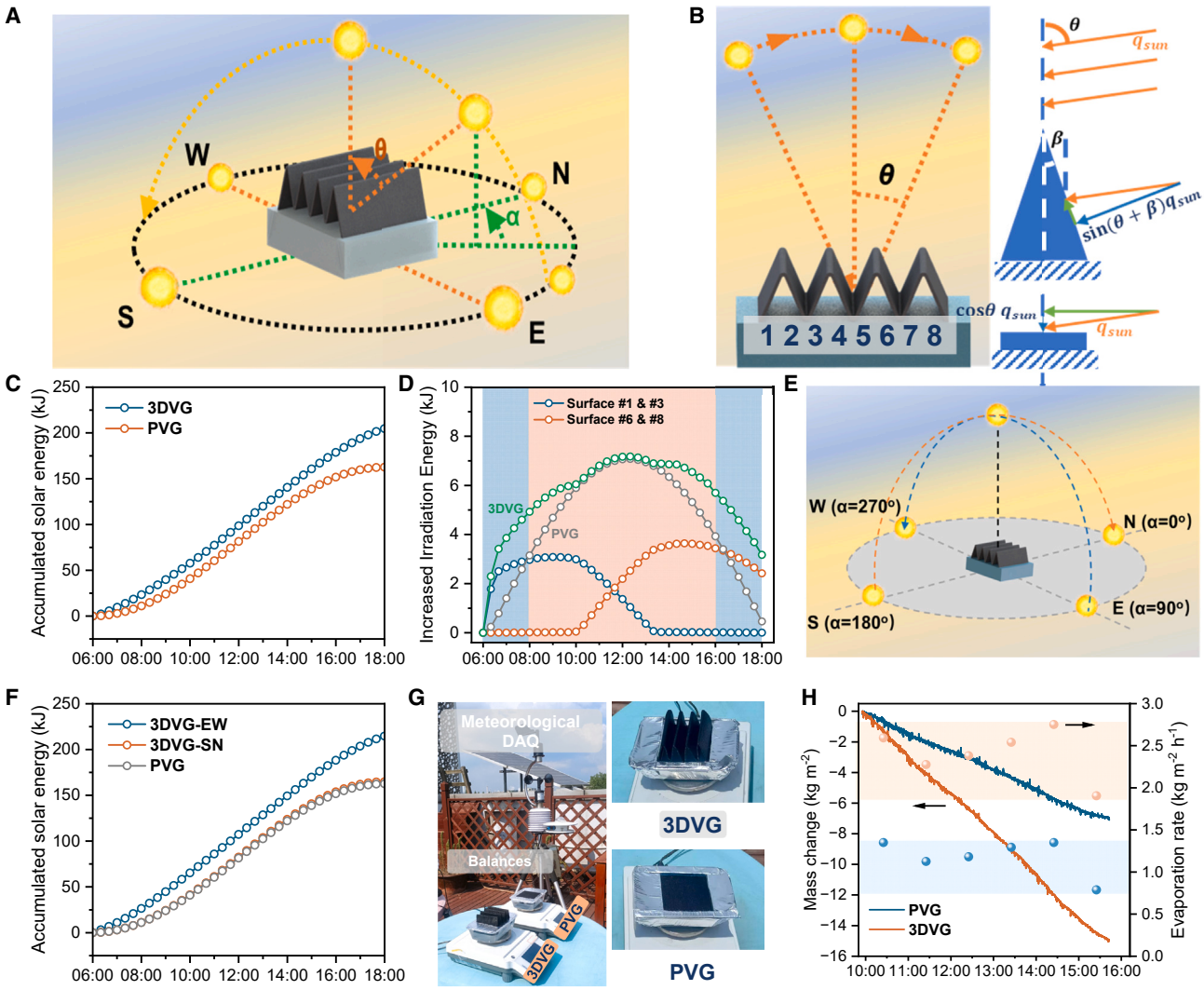

Figure 4. Effect of the solar illumination directions on outdoor evaporation performance

(A) Sunlight illumination on the 3DVG from different directions. The zenith angle α and the altitude angle θ describe the solar position.

(B) The influence of altitude angle θ on the solar energy received by the surface with different tilt angles.

(C) The accumulated solar energy received by the 3DVG and PVG.

(D) The received irradiation energy by #1 and #3 surfaces, #6 and #8 surfaces, all surfaces of the 3DVG, and the PVG during each 20-min period.

(E) Two extreme cases of the solar path under simulated conditions.

(F) The accumulated solar energy received by the 3DVG with the solar paths from south to north (SN) and from east to west (EW).

(G) Photos of the setup of the outdoor solar water evaporation tests.

(H) Mass changes and evaporation rates under the outdoor conditions for PVG and 3DVG.

(labeled in Figure 4B) receiving more irradiation (Figures 4D and S17). A similar effect can be observed at sunset, although the inclined surfaces that receive more irradiations change to the #6 and #8 surfaces with variations in solar irradiation direction. This indicates that the 3DVG can initiate evaporation earlier at sunrise and can continue operating later at nightfall. During the remaining hours (8 a.m. to 4 p.m.), the 3DVG also receives more solar irradiation, ultimately promoting the overall solar energy harvesting.

Considering the impact of the solar azimuth angle α, the accumulated solar energy received by the PVG remains unchanged. However, in the case of the 3DVG, the elevated section of the structure may obstruct sunlight, leading to a potentially reduced energy-harvesting enhancement effect. To examine this, we investigated two extreme scenarios: $\alpha = 180^\circ$ to 0° (referred to as SN, representing the south-to-north direction) and $\alpha = 90^\circ$ to 270° (referred to as EW, representing the east-to-west direction), as illustrated in Figure 4E. Simulation results elucidated that the daily accumulated solar energy for the 3DVG reached its pinnacle at 215 kJ, when the projection line of the solar path aligned vertically with the peak direction of the 3DVG (3DVG-EW) (Figure 4F). The variations in irradiation intensity across

Please cite this article in press as: et al., Improving solar water harvesting via airflow restructuring using 3D vapor generator, Device (2023), https://doi.org/10.1016/j.device.2023.100065

distinct surfaces of the 3DVG throughout the day are depicted in Figure S18, underscoring the sequential exposure of different surfaces of the 3D structure to solar radiation, culminating in a greater cumulative solar energy. Conversely, when these two lines are parallel (3DVG-SN), the 3DVG receives the minimum daily solar energy input, which closely approximates the 163 kJ obtained by the PVG. Quantitative analysis reveals that the potential enhancement in evaporation rate attributable to augmented energy harvesting can soar up to 31.9%. Hence, it is evident that the energy-harvesting capacity of the 3DVG consistently surpasses that of the PVG irrespective of the position of the sun, consequently augmenting the daily energy input for water evaporation and showcasing the formidable adaptability of 3DVG to environmental conditions.

Based on the analysis, we have obtained insights into the enhanced performance of the 3DVG structure compared with the PVG in both laboratory and outdoor settings. To further validate the evaporation enhancement achieved by the 3DVG under real outdoor conditions, we conducted outdoor solar evaporation experiments as depicted in Figure 4G. The PVG and the 3DVG were placed on the rooftop of the Green Energy Laboratory (GEL) at Shanghai Jiao Tong University (SJTU), with an average ambient temperature, relative humidity, and wind speed of 37.5°C, 44.9%, and 1 m s^{-1}, respectively (Figure S19). The mass changes of the SVGs were recorded throughout evaporation. The cumulative incident solar energy over the experimental period amounted to 14.8 MJ m^{-2} (Figure S20). The variations in mass and evaporation rate for the 3DVG and PVG are presented in Figure 4H. Notably, the 3DVG exhibited remarkably high evaporation rates of 2.59 kg m^{-2} h^{-1} under clear sky conditions during late morning hours (10–11 a.m.), representing an impressive 92% increase compared with the PVG. During the period characterized by weak solar intensities and high solar altitude angles (3–4 p.m.), the evaporation rates for the 3DVG and the PVG were measured at 1.91 and 0.79 kg m^{-2} h^{-1}, respectively. Interestingly, during this period, the evaporation rate increase (142%) was even more substantial than that observed near noon, confirming the exceptional solar energy-harvesting capacity demonstrated by the 3DVG at high solar altitude angles. Furthermore, the measured improvement in evaporation surpassed the combined effect of the inherent evaporation enhancement (maximum 43.2%) and the energy-harvesting enhancement (maximum 31.9%), owing to the effective utilization of natural outdoor convection to promote evaporation. Overall, these findings highlight the comprehensive advantages offered by the 3DVG over conventional PVGs when operating in real outdoor conditions.

Solar desalination and water production performance

To investigate the potential of 3DVGs for solar desalination, we conducted continuous evaporation experiments using saline water (3.5 wt % NaCl solution) for 13 h and real seawater for 65 h under simulated 1 kW m^{-2} solar irradiation. It is important to note that the energy input during the 65-h solar experiment is equivalent to that of the over-14-day typical outdoor natural solar energy input. Meanwhile, no nighttime salt diffusion occurred in these continuous evaporation experiments. The situations tested correspond to harsher conditions than those encountered in most outdoor solar desalination scenarios.

The mass change curve and real-time evaporation rate for saline water are presented in Figure S21, where the evaporation rate ranged from 1.65 to 2.01 kg m^{-2} h^{-1}, with an initial dark evaporation rate of 0.37 kg m^{-2} h^{-1}. For real seawater, the 3DVG showed stable evaporation rates of 1.71–2.06 kg m^{-2} h^{-1}, with an initial dark evaporation rate of 0.23 kg m^{-2} h^{-1} (Figure 5A). This demonstrated that processing the complex ions in the seawater will not highly affect the evaporation rate, and even the evaporation rate is higher than that in pure water, which is attributed to the higher ambient temperature and the slight temperature increase in the bulk water during the continuous evaporation, leading to enhanced dark evaporation.

To visualize potential salt fouling, we captured IR images during evaporation (Figures 5B and S22). These images indicate that the initial temperature distribution of the 3DVG during evaporation is uniform, similar to that observed during pure water evaporation. However, a significant temperature elevation is observed at the middle-bottom portion of the 3DVG, with this area gradually expanding and the overall evaporator temperature rising over time, especially during seawater evaporation, where the temperature degradation is more pronounced and accelerated. Beyond 48 h of seawater evaporation, this temperature elevation zone stabilizes. The underlying cause of this phenomenon may be attributed to insufficient water supply in the central region, resulting in partial blockage of the water transport channel. The SEM and EDS images of the post-evaporation materials provide valuable insights (Figure 5C). The NaCl salt shells are observed on the fiber surfaces following continuous 13-h evaporation in the saline water (Figure S23). Some adherence of the salt shell between adjacent fibers was noticed. However, the deposition was not severe, and the fiber gaps remained unblocked for capillary water supply and vapor escaping. Moreover, the presence of Si on the fiber surface indicated the shape stability. Similarly, for the materials after 65-h seawater evaporation, no prominent obstruction caused by salt particles, such as NaCl or $MgSO_4$, was observed (Figures 5D and S24). The observed increased evaporator temperature may be attributed to the formation of the salt shell, leading to reduced capillary forces, although this salt shell has a minimal impact on light-to-heat conversion and micro-scale vapor diffusion. Nevertheless, experimental results demonstrate that this encasement phenomenon has negligible influence on the overall evaporation performance of the fibers. Additionally, we conducted a salt diffusion experiment using an excess of NaCl, and the images depict the efficacy of NaCl diffusion during nighttime, further confirming the stability and feasibility of the 3DVG during day-night solar desalination cycles (Figure S25).

In addition to the desalination tests, the outdoor water production performance is also evaluated. The water production device is made of transparent acrylic sheets where hydrophilic coatings were applied to enable efficient condensation and water sliding (Figure S26). Temperature variations were monitored using thermocouples that connected to a data acquisition instrument (Figure 5E). To evaluate the evaporation and water production performance of the prepared SVGs under different climatic conditions, typical sunny (Shanghai, China, October 18, 2022) and dark cloudy days (October 16, 2022) were selected. The solar intensity variations and the accumulated incident solar energy for these days are illustrated in Figure 5F, indicating daily solar

Please cite this article in press as: et al., Improving solar water harvesting via airflow restructuring using 3D vapor generator, Device (2023), https://doi.org/10.1016/j.device.2023.100065

CellPress

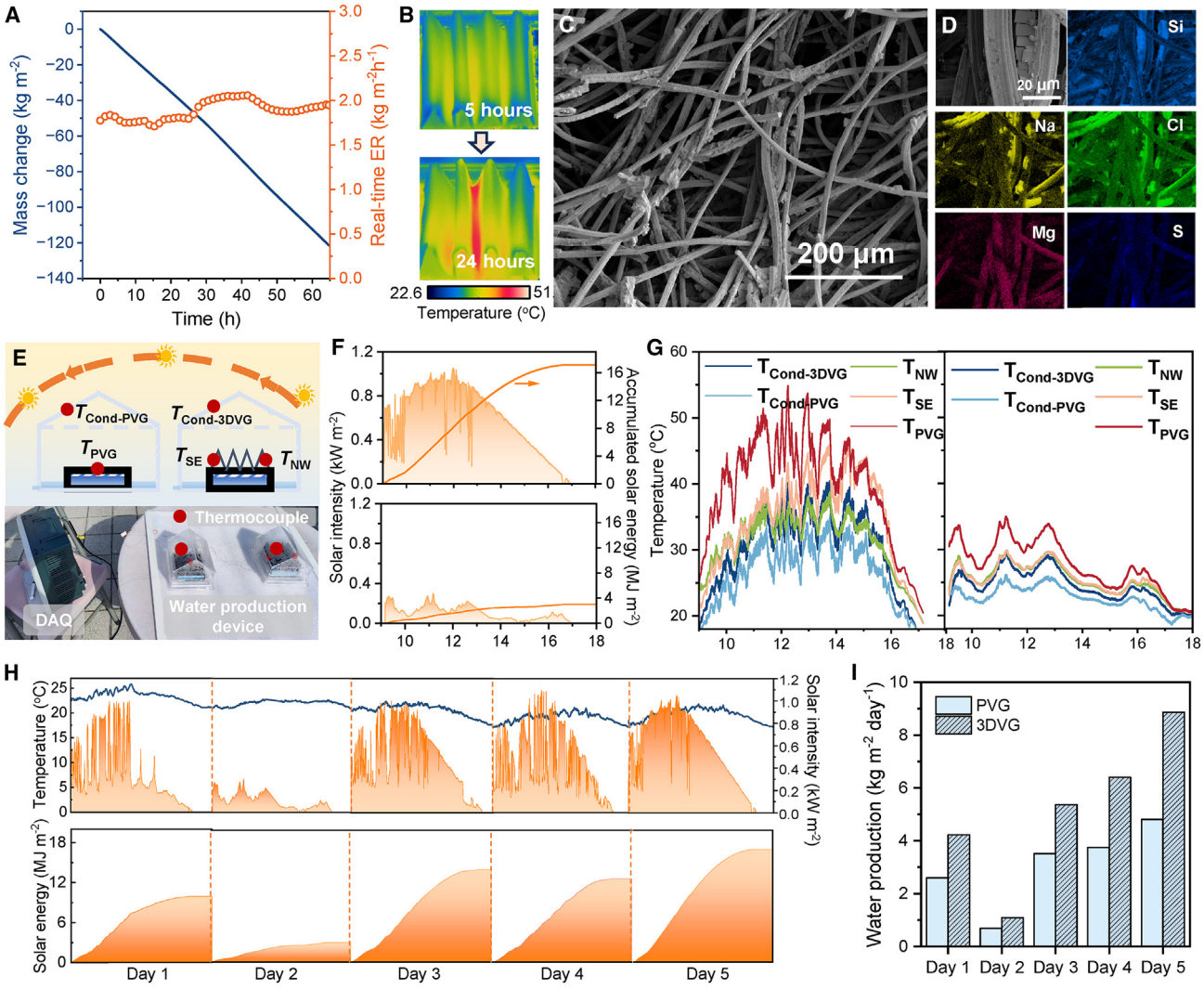

Figure 5. The comprehensive performance analysis of solar desalination and outdoor water production using 3DVG and PVG

(A) The mass change curve and real-time evaporation rate observed during the actual seawater evaporation process.

(B) IR images of the 3DVG during the evaporation of seawater, allowing visualization of the temperature distribution and heat transfer within the system.

(C) SEM image of the 3DVG after a prolonged 65-h seawater evaporation process, providing a closer view of its surface morphology and potential changes due to the evaporation process.

(D) EDS images of the 3DVG after the 65-h seawater evaporation, which assists in analyzing the long-term stability of the potential salt fouling and the structure strength.

(E) The experimental setups used for outdoor solar water production tests. The positions of thermocouples are marked with red dots, serving to monitor temperature variations at specific points during the experiments.

(F) Recorded data for solar intensity and daily accumulated solar energy, differentiating between typical sunny and cloudy days to understand how weather conditions impact solar water production.

(G) Temperature variations observed in the water production devices using the 3DVG and the PVG on both sunny and cloudy days.

(H) A comprehensive view of the recorded ambient temperature, solar intensity, and incident solar radiation energy across 5 consecutive experimental days.

(I) The daily water production yield for each of the experimental days.

radiations of 12.65 and 3.01 MJ m^{-2} for the sunny and cloudy days, respectively. Figure 5G shows the temperature variations of the components during the sunny and cloudy days. Clearly, the temperature of all parts of the device is higher on sunny days compared with on cloudy days due to strong photothermal conversion. In terms of the temperatures, the 3DVG exhibits a lower evaporation temperature compared with the PVG, indicating faster double-sided enhanced evaporation in the 3DVG. Furthermore, the condensation surface temperature of the 3DVG is 3°C–7.5°C higher than that of the PVG. As the condensation process releases vapor-liquid condensation latent heat on the surface, the higher condensation temperature indicates higher condensation rates for the 3DVG device, which is expected to result in higher water production.

Please cite this article in press as:et al., Improving solar water harvesting via airflow restructuring using 3D vapor generator, Device (2023), https://doi.org/10.1016/j.device.2023.100065

The temperature of each part of the 3DVG also shows distinct differences (Figure 5G), which can be categorized into three stages based on their variation characteristics. (1) From 9 to 10 a.m., when the solar altitude angle θ is large, only the southeastern side of the 3DVG receives solar radiation, resulting in a higher temperature on the southeastern side ($T_{SE} > T_{NW}$). (2) From 10 to 11 a.m., evaporation exhibits a uniform temperature distribution. (3) After 11 a.m., as the solar altitude angle θ increases, the other northwestern part of the 3DVG shows a higher temperature ($T_{SE} < T_{NW}$). The experimental results align with the simulation results, confirming the excellent solar-energy-harvesting capacity of the 3DVG throughout the day. The 3DVG with a projected area of 80 × 80 cm^2 produces 56.7 g water on the sunny day (Figure S27), equivalent to a water yield of 8.86 kg m^{-2} day^{-1}, approximately 1.8 times higher than the water production of the PVG device.

A 5-day continuous outdoor water production experiment was conducted. The peak solar intensity during experiments ranged from 300 to 1,096 W m^{-2}, and the daily solar radiation energy varied from 3.01 to 17.10 MJ m^{-2} (Figure 5H), resulting in water production yields of 1.088–8.863 kg m^{-2} day^{-1} with a 52%–84% improvement compared with the PVG (Figure 5I). After 5 days of continuous operation, the 3DVG maintained excellent evaporation capacity and environmental adaptability, confirming the feasibility of our material and structural design.

DISCUSSION

In this study, we looked for mechanisms and improvement strategies for enhancing SVGs beyond material choices or structures designs. We examined the heat and mass transfer phenomena around the macroscopic 3D structures of solar vapor evaporators. Additionally, we investigate the energy acquisition under consideration of the sun trajectory in outdoor scenarios, aiming to elucidate the mechanisms behind the performance enhancement of such evaporators in both laboratory and outdoor settings.

Through a combination of experimental and simulation approaches, we attribute the observed enhancement in our 3DVG device to two key factors: (1) the utilization of a double-sided peak-valley 3D structure, which offers larger evaporation surfaces, modified flow patterns, and reduced heat loss, and (2) the effective harnessing of solar energy from multiple inclined surfaces under real-world sunlight conditions.

In laboratory tests, the evaporation rate of our 3DVG reached 1.69 kg m^{-2} day^{-1}, surpassing the plane evaporator and single-sided SVG by 43.2% and 11.1%, respectively. Previous studies have suggested that increased dark evaporation resulting from larger evaporation surfaces contributes to the improved evaporation rate in similar 3D evaporators. However, in our case, the substantial enhancement in overall evaporation rate cannot be solely attributed to increased dark evaporation. Instead, it is primarily due to the accelerated vapor diffusion and minimized heat loss resulting from the double-sided peak-valley structure. Evaporation simulations indicated that the strategic positioning of peaks and valleys in the double-sided 3D structure mitigates vapor aggregation, eliminates stagnation, and alters airflow patterns, leading to stronger upward airflow and lower evaporator temperatures, thereby facilitating more efficient evaporation.

Among most reported solar evaporators where the lab-tested evaporation rate and efficiency are near the thermodynamic limit, their actual water production performances in outdoor settings are either unreported or underwhelming. To help assess the performance gap between lab tests and real-world conditions, we developed a dynamic solar-energy-harvesting model, demonstrating that the 3DVG with multiple inclined surfaces can increase daily solar energy harvesting by up to 31.9% compared with plane evaporators when the sun position throughout the day is considered. Moreover, the 3D structure enables early activation of evaporation at sunrise and prolonged evaporation until nightfall, enabling comprehensive utilization of solar energy. These findings highlight the adaptability of our 3DVG to changes in solar irradiation directions.

Finally, we validated the continuous long-term evaporation performance of the evaporator in both saltwater and seawater and the outdoor water production performance, both of which achieved excellent results. This outcome confirms the effectiveness of the 3D structure and the utilization of commercial materials (Table S2) for the process of evaporation. Given its substantial water production yield in outdoor environments, its cost effectiveness, and its potential for large-scale production, the 3DVG holds immense promise for practical integration into solar evaporation systems. Its implementation offers a sustainable and dependable means of accessing freshwater resources.

EXPERIMENTAL PROCEDURES

Resource availability

Lead contact

Further information and requests for additional details should be directed to and will be fulfilled by the lead contact, Zhenyuan Xu (xuzhy@sjtu.edu.cn).

Materials availability

All unique/stable reagents generated in this study are available from the lead contact without restriction.

Data and code availability

All data needed to evaluate the conclusions in the paper are present in the paper and/or the supplemental information and are available from the lead contact upon reasonable request.

Materials

The silica sol solution (20 wt %) was obtained from Aladdin. The mold was designed using Solidworks software and formed by 3D printing using nylon. The ACFF was purchased from Jiangsu Kejing Carbon, China.

Preparation of the 3DVG and the PVG

Briefly, as shown in Figure 1A, the raw ACFF was dried at 120°C for 8 h to remove the water content and the volatile impurities. Afterward, it was cooled to the ambient temperature and then fixed on the 3D-printed mold. The ACFF together with the 3D-printed mold were immersed in the 20 wt % silica sol solution for 12 h. Then, they were transferred into an oven at 120°C to remove the water and form the 3D origami-type structure. The only difference in PVG preparation was that it did not use a 3D mold for finalization. For comparison, the different 3DVG with heights of 2, 3, and 4 cm were made by selecting different shaping molds. All molds were of the same length (L = 80 mm) and width (B = 80 mm).

Characteristics

The surface morphology of ACFF and 3DVG were characterized by SEM (Nova NanoSEM 230) equipped with EDS (X-MaxN 80, Oxford). The contact angles were measured by a surface contact angle meter (DataPhysics OCA20) at ambient temperature (~22°C) using a 5-μL water droplet as the indicator. The absorption spectrum was measured by a UV-visible-near-IR spectrometer (PerkinElmer LAMBDA 950). The specific surface area and the pore properties

of ACFF and HSCC were analyzed by 3Flex America Micromeritics using the Brunauer–Emmett–Teller (BET) and non-local density functional theory (NLDFT) methods.

Solar evaporation experiments in the lab

The setup for solar evaporation experiments in the lab are shown in Figures 2A and S8. The SVGs were floated on the water surface with the help of polystyrene foam. This foam substrate has two 3-mm channels, enabling the material to extend into the water body for water supply. The two ends of the 3DVG were beneath the water surface to supply water. Additionally, the foam was precisely positioned inside a disposable polystyrene (PS) box that was filled with water, attaining a depth of 10 cm. The polystyrene foam with low thermal conductivity ($\sim$0.03 W m^{-1} s^{-1}) can also help reduce the energy loss of the 3DVG and improve the overall thermal efficiency. The non-evaporation part was shielded with aluminum foil and PE film to prevent its dark evaporation.

The simulated sunlight is provided by a steady-state solar simulator with a 100 × 100 mm rectangular light spot (Sciencetech, UHE-NS-100). The solar intensity was measured and calibrated using a solar radiometer (CEAULIGHT CEL-FZ-A). The continuous mass change curves were recorded by an electronic balance (Sartoris, GL2202L-1SCN, 1 mg) that was connected to a PC for real-time monitoring. All lab experiments were conducted with the controlled ambient temperature of 23°C–27°C and a relative humidity (RH) of 50%–60%. Importantly, to ensure equal energy inputs for 3DVG with different heights, the solar intensity for all experimental cases was measured at the middle height of the 3DVG. The temperature variations of the SVG were recorded by the IR camera (FLIR T630sc).

Outdoor solar evaporation experiments

The outdoor solar evaporation experiment was carried out on the roof of the Sino-Italy GEL at SJTU, China, on July 7, 2022. The experiment lasted around 6 h from 9:55 a.m. to 3:45 p.m. The mass change curves were recorded by two electronic balances (Mettler Toledo ME503) that were connected to a PC. The solar flux was measured by an optical power meter (LP100, New Industries Optoelectronics Tech.). Other ambient data were collected from a portable meteorological station (YGC-BYX-M, YIGU).

Outdoor solar water collection experiments

The devices for outdoor solar water collection experiments were fabricated with acrylic sheets with a hydrophilic coating (NC-3082, Changzhou Nanocoating). The total bottom area of the apparatus measured 14 × 14 cm^2, with a height of 12 cm and an 32° inclined angle of the sloping roof. Within the structure, an acrylic container measuring 8 × 8 cm^2 in surface area and 2 cm in height was internally placed to serve as the water supply layer. Condensed water precipitates were placed along the side walls and top surface before cascading down to the bottom of the apparatus for collection. The continuous 5-day outdoor experiments were carried out on the roof of GEL at SJTU from October 15 to 19, 2022. The solar intensity and the ambient data were collected from a portable meteorological station (YGC-BYX-M, YIGU). The water production experiments started at $\sim$9:00 a.m. and went until 6:00 p.m. each day. The ultra-thin K-type thermocouples with a diameter of 0.1 mm (−20°C to 200°C, ±1°C) were used to measure temperature. The measure points were arranged on the surface of the vapor condensation covers and the SVGs (Figure 5B). All signals of the temperature sensors were collected by a data acquisition device (TP700, TOPRIE).

Long-term saline water and seawater evaporation experiments

Similar to solar evaporation experiments in the lab, the long-term real seawater evaporation experiments were carried out under a solar simulator with an irradiance set at 1 kW m^{-2}. The dynamic fluctuations in evaporation rate were diligently recorded using a precision balance (Sartorius GL22021-1SCN). The saline water was a 3.5 wt % NaCl solution, while the authentic seawater was sourced from the Bohai Sea, specifically from the coastal region of Huludao Island. A straightforward yet effective filtration technique employing filter paper was employed to eliminate solid impurities like sediment and seaweed while retaining vital components such as microorganisms and organic matter. The saline water evaporation experiment persisted for a duration of 13.5 h, with the input energy equivalent to the cumulative solar energy input typically received over a 3-day period. The seawater evaporation trial persisted uninterruptedly for an extended period of 65 h, with a commensurate input energy of 14-day typical daily solar energy. Throughout the experiment, we ensured the timely replenishment of saline water/seawater, thereby maintaining the desired liquid level. The indoor ambient temperature fluctuated between 20°C and 30°C, while the RH spanned from 50% to 90%.

SUPPLEMENTAL INFORMATION

Supplemental information can be found online at https://doi.org/10.1016/j.device.2023.100065.

ACKNOWLEDGMENTS

We gratefully acknowledge funding support from the National Natural Science Foundation of China (no. 51976123, and no. 52376200), the Belt and Road Young Scientists Exchange Program of Shanghai Science and Technology Committee (no. 20160742700), andthe Fundamental Research Funds for the Central Universities (no. 0200316). We also thank Dr. Wenwen Wang and Prof. Tianshu Ge for their discussions on material preparation.

AUTHOR CONTRIBUTIONS

Z.X. and R.W. conceived the idea and led the project. H.S. and Z.Y. conducted all experiments. Z.Y. and J.Y. developed the model and performed the simulation. All authors analyzed the results and contributed to the final manuscript.

DECLARATION OF INTERESTS

The authors declare no competing interests.

INCLUSION AND DIVERSITY

We support inclusive, diverse, and equitable conduct of research.

Received: May 30, 2023
Revised: July 11, 2023
Accepted: August 14, 2023
Published: September 12, 2023

REFERENCES

1. Mekonnen, M.M., and Hoekstra, A.Y. (2016). Four billion people facing severe water scarcity. Sci. Adv. *2*, e1500323. https://doi.org/10.1126/sciadv.1500323.
2. Shannon, M.A., Bohn, P.W., Elimelech, M., Georgiadis, J.G., Mariñas, B.J., and Mayes, A.M. (2008). Science and technology for water purification in the coming decades. Nature *452*, 301–310. https://doi.org/10.1038/nature06599.
3. Griggs, D., Stafford-Smith, M., Gaffney, O., Rockström, J., Öhman, M.C., Shyamsundar, P., Steffen, W., Glaser, G., Kanie, N., and Noble, I. (2013). Sustainable development goals for people and planet. Nature *495*, 305–307. https://doi.org/10.1038/495305a.
4. Elimelech, M., and Phillip, W.A. (2011). The Future of Seawater Desalination: Energy, Technology, and the Environment. Science *333*, 712–717. https://doi.org/10.1126/science.1200488.
5. Zhang, L., Xu, Z., Zhao, L., Bhatia, B., Zhong, Y., Gong, S., and Wang, E.N. (2021). Passive, high-efficiency thermally-localized solar desalination. Energy Environ. Sci. *14*, 1771–1793. https://doi.org/10.1039/D0EE03991H.
6. Wang, Z., Horseman, T., Straub, A.P., Yip, N.Y., Li, D., Elimelech, M., and Lin, S. (2019). Pathways and challenges for efficient solar-thermal desalination. Sci. Adv. *5*, eaax0763. https://doi.org/10.1126/sciadv.aax0763.
7. Xu, N., Li, J., Wang, Y., Fang, C., Li, X., Wang, Y., Zhou, L., Zhu, B., Wu, Z., Zhu, S., and Zhu, J. (2019). A water lily–inspired hierarchical design for

stable and efficient solar evaporation of high-salinity brine. Sci. Adv. *5*, eaaw7013. https://doi.org/10.1126/sciadv.aaw7013.

8. Kim, H., Yang, S., Rao, S.R., Narayanan, S., Kapustin, E.A., Furukawa, H., Umans, A.S., Yaghi, O.M., and Wang, E.N. (2017). Water harvesting from air with metal-organic frameworks powered by natural sunlight. Science *356*, 430–434. https://doi.org/10.1126/science.aam8743.
9. Poredoš, P., Shan, H., Wang, C., Deng, F., and Wang, R. (2022). Sustainable water generation: grand challenges in continuous atmospheric water harvesting. Energy Environ. Sci. *15*, 3223–3235. https://doi.org/10.1039/D2EE01234K.
10. Shan, H., Li, C., Chen, Z., Ying, W., Poredoš, P., Ye, Z., Pan, Q., Wang, J., and Wang, R. (2022). Exceptional water production yield enabled by batch-processed portable water harvester in semi-arid climate. Nat. Commun. *13*, 5406.
11. Yu, Z., Zhu, T., Zhang, J., Ge, M., Fu, S., and Lai, Y. (2022). Fog Harvesting Devices Inspired from Single to Multiple Creatures: Current Progress and Future Perspective. Adv. Funct. Mater. *32*, 2200359. https://doi.org/10.1002/adfm.202200359.
12. Yu, Z., Zhang, J., Li, S., Zhou, Z., Qin, Z., Liu, H., Lai, Y., and Fu, S. (2023). Bio-inspired Copper Kirigami Motifs Leading to a 2D–3D Switchable Structure for Programmable Fog Harvesting and Water Retention. Adv. Funct. Mater. *33*, 2210730. https://doi.org/10.1002/adfm.202210730.
13. Chen, C., Kuang, Y., and Hu, L. (2019). Challenges and Opportunities for Solar Evaporation. Joule *3*, 683–718. https://doi.org/10.1016/j.joule.2018.12.023.
14. Tao, P., Ni, G., Song, C., Shang, W., Wu, J., Zhu, J., Chen, G., and Deng, T. (2018). Solar-driven interfacial evaporation. Nat. Energy *3*, 1031–1041. https://doi.org/10.1038/s41560-018-0260-7.
15. Zhao, F., Guo, Y., Zhou, X., Shi, W., and Yu, G. (2020). Materials for solar-powered water evaporation. Nat. Rev. Mater. *5*, 388–401. https://doi.org/10.1038/s41578-020-0182-4.
16. Gao, M., Zhu, L., Peh, C.K., and Ho, G.W. (2019). Solar absorber material and system designs for photothermal water vaporization towards clean water and energy production. Energy Environ. Sci. *12*, 841–864. https://doi.org/10.1039/C8EE01146J.
17. Ren, H., Tang, M., Guan, B., Wang, K., Yang, J., Wang, F., Wang, M., Shan, J., Chen, Z., Wei, D., et al. (2017). Hierarchical Graphene Foam for Efficient Omnidirectional Solar–Thermal Energy Conversion. Adv. Mater. *29*, 1702590. https://doi.org/10.1002/adma.201702590.
18. Hu, X., Xu, W., Zhou, L., Tan, Y., Wang, Y., Zhu, S., and Zhu, J. (2017). Tailoring Graphene Oxide-Based Aerogels for Efficient Solar Steam Generation under One Sun. Adv. Mater. *29*, 1604031. https://doi.org/10.1002/adma.201604031.
19. Fan, X., Yang, Y., Shi, X., Liu, Y., Li, H., Liang, J., and Chen, Y. (2020). A MXene-Based Hierarchical Design Enabling Highly Efficient and Stable Solar-Water Desalination with Good Salt Resistance. Adv. Funct. Mater. *30*, 2007110. https://doi.org/10.1002/adfm.202007110.
20. Wang, X., Hsieh, M.L., Bur, J.A., Lin, S.Y., and Narayanan, S. (2020). Capillary-driven solar-thermal water desalination using a porous selective absorber. Mater. Today Energy *17*, 100453. https://doi.org/10.1016/j.mtener.2020.100453.
21. Bu, Y., Zhou, Y., Lei, W., Ren, L., Xiao, J., Yang, H., Xu, W., and Li, J. (2022). A bioinspired 3D solar evaporator with balanced water supply and evaporation for highly efficient photothermal steam generation. J. Mater. Chem. A *10*, 2856–2866. https://doi.org/10.1039/D1TA09288J.
22. Wu, X., Wu, Z., Wang, Y., Gao, T., Li, Q., and Xu, H. (2021). All-Cold Evaporation under One Sun with Zero Energy Loss by Using a Heatsink Inspired Solar Evaporator. Adv. Sci. *8*, 2002501. https://doi.org/10.1002/advs.202002501.
23. Zeng, J., Wang, Q., Shi, Y., Liu, P., and Chen, R. (2019). Osmotic Pumping and Salt Rejection by Polyelectrolyte Hydrogel for Continuous Solar Desalination. Adv. Energy Mater. *9*, 1900552. https://doi.org/10.1002/aenm.201900552.
24. Zhao, F., Zhou, X., Shi, Y., Qian, X., Alexander, M., Zhao, X., Mendez, S., Yang, R., Qu, L., and Yu, G. (2018). Highly efficient solar vapour generation via hierarchically nanostructured gels. Nat. Nanotechnol. *13*, 489–495. https://doi.org/10.1038/s41565-018-0097-z.
25. Zhou, X., Zhao, F., Guo, Y., Rosenberger, B., and Yu, G. (2019). Architecting highly hydratable polymer networks to tune the water state for solar water purification. Sci. Adv. *5*, eaaw5484. https://doi.org/10.1126/sciadv.aaw5484.
26. Yao, H., Zhang, P., Yang, C., Liao, Q., Hao, X., Huang, Y., Zhang, M., Wang, X., Lin, T., Cheng, H., et al. (2021). Janus-interface engineering boosting solar steam towards high-efficiency water collection. Energy Environ. Sci. *14*, 5330–5338. https://doi.org/10.1039/D1EE01381E.
27. Guo, Y., Zhao, X., Zhao, F., Jiao, Z., Zhou, X., and Yu, G. (2020). Tailoring surface wetting states for ultrafast solar-driven water evaporation. Energy Environ. Sci. *13*, 2087–2095. https://doi.org/10.1039/D0EE00399A.
28. Zhang, H., Shen, X., Kim, E., Wang, M., Lee, J.-H., Chen, H., Zhang, G., and Kim, J.-K. (2022). Integrated Water and Thermal Managements in Bio-inspired Hierarchical MXene Aerogels for Highly Efficient Solar-Powered Water Evaporation. Adv. Funct. Mater. *32*, 2111794. https://doi.org/10.1002/adfm.202111794.
29. Zhang, P., Liao, Q., Yao, H., Cheng, H., Huang, Y., Yang, C., Jiang, L., and Qu, L. (2018). Three-dimensional water evaporation on a macroporous vertically aligned graphene pillar array under one sun. J. Mater. Chem. A *6*, 15303–15309. https://doi.org/10.1039/C8TA05412F.
30. Wang, Y., Wang, C., Song, X., Huang, M., Megarajan, S.K., Shaukat, S.F., and Jiang, H. (2018). Improved light-harvesting and thermal management for efficient solar-driven water evaporation using 3D photothermal cones. J. Mater. Chem. A *6*, 9874–9881. https://doi.org/10.1039/C8TA01469H.
31. Li, J., Wang, X., Lin, Z., Xu, N., Li, X., Liang, J., Zhao, W., Lin, R., Zhu, B., Liu, G., et al. (2020). Over 10 kg m^{-2} h^{-1} Evaporation Rate Enabled by a 3D Interconnected Porous Carbon Foam. Joule *4*, 928–937. https://doi.org/10.1016/j.joule.2020.02.014.
32. Guo, Y., Zhao, F., Zhou, X., Chen, Z., and Yu, G. (2019). Tailoring Nanoscale Surface Topography of Hydrogel for Efficient Solar Vapor Generation. Nano Lett. *19*, 2530–2536. https://doi.org/10.1021/acs.nanolett.9b00252.
33. Liu, H., Luo, H., Huang, J., Chen, Z., Yu, Z., and Lai, Y. Programmable Water/Light Dual-Responsive Hollow Hydrogel Fiber Actuator for Efficient Desalination with Anti-Salt Accumulation. Advanced Functional Materials n/a, 2302038. https://doi.org/10.1002/adfm.202302038.
34. Wang, W., Shi, Y., Zhang, C., Hong, S., Shi, L., Chang, J., Li, R., Jin, Y., Ong, C., Zhuo, S., and Wang, P. (2019). Simultaneous production of fresh water and electricity via multistage solar photovoltaic membrane distillation. Nat. Commun. *10*, 3012. https://doi.org/10.1038/s41467-019-10817-6.
35. Chiavazzo, E., Morciano, M., Viglino, F., Fasano, M., and Asinari, P. (2018). Passive solar high-yield seawater desalination by modular and low-cost distillation. Nat. Sustain. *1*, 763–772. https://doi.org/10.1038/s41893-018-0186-x.
36. Xu, Z., Zhang, L., Zhao, L., Li, B., Bhatia, B., Wang, C., Wilke, K.L., Song, Y., Labban, O., Lienhard, J.H., et al. (2020). Ultrahigh-efficiency desalination via a thermally-localized multistage solar still. Energy Environ. Sci. *13*, 830–839. https://doi.org/10.1039/C9EE04122B.
37. Morciano, M., Fasano, M., Boriskina, S.V., Chiavazzo, E., and Asinari, P. (2020). Solar passive distiller with high productivity and Marangoni effect-driven salt rejection. Energy Environ. Sci. *13*, 3646–3655. https://doi.org/10.1039/D0EE01440K.
38. Xia, Y., Hou, Q., Jubaer, H., Li, Y., Kang, Y., Yuan, S., Liu, H., Woo, M.W., Zhang, L., Gao, L., et al. (2019). Spatially isolating salt crystallisation from water evaporation for continuous solar steam generation and salt harvesting. Energy Environ. Sci. *12*, 1840–1847. https://doi.org/10.1039/C9EE00692C.
39. Kuang, Y., Chen, C., He, S., Hitz, E.M., Wang, Y., Gan, W., Mi, R., and Hu, L. (2019). A High-Performance Self-Regenerating Solar Evaporator for

Continuous Water Desalination. Adv. Mater. *31*, 1900498. https://doi.org/10.1002/adma.201900498.

40. Zhang, Y., Zhang, H., Xiong, T., Qu, H., Koh, J.J., Nandakumar, D.K., Wang, J., and Tan, S.C. (2020). Manipulating unidirectional fluid transportation to drive sustainable solar water extraction and brine-drenching induced energy generation. Energy Environ. Sci. *13*, 4891–4902. https://doi.org/10.1039/D0EE01572E.

41. He, S., Chen, C., Kuang, Y., Mi, R., Liu, Y., Pei, Y., Kong, W., Gan, W., Xie, H., Hitz, E., et al. (2019). Nature-inspired salt resistant bimodal porous solar evaporator for efficient and stable water desalination. Energy Environ. Sci. *12*, 1558–1567. https://doi.org/10.1039/C9EE00945K.

42. Cooper, T.A., Zandavi, S.H., Ni, G.W., Tsurimaki, Y., Huang, Y., Boriskina, S.V., and Chen, G. (2018). Contactless steam generation and superheating under one sun illumination. Nat. Commun. *9*, 5086. https://doi.org/10.1038/s41467-018-07494-2.

43. Menon, A.K., Haechler, I., Kaur, S., Lubner, S., and Prasher, R.S. (2020). Enhanced solar evaporation using a photo-thermal umbrella for wastewater management. Nat. Sustain. *3*, 144–151. https://doi.org/10.1038/s41893-019-0445-5.

44. Zhang, L., Li, X., Zhong, Y., Leroy, A., Xu, Z., Zhao, L., and Wang, E.N. (2022). Highly efficient and salt rejecting solar evaporation via a wick-free confined water layer. Nat. Commun. *13*, 849. https://doi.org/10.1038/s41467-022-28457-8.

45. Xu, Z., Ran, X., Wang, D., Zhong, M., and Zhang, Z. (2022). High efficient 3D solar interfacial evaporator: Achieved by the synergy of simple material and structure. Desalination *525*, 115495. https://doi.org/10.1016/j.desal.2021.115495.

46. Li, X., Li, J., Lu, J., Xu, N., Chen, C., Min, X., Zhu, B., Li, H., Zhou, L., Zhu, S., et al. (2018). Enhancement of Interfacial Solar Vapor Generation by Environmental Energy. Joule *2*, 1331–1338. https://doi.org/10.1016/j.joule.2018.04.004.

47. Xu, N., Li, J., Finnerty, C., Song, Y., Zhou, L., Zhu, B., Wang, P., Mi, B., and Zhu, J. (2023). Going beyond efficiency for solar evaporation. Nat. Water *1*, 494–501. https://doi.org/10.1038/s44221-023-00086-5.

48. Li, X., Lin, R., Ni, G., Xu, N., Hu, X., Zhu, B., Lv, G., Li, J., Zhu, S., and Zhu, J. (2017). Three-dimensional artificial transpiration for efficient solar wastewater treatment. Natl. Sci. Rev. *5*, 70–77. https://doi.org/10.1093/nsr/nwx051.

49. Du, C., Zhao, X., Qian, X., Huang, C., and Yang, R. (2023). Heat-localized solar evaporation: Transport processes and applications. Nano Energy *107*, 108086. https://doi.org/10.1016/j.nanoen.2022.108086.

50. Arunkumar, T., Raj, K., Kabeel, A.E., and Lee, S.J. (2021). Effects of solar geometry and operation period on stability of solar desalination systems: a review. Environ. Sci. Pollut. Res. Int. *28*, 65014–65032. https://doi.org/10.1007/s11356-021-16566-8.

51. Xu, Y., Ma, J., Liu, D., Xu, H., Cui, F., and Wang, W. (2019). Origami system for efficient solar driven distillation in emergency water supply. Chem. Eng. J. *356*, 869–876. https://doi.org/10.1016/j.cej.2018.09.070.

52. Kelly, N.A., and Gibson, T.L. (2009). Improved photovoltaic energy output for cloudy conditions with a solar tracking system. Sol. Energy *83*, 2092–2102. https://doi.org/10.1016/j.solener.2009.08.009.

53. Guo, L., Tao, X., Gong, Z., Guo, A., Du, H., and Liu, J. (2019). Preparation of MoSi2-SiC-Al2O3-SiO2 coating on mullite fibrous insulation with silica sol as binder by non-firing process. Ceram. Int. *45*, 2602–2611. https://doi.org/10.1016/j.ceramint.2018.10.197.

54. Shan, H., Pan, Q., Xiang, C., Poredoš, P., Ma, Q., Ye, Z., Hou, G., and Wang, R. (2021). High-yield solar-driven atmospheric water harvesting with ultra-high salt content composites encapsulated in porous membrane. Cell Reports Physical Science *2*, 100664. https://doi.org/10.1016/j.xcrp.2021.100664.

55. Shimada, T., Aoki, K., Shinoda, Y., Nakamura, T., Tokunaga, N., Inagaki, S., and Hayashi, T. (2003). Functionalization on Silica Gel with Allylsilanes. A New Method of Covalent Attachment of Organic Functional Groups on Silica Gel. J. Am. Chem. Soc. *125*, 4688–4689. https://doi.org/10.1021/ja034691l.

56. Sun, S., Wang, Y., Sun, B., Zhang, F., Xu, Q., Mi, H.-Y., Li, H., Tao, X., Guo, Z., Liu, C., and Shen, C. (2021). Versatile Janus Composite Nonwoven Solar Absorbers with Salt Resistance for Efficient Wastewater Purification and Desalination. ACS Appl. Mater. Interfaces *13*, 24945–24956. https://doi.org/10.1021/acsami.1c05618.

57. Storer, D.P., Phelps, J.L., Wu, X., Owens, G., Khan, N.I., and Xu, H. (2020). Graphene and Rice-Straw-Fiber-Based 3D Photothermal Aerogels for Highly Efficient Solar Evaporation. ACS Appl. Mater. Interfaces *12*, 15279–15287. https://doi.org/10.1021/acsami.0c01707.

58. Shao, B., Wu, X., Wang, Y., Gao, T., Liu, Z.-Q., Owens, G., and Xu, H. (2020). A general method for selectively coating photothermal materials on 3D porous substrate surfaces towards cost-effective and highly efficient solar steam generation. J. Mater. Chem. A *8*, 24703–24709. https://doi.org/10.1039/D0TA08539A.

59. Kalogirou, S.A. (2022). 3.01 - Solar Thermal Systems: Components and Applications—Introduction. In Comprehensive Renewable Energy, Second Edition, T.M. Letcher, ed. (Elsevier), pp. 1–25. https://doi.org/10.1016/B978-0-12-819727-1.00001-7.